UNIVERSITÀ
DEGLI STUDI
DI PADOVA

Sede amministrativa: Università degli studi di Padova

Dipartimento di Ingegneria dell'Informazione

SCUOLA DI DOTTORATO DI RICERCA IN: Ingegneria dell'Informazione

INDIRIZZO: Bioingegneria

CICLO XXIV

DEVELOPMENT OF NOVEL COMPUTATIONAL ALGORITHMS FOR QUANTITATIVE VOXEL-WISE FUNCTIONAL BRAIN IMAGING WITH POSITRON EMISSION TOMOGRAPHY

Direttore della scuola: Ch.mo Prof. Matteo Bertocco

Supervisore: Prof. Alessandra Bertoldo

Dottorando: Gaia Rizzo

Contents

Summary

Positron Emission Tomography (PET) allows to study, *in vivo*, important biological processes in both animals and humans. In particular, it is widely used for receptor studies, where it allows quantitative functional imaging of physiological parameters in terms of receptor binding, volume of distribution, and/or receptor occupancy.

The radioactivity concentration measured with PET can be related to the underlying physiological processes using appropriate tracer kinetic modeling techniques, generally compartmental models. Once the best compartmental structure describing the behavior of the tracer has been defined, it is possible to estimate the system's micro or macro parameters. This can be achieved at the Region of Interest (ROI) level, i.e. generating a tissue Time Activity Curve (TAC) of the average activity concentration within a specific brain area, or at the voxel level, i.e. deriving the tissue TAC from one single image unit.

The ROI level approach is commonly used to quantify PET images by using nonlinear estimators since ROI TACs are characterized by a good signal-to-noise ratio. However, the use of ROI TACs causes a loss of spatial resolution since it does not allow the quantification of the physiological information with the same spatial detail as the acquired PET data.

Voxel level analysis allows avoiding operator-dependency of manually delineated ROIs and produces parametric maps having the same spatial resolution as the

original PET image. However, TACs derived from a voxel are characterized by a low signal-to-noise ratio. This renders the use of nonlinear estimators difficult and unwieldy because of their computational cost. Thus, more robust and faster estimation algorithms are necessary in order to quantify the physiological information at the voxel level within reasonable computational time.

The purpose of this work is to propose and develop methods to quantify PET tracer activity at voxel level, overcoming the limitations of the approaches already present in literature.

In Chapter 1 an overview on the basis of kinetic modeling in PET and a report of the state of the art literature of the topic will be given. Diverse approaches are available for quantification at the voxel level, such as generalized linear least square ([1]), basis function methods (BFMs) ([2], [3], [4]), spectral analysis ([5]), population methods as Global Two Stage (GTS, [6]), Bayesian estimation ([7]), and graphical approaches such as the Patlak and Logan plots ([8], [9], [10]). Each of them will be presented with their advantages and drawbacks.

In Chapter 2 an overview of the main PET receptor compartmental models is presented, both models with plasma input function and models with reference input function, which are of particular interest as they allow obviating the need for invasive arterial plasma measurements during the PET exam.

In Chapter 3 the proposed novel approaches for Bayesian quantification will be presented. In Section 3.1 the principles of Bayesian estimation are given. In Section 3.2 a general approach to generate parametric maps that consists in a multi-stage hierarchical method will be investigated. Kinetic information are transmitted from the regions to the voxels using a maximum a posteriori (MAP) estimator. A Bayesian estimator considers as known the *a priori* probability of

the model parameters and updates the prior probability itself using the measured data ([11]). When the prior distribution is derived from the data, the method is referred as empirical Bayes.
In Section 3.3 a new hierarchical method to apply BFM to multicompartmental models is investigated. The grids for the basis functions are generated automatically from the data, specifically for each ROI, being consequently user-indipendent. The local grids for the voxel-by-voxel analysis are defined *a priori*, using the estimates obtained by application of the optimal model for the ROI TACs and solving with a non linear estimator, the gold standard method.

In Chapter 4 the datasets available are presented. Six different datasets were made available by Division of Experimental Medicine, Imperial College of London (UK) and by the Institute San Raffaele of Milan (Italy). In particular, datasets of [^{11}C]DPN (selective antagonist at opioid receptors), [^{11}C]FLB457 (high affinity dopamine D_2/D_3 receptor radioligand), [*carbonyl*-^{11}]WAY100635 (selective serotonin 5-HT_{1A} receptor antagonist), [^{11}C]MDL100907 (high affinity serotonin 5-HT_{2A} ligand) and [^{11}C]SCH442416 (highly selective adenosine A_{2A} antagonist) were available. An alternative method for the ROI segmentation by using cluster analysis is also presented in Section 4.2, in order to assess the effect on the results of the different ways to extract the priors.

In Chapter 5 the application of the methods presented above on the various datasets will be illustrated and in Chapter 6 the results obtained with the different methods will be reported and discussed.

In Chapter 7 some additional aims of this work are presented, in particular the development of compartmental model for quantification of PET tracer kinetics. Both novel methods are model-driven methods, based on compartmental models. Consequently, the primary aim of the work has been the identification of the

optimal model to describe the data, in case it was not already presented in literature. A new compartmental model for [^{11}C]SCH442416 and for [^{11}C]MDL100907 dataset was developed. [^{11}C]SCH442416 data have never been quantified with compartmental models in humans before and for [^{11}C]MDL100907 the model presented in literature was not appropriate for the fit of the available data.

In Chapter 8 an overall discussion and conclusions are presented. In particular, in Section 8.2 a comparison with existing methodologies is implemented, focusing on population methods, as Global and Iterative Two Stage.

The main results of this work are the development of two methods for voxel-wise quantification of PET data, H-MAP and H-BFM. The methods are a good alternative for the generation of reliable parametric maps, and applied to clinical data are expected to simplify r the detection also of small/specific pathological areas. The first method led to a publication in Neuroimage ([12]), the second was presented during two international conferences (BrainPET2011 and SNM2011) as oral contribution and a publication is ready to be submitted.
The novel methods proposed have been already inserted in PIWAVE, a pre-existing software for voxel-wise PET quantification originally developed by Imperial College of London.

As additional results, an alternative method for the ROI segmentation by using cluster analysis was implemented and a new compartmental model for [^{11}C]SCH-442416 and [^{11}C]MDL100907 data was developed. A new method for the selection of the optimal reference region was implemented and applied on [^{11}C]MDL100907 data.

Sommario

La Tomografia ad Emissione di Positroni (PET) permette di studiare, *in vivo*, l'interazione dei traccianti con specifici siti di legame (trasportatori, recettori, etc.). Inoltre permette un imaging funzionale quantitativo di importanti parametri fisiologici quali la densità di recettori, volume di distribuzione e/o occupazione recettoriale.

La concentrazione di radioattività misurata con la PET può essere messa in relazione con i processi fisiologici usando appropriate strategie modellistiche, in genere modelli compartimentali. Una volta definita la struttura compartimentale che meglio descrive le cinetiche del tracciante, è possibile stimare i micro o macro parametri del sistema. Tale analisi può essere eseguita a livello di regione di interesse (ROI - Region of Interest), cioè generando una curva (TAC - Time Activity Curve) della concentrazione di radioattività media in una specifica area cerebrale, o a livello di voxel, cioè derivando la curva tessutale da un singolo elemento dell'immagine.

L'approccio a livello di regione è usato solitamente per quantificare immagini PET con stimatori non lineari dato che le curve tessutali di regione sono caratterizzate da un buon rapporto segnale disturbo. Tuttavia, l'analisi a livello di regione comporta una perdita in risoluzione spaziale, dato che non permette di quantificare l'informazione fisiologica con lo stesso dettaglio spaziale delle immagini acquisite.

L'analisi a livello di voxel permette di evitare la selezione a mano (dipendente dall'operatore) delle regioni e produce mappe parametriche con la stessa risoluzione spaziale dell'immagine PET originale. Tuttavia, le TAC derivate da un voxel sono caratterizzate da un basso rapporto segnale disturbo e ciò rende l'uso di stimatori non lineari difficile e inefficiente, dato il loro costo computazionale. Sono quindi necessari algoritmi di stima più robusti e veloci per quantificare l'informazione fisiologica a livello di voxel in un tempo ragionevole.

Obiettivo di questo lavoro è proporre e sviluppare metodi per la quantificazione di immagini PET a livello di voxel, superando le limitazioni dei metodi già presenti in letteratura.
Nel Capitolo 1 è presentata una panoramica dei principali metodi modellistici in PET e una rassegna sullo stato dell'arte. Vari approcci sono già disponibili per la quantificazione a livello di voxel, come il generalized linear least square ([1]), basis function methods (BFMs) ([2], [3], [4]), spectral analysis ([5]), metodi di popolazione come Global Two Stage (GTS, [6]), stima Bayesiana ([7]), e metodi grafici quali il Patlak e Logan plots ([9], [10]). Per ognuno di questi verranno descritti vantaggi e limiti.

Il Capitolo 2 espone una panoramica dei principali modelli compartimentali recettoriali, sia modelli con ingresso la curva dell'attività plasmatica del tracciante, che modelli a regione di riferimento, di particolare interesse poiché permettono di evitare l'invasivo campionamento arteriale durante l'esame PET.

Il Capitolo 3 propone i nuovi approcci Bayesiani sviluppati per la quantificazione PET. Nella Sezione 3.1 sono presentati i principi di stima Bayesiana. Nella Sezione 3.2 viene descritto un approccio generale per la generazione di mappe parametriche, basato su un metodo gerarchico multi-livello. Le informazioni cinetiche ottenute per la regione vengono trasmesse ai voxel appartenenti a cias-

cuna classe con uno stimatore Maximum A Posteriori (MAP). Uno stimatore Bayesiano considera nota la probabilità *a priori* dei parametri del modello e la aggiorna basandosi sui dati misurati ([11]). Quando l'informazione *a priori* è derivata dai dati, il metodo è detto Bayesiano empirico.
La Sezione 3.3 descrive un nuovo metodo gerarchico per applicare il metodo BFM a modelli multi compartimentali. Le griglie per le funzioni base sono generate automaticamente dai dati, specifiche per ogni regione, e di conseguenza in modo indipendente dall'utente. Le griglie locali per l'analisi a livello di voxel sono definite *a priori*, usando le stime ottenute applicando il modello ottimo alle curve di regione e risolvendolo con uno stimatore non lineare, che rappresenta il metodo gold standard.

Nel Capitolo 4 sono presentati i sei dataset messi a disposizione dalla Division of Experimental Medicine, Imperial College of London (UK) e dall'Istituto San Raffaele di Milano (Italia). I dataset disponibili constano di dati di [^{11}C]DPN (antagonista selettivo ai recettori oppiodi), [^{11}C]FLB457 (radioligando ad alta affinità per i recettori di dopamina D_2/D_3), [*carbonyl*-^{11}]WAY100635 (antagonista selettivo ai recettori di serotonina 5-HT_{1A}), [^{11}C]MDL100907 (ligando ad alta affinità per i recettori di serotonina 5-HT_{2A}) e [^{11}C]SCH442416 (antagonista altamente selettivo ai recettori di adenosina A_{2A}) Viene inoltre presentato un metodo alternativo per la segmentazione delle ROI tramite cluster analysis (Sezione 4.2), per valutare l'effetto dei diversi modi di estrarre i priors sui risultati.

Nel Capitolo 5 si presenta l'applicazione dei metodi descritti in precedenza sui vari dataset e nel Capitolo 6 vengono descritti e discussi i risultati ottenuti.

Il Capitolo 7 espone alcuni obiettivi aggiuntivi di questo lavoro, in particolare lo sviluppo di modelli compartimentali per la quantificazione delle cinetiche di traccianti PET. I nuovi metodi proposti sono *model-driven*, basati cioè su

modelli compartimentali. Di conseguenza l'obiettivo iniziale del lavoro è stato l'identificazione del miglior modello per descrivere i dati, qualora tale modello non fosse già presente in letteratura. Un nuovo modello compartimentale è stato sviluppato per il dataset di dati [^{11}C]SCH442416 e per i dati di [^{11}C]MDL100907. I dati di [^{11}C]SCH442416 non sono mai stati analizzati in precedenza con modelli compartimentali nell'uomo e per i dati da [^{11}C]MDL100907 il modello presentato in letteratura non è stato invece adatto a descrivere i dati a disposizione.

Nel Capitolo 8 si espongono la discussione complessiva e le conclusioni. In particolare, nella Sezione 8.2 si presenta un confronto dei metodi sviluppati con le metodologie esistenti, con speciale attenzione ai metodi di popolazione, come il Global e Iterative Two Stage.

I principali risultati di questo lavoro consistono nello sviluppo di due metodi per la quantificazione di dati PET a livello di voxel, H-MAP e H-BFM. I metodi costituiscono un'alternativa per la generazione di mappe parametriche affidabili ed applicate a dati clinici renderanno più semplice il riconoscimento di piccole zone patologiche specifiche. Il primo metodo ha portato ad una pubblicazione su Neuroimage ([12]), il secondo lavoro è stato presentato durante due conferenze internazionali (BrainPET2011 e SNM2011) come *oral presentation* e una pubblicazione è in fase di sottomissione.
Come ulteriore risultato, è stato implementato un metodo alternativo per la segmentazione di regioni tramite cluster analysis ed è stato sviluppato un nuovo modello compartimentale per i dati di [^{11}C]SCH442416 e di [^{11}C]MDL100907. Inoltre è stato implementato un nuovo metodo per la selezione della migliore regione di riferimento ed è stato applicato su immagini di [^{11}C]MDL100907.

Chapter 1

Introduction

Positron Emission Tomography (PET) is a functional nuclear medicine imaging technique widely used to study *in vivo* physiological processes in the body. After injection of a radiotracer (i.e. a positron-emitting radionuclide) into a patient, a normal volunteer or a research animal, PET instrumentation detects pairs of gamma rays generated after annihilation of any emitted positron with any electron of the surrounding material. Four-dimensional images representing the radioactivity concentration of the injected tracer over time are generated with an appropriate reconstruction algorithm and with proper corrections for the physical effects such as attenuation, dead time and scatter.

The radioactivity concentration measured during a dynamic PET exam can be related to the underlying physiological processes using appropriate tracer kinetic modeling techniques, where the model input is either the time course of the tracer concentration in plasma or, for receptor studies, that of the tracer concentration in an appropriate region, called reference region, devoid of receptors specific for the tracer under examination. The kinetic analysis allows quantitative functional imaging of physiological parameters such as blood flow, rate of glucose consumption or amount of binding of the tracer to its specific receptors, depending upon the tracer in use.

These modeling techniques can be divided into model-driven methods and data-driven methods. The distinction is that data-driven methods do not require any *a priori* definition of the best model structure, but this information is derived directly from the kinetic data. There are three data-driven methods developed for quantitative PET analysis: graphical analysis (Patlak plot, [8], [9], and Logan plot, [10]), spectral analysis ([5]) and basis pursuit ([13]).

Graphical methods are model-independent methods and allow fast estimation of the parameters of interest through a transformation of the data that, after a certain time $t > t^*$, shows a linear trend, whose slope can be related to the parameter of interest. However it is possible to estimate only one macro system parameter.

In spectral analysis ([5]) the kinetic activity of the tracer in the tissue is described by the sum of decaying exponentials convolved with an input function, and the coefficients of a predefined set of biologically plausible exponential basis functions are estimated using nonnegative least squares to fit the data. Spectral analysis also returns information on the number of compartments necessary to describe the data.

Basis pursuit denoising ([13]) is an alternative approach to solve the linear system of equations of spectral analysis, and includes a regularization term. Also this technique returns parameter estimates that describe the transfer function of the system, information on the number of components and on the type of kinetics.

Thus graphical methods allow the estimation of only macroparameters but they are easy and fast to implement. Spectral analysis and basis pursuit allow to characterize the transfer function of the system but the relation of these parameters to measures of the physiological process of interest is possible only with knowledge of the biochemical properties of the tracer and with the definition of the model structure. In general data-driven methods allow generation of reliable parametric maps and require less restrictive hypothesis compared to model-driven methods.

In order to apply model-driven methods it is instead necessary to define the com-

partmental structure that best describe the behavior of the tracer, with specific assumptions on the number of compartments and their connections. It is thus possible to relate the parameters to specific physiological measures. In PET, the kinetic rate constants of the compartmental model are called micro parameters. Well-established compartmental models in PET include those used for the quantification of blood flow ([14]), cerebral metabolic rate for glucose ([15]), and for neuroreceptor ligand binding ([16]).
Further developments have produced models using the reference tissue as model input, thus avoiding the need for blood sampling ([17], [18], [19], [20], [21]). Micro or macro system parameters are obtained using a least squares fitting procedure such as linear least squares ([22]), non linear least squares ([22]), generalized linear least squares ([1]) or basis function techniques ([2]).

Among the various modeling techniques, compartmental modeling represents the gold standard in PET quantification. The analysis can be applied both at the Region of Interest (ROI) level, i.e. generating a tissue Time Activity Curve (TAC) of the average activity concentration within a specific brain area, or at the voxel level, i.e. deriving the tissue TAC from one single image unit. In the ROI level approach PET data are quantified using nonlinear estimators since ROI TACs are characterized by a good signal-to-noise ratio. However, the use of ROI TACs causes a loss of spatial resolution since it does not allow the quantification of the physiological information with the same spatial detail as the acquired PET data. Voxel level analysis allows avoiding operator-dependency of manually delineated ROIs and produces parametric maps having the same spatial resolution as the original PET image. However, TACs derived from a voxel are characterized by a low signal-to-noise ratio. This renders the use of nonlinear estimators difficult and unwieldy because of their computational cost. Thus, more robust and faster estimation algorithms are necessary in order to quantify the physiological information at the voxel level within reasonable computational time.

Diverse approaches are available for quantification at the voxel level based on compartmental modeling, such as generalized linear least square (GLLS) ([1]), basis function methods (BFMs) ([2], [3] and [4]), Global Two Stage (GTS, [6]) and Bayesian estimation ([23], [7]).

In the GLLS approach, the model is linearized and then solved iteratively via linear least square in order to eliminate the bias introduced by the linearization of the model. The method was proven to lead to precise and accurate results in the presence of low noise levels when the model which describes the data is composed of two compartments, but its performance deteriorates rapidly at high noise levels ([24]), typical of TACs derived from a single voxel. Moreover, the choice of the termination criterion is crucial and GLLS's computational cost can be high or at least not negligible.

Among the so-called "population approaches", developed and largely used in pharmacokinetic/pharmacodynamic studies, GTS is an iterative method which has been demonstrated to be utilizable in quantitative PET for the generation of parametric maps and tested on Simplified Reference Tissue Model (SRTM, [20]) and simulated 2-tissue PET data. In this approach, the estimates for each voxel are iteratively updated using both the population variability and the precision of the individual estimates. However, the performance of the method is sensitive to the goodness of the initial values and to the noise level of PET data ([6]).

BFMs is the most used method, in which a grid consisting of exponential terms convolved with the input function is defined *a priori* and the model is then solved with linear estimators. It is commonly used as it can be easily applied to SRTM. The method presents certain limitations, such as user-defined grids, fixed for all subjects and brain voxels. Moreover, the choice of the grid can heavily penalize the results and can lead to bias in the final estimates, which can also be affected by the presence of noise in the data ([25]).

The BFMs have been also applied on multi-compartmental models, but the grids were still fixed and very dense and the quantification was computationally de-

manding ([3]).

Among the Bayesian methods, in the linear and non linear ridge regression with spatial constraints by Zhou et al. ([23], [26]) the parametric images obtained with linear regression are spatially smoothed and then used as spatial constraints for a second iteration of ridge regression. In particular, the *a priori* information is provided for each voxel by the TACs of the voxels in its neighborhood, making the method appropriate only for linear models, as the computational cost would be too high for clinical routine use in case of non linear models.

The Bayesian method proposed by [7] is based on a nonlinear estimator and uses prior information obtained by analyzing a prior cohort of parametric images. This implies both the need of a high computational time and the necessity of having an additional sufficiently large data set to derive reliable *a priori* information.

The purpose of this work was to propose and develop methods to quantify PET tracer activity at voxel level, overcoming the limitations of the methods above, e.g. the use of global and user-defined grids and the necessity of choosing a termination criterion, and to avoid the sensitivity to initial estimates.

At first a general approach to generate parametric maps that consists in a multistage hierarchical method was investigated. Kinetic information obtained analyzing systems which are akin in terms of, for instance, receptor densities or distribution volumes, can be transmitted to the voxels belonging to each class using a maximum a posteriori (MAP) estimator. At voxel level the model was linearized and solved with a MAP estimator to eliminate the bias introduced with the model linearization. A Bayesian estimator considers as known the *a priori* probability of the model parameters and updates the prior probability itself using the measured data ([22]). The method (Hierarchical MAP, H-MAP) is based on a linear estimator, with a negligible computational cost ($< 5\%$ of the time required to complete the analysis with a non linear estimator).

A method to generate parametric maps based on compartmental modeling in its

original non linear definition was then investigated. Focusing on the BFM, the most widely used method generally applied to SRTM, a new hierarchical method to apply BFM to multicompartmental models (Hierarchical BFM, H-BFM) was developed. The grids for the basis functions were generated automatically from the data, specifically for each ROI, being consequently user-independent. The local grids for the voxel-by-voxel analysis were defined *a priori*, using the estimates obtained by application of the optimal model for the ROI TACs solved with a non linear estimator, the gold standard method. The H-BFM was applied both to model with plasma input function and to model with reference input function, which are of particular interest as they allow obviating the need for invasive arterial plasma measurements during the PET exam.

The methods presented above were tested on different datasets, made available by the Division of Experimental Medicine, Imperial College of London (UK) and by the Institute San Raffaele of Milan (Italy). In particular, datasets of [^{11}C]DPN (selective antagonist at opioid receptors), [^{11}C]FLB457 (high affinity dopamine D_2/D_3 receptor radioligand), [*carbonyl*-^{11}]WAY100635 (selective serotonin 5-HT_{1A} receptor antagonist), [^{11}C]MDL100907 (high affinity serotonin 5-HT_{2A} ligand) and [^{11}C]SCH442416 (highly selective adenosine A_{2A} antagonist) were available.
In all the methods described above, the ROIs have been always defined in two alternative ways, in order to evaluate the impact of the cerebral segmentation on the results. In particular, the regions were obtained based on anatomical information, using the Hammersmith BrainAtlas ([27]) or based on functional information, using an unsupervised clustering.

Additional aims of this work were the development of compartmental models for quantification of PET tracer kinetics and the implementation of a new method for the selection of the optimal reference region. The majority of the methods

investigated are model-driven methods, based on compartmental models. Consequently, it was necessary to identify the optimal model to describe the data, in case it was not already presented in literature. In particular, a new compartmental model was developed for the [^{11}C]SCH442416 dataset, never quantified with compartmental models in humans before, and for [^{11}C]MDL100907 , as the model presented in literature was not appropriate for the fit of our data. The methodology for the selection of the optimal reference region was also applied on the same [^{11}C]MDL100907 dataset.

Chapter 2

PET receptor kinetic models

In PET receptor studies, there are mainly three models with plasma input function used to describe the data at voxel level, i.e. one tissue-two rate constants model (1T), two tissue-three rate constants model (3K), two tissue-four rate constants model (2T).

The three tissue-six rate constant model (3T) is difficult to estimate in all its parameters. The model consists in four different compartments, accounting for the concentration of tracer in plasma (C_p), the free concentration in tissue (C_{free}), the non-specifically bound tracer concentration in plasma (C_{ns}) and the receptor-bound (specifically) tracer concentration (C_{sp}).

This model is generally simplified under the assumption of a rapid equilibrium between free and non-specifically bound compartments that produces a single compartment of non displaceable (free + non-specifically bound) ligand (C_{nd}), leading to the 2T model.

One exception which allow the use of the 3T model is [^{11}C]Flumazenil data whose ROI kinetics are best described by the full model ([28]), but as for the author's knowledge, there are no tracers allowing the fit of the 3T model at voxel level.

Among the reference input models, the Simplified Reference Tissue Model (SRTM) is the most widely used for voxel level analysis. The more complex Full Reference

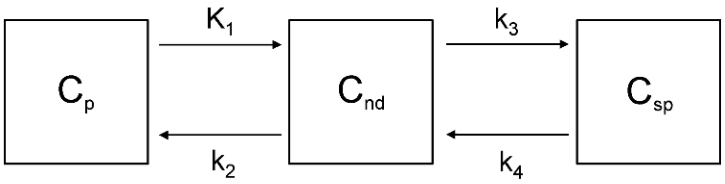

Figure 2.1: Two tissue-four rate constants (2T) compartmental model. K_1 (ml/g/min), k_2 (min^{-1}), k_3 (min^{-1}) and k_4 (min^{-1}) are the rate constants for tracer transport from plasma to tissue and return, and from the non displaceable compartment to the specific one and return, respectively. The tissue is represented by a compartment for the non displaceable component (nd) and a specifically bound fraction (sp).

Tissue Model (FRTM) it is not generally used for voxel-wise quantification due to stability problems.

All these model can be solved not only using nonlinear fitting but also using linearized methods ([29]), or with basis functions ([2]).

2.1 Two tissue-four rate constants plasma input model

The 2T compartmental model presented in Figure 2.1 includes the arterial plasma component (C_p) and two tissue compartments, one describing the non displaceable component (C_{nd}) and one describing the specific binding (C_{sp}), according to:

$$\begin{aligned} \dot{C}_{nd}(t) &= K_1 C_p(t) - (k_2 + k_3)\, C_{nd}(t) + k_4 C_{sp}(t) \qquad & C_{nd}(0) &= 0 \\ \dot{C}_{sp}(t) &= k_3 C_{nd}(t) - k_4 C_{sp}(t) & C_{sp}(0) &= 0 \end{aligned} \tag{2.1}$$

$$C_{VOI}(t) = (1 - V_b)\,(C_{nd}(t) + C_{sp}(t)) + V_b C_b(t) \tag{2.2}$$

where C_b is the concentration of the tracer in the whole blood (kBq/ml), V_b is the fraction of blood volume (unitless) and K_1 (ml/g/min), k_2 (min^{-1}), k_3[1] (min^{-1})

[1]The pooling of C_{free} and C_{ns} causes a change in the meaning of the parameter k_3 from 3T to 2T model, because only the free tracer concentration is available for binding to receptors.

and k_4 (min^{-1}) are the rate constants for tracer transport from plasma to tissue and return, and from the non displaceable compartment to the specific one and return, respectively.

The parameters to be estimated are K_1, k_2, k_3 and k_4, and from these values it is possible to calculate the system macro parameters. In particular, the parameter of interest is the total volume of distribution (V_T, ml/g), defined as the ratio of the tracer concentration in the tissue to the metabolite corrected plasma concentration at equilibrium and provides an estimate of receptor binding ([30]). For the 2T model, it is calculated as:

$$V_T = \frac{K_1}{k_2}\left(1 + \frac{k_3}{k_4}\right) \tag{2.3}$$

Another parameter of interest is the binding potential (BP, unitless) defined as the ratio at equilibrium of specifically bound radioligand to that of non displaceable radioligand in tissue ([31]) and it is defined as:

$$BP_{ND} = \frac{k_3}{k_4} \tag{2.4}$$

2T: linearized

It is common practice in PET quantification to consider the blood component negligible at voxel level, i.e. $V_b = 0$. Thus, this model can be linearized obtaining the following equation, with $C_T(t) = C_{nd}(t) + C_{sp}(t)$:

$$\begin{aligned} C_T(t) = -\vartheta_1 \int_0^t C_T(\tau)d\tau - \vartheta_2 \int_0^t \int_0^t C_T(\tau)d\tau d\tau + \vartheta_3 \int_0^t C_p(\tau)d\tau + \\ + \vartheta_4 \int_0^t \int_0^t C_p(\tau)d\tau d\tau \end{aligned} \tag{2.5}$$

From here on, k_3 indicates $f_{ND}k_3$, where f_{ND} is the free fraction of ligand in the nondisplaceable tissue, which is assumed to be constant over time. It is common practice in PET quantification, moreover f_{ND} is rarely measured.

with:

$$\begin{aligned}\vartheta_1 &= k_2 + k_3 + k_4 \\ \vartheta_2 &= k_2 k_4 \\ \vartheta_3 &= K_1 \\ \vartheta_4 &= K_1 (k_3 + k_4)\end{aligned} \tag{2.6}$$

The parameters ϑ_1, ϑ_2, ϑ_3 and ϑ_4 can be estimated with a linear least square estimator.

2T: basis function

Solving the 2T model, the tissue concentration of Eq. 2.2 can be written in form of basis functions, with α_1, α_2 and V_b as parameter to be estimated, as:

$$C_{VOI}(t) = \alpha_1 C_p(t) \otimes e^{-\beta_1 t} + \alpha_2 C_p(t) \otimes e^{-\beta_2 t} + V_b C_b(t) \tag{2.7}$$

where $\otimes$ denotes the convolution operator and where:

$$\begin{aligned}\alpha_1 &= (1 - V_b)\, \tfrac{K_1(\beta_1 - k_3 - k_4)}{\beta_1 - \beta_2} \\ \alpha_2 &= (1 - V_b)\, \tfrac{K_1(k_3 + k_4 - \beta_2)}{\beta_1 - \beta_2} \\ \beta_1, \beta_2 &= \tfrac{(k_2 + k_3 + k_4) \mp \sqrt{(k_2 + k_3 + k_4)^2 - 4 k_2 k_4}}{2}\end{aligned} \tag{2.8}$$

In this form the model parameters can be estimated with a linear estimator, assuming β_1 and β_2 as known, as in [2].

2.2 Two tissue-three rate constants plasma input model

The two tissue-three rate constants compartmental (3K) model was originally presented in [15], and it is used to describe kinetics of tracers which bind irreversibly to the tissue during the PET exam (i.e. $k_4 = 0$). This model (presented in Figure 2.2) includes the arterial plasma component (C_p) and two tissue compartments, one describing the non displaceable component (C_{nd}) and one describing

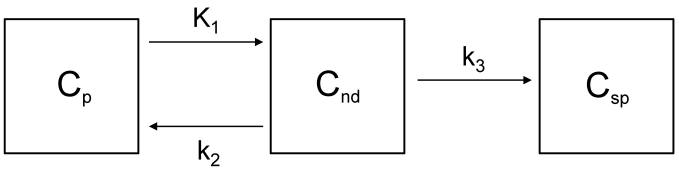

Figure 2.2: Two tissue-three rate constants (3K) compartmental model. K_1 (ml/g/min) and k_2 (min^{-1}) represent first order rate constants for transport of ligand from plasma to tissue and vice versa. k_3 (min^{-1}) is the rate constant from the non displaceable compartment to the specific one. The tissue is represented by a compartment for the non displaceable component (nd) and a specifically bound fraction (sp).

the specific binding (C_{sp}), according to:

$$\begin{aligned} \dot{C}_{nd}(t) &= K_1 C_p(t) - (k_2 + k_3)\, C_{nd}(t) \qquad & C_{nd}(0) &= 0 \\ \dot{C}_{sp}(t) &= k_3 C_{nd}(t) & C_{sp}(0) &= 0 \end{aligned} \tag{2.9}$$

$$C_{VOI}(t) = (1 - V_b)\,(C_{nd}(t) + C_{sp}(t)) + V_b C_b(t) \tag{2.10}$$

where C_b is the concentration of tracer in whole blood (kBq/ml), V_b is the fraction of blood volume (unitless), K_1 (ml/g/min) and k_2 (min^{-1}) are the rate constants for transport of tracer from plasma to tissue and return, respectively, and k_3 (min^{-1}) is the rate constant from the non displaceable compartment to the specific one.

The parameters to be estimated are K_1, k_2 and k_3, and from these values it is possible to calculate the macro parameters of interest. In particular, for 3K model the parameter of interest is the irreversible uptake rate constant (K_I, ml/g/min) and it is calculated as:

$$K_I = \frac{K_1 k_3}{k_2 + k_3} \tag{2.11}$$

It is also possible to consider the pseudo-volume of distribution as:

$$V_T = \frac{K_1}{k_2 + k_3} \tag{2.12}$$

3K: linearized

Considering negligible the blood component at voxel level, the model can be linearized obtaining the following equation, with $C_T(t) = C_{nd}(t) + C_{sp}(t)$:

$$C_T(t) = -\vartheta_1 \int_0^t C_T(\tau)d\tau + \vartheta_2 \int_0^t C_p(\tau)d\tau + \vartheta_3 \int_0^t \int_0^t C_p(\tau)d\tau d\tau \tag{2.13}$$

with:

$$\begin{aligned} \vartheta_1 &= k_2 + k_3 \\ \vartheta_2 &= K_1 \\ \vartheta_3 &= K_1 k_3 \end{aligned} \tag{2.14}$$

The parameters ϑ_1, ϑ_2 and ϑ_3 can be estimated with a linear least square estimator.

3K: basis function

This model can be solved with basis functions obtaining the following equation:

$$C_{VOI}(t) = \alpha_0 \int_0^t C_p(\tau)d\tau + \alpha_1 C_p(t) \otimes e^{-\beta_1 t} + V_b C_b(t) \tag{2.15}$$

with:

$$\begin{aligned} \alpha_0 &= (1 - V_b)\, \tfrac{K_1 k_3}{k_2 + k_3} \\ \alpha_1 &= (1 - V_b)\, \tfrac{K_1 k_2}{k_2 + k_3} \\ \beta_1 &= k_2 + k_3 \end{aligned} \tag{2.16}$$

In this form the model parameters α_0, α_1 and V_b can be estimated with a linear estimator, assuming β_1 as known, as in [2].

2.3 One tissue-two rate constants plasma input model

The 1-tissue compartmental (1T) model is the simplest model used to quantify PET data of reversible tracer. This model (presented in Figure 2.3) includes the arterial plasma compartment C_p and a tissue compartment C_T that incorporates

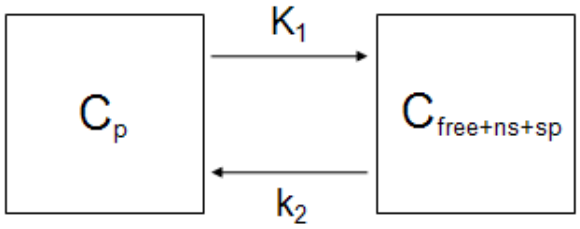

Figure 2.3: One tissue-two rate constants (1T) compartmental model. K_1 and k_2 represent first order rate constants for transport of ligand from plasma to tissue and vice versa. The tissue is represented by a compartment for a free fraction (free) plus a nonspecifically bound (ns) plus a specifically bound fraction (sp).

the free fraction (*free*) plus a non specifically bound fraction (*ns*) and a specific bound fraction (*sp*), according to:

$$\dot{C}_T(t) = K_1 C_p(t) - k_2 C_T(t) \qquad C_T(0) = 0 \tag{2.17}$$

$$C_{VOI}(t) = (1 - V_b)\, C_T(t) + V_b C_b(t) \tag{2.18}$$

where C_b is the concentration of tracer in whole blood (kBq/ml), V_b is the fraction of blood volume (unitless), K_1 (ml/g/min) and k_2 (min^{-1}) are the rate constants for transport of tracer from plasma to tissue and back, respectively.
The parameters to be estimated are K_1 and k_2 and from these values the total volume of distribution (V_T, ml/g) can be calculated as:

$$V_T = \frac{K_1}{k_2} \tag{2.19}$$

1T: linearized

This model can be linearized obtaining the following equation:

$$C_T(t) = K_1 \int_0^t C_p(\tau) d\tau - k_2 \int_0^t C_T(\tau) d\tau \tag{2.20}$$

The blood component is considered negligible at voxel level, and the parameters K_1 and k_2 can be estimated with linear least square estimator.

1T: basis function

This model can be solved with basis functions obtaining the following equation:

$$C_{VOI}(t) = \alpha_1 C_p(t) \otimes e^{-\beta_1 t} + V_b C_b(t) \tag{2.21}$$

with:

$$\begin{aligned} \alpha_1 &= (1 - V_b)\, K_1 \\ \beta_1 &= k_2 \end{aligned} \tag{2.22}$$

In this form the model parameters α_1 and V_b can be estimated with a linear estimator, assuming β_1 as known, as in [2].

2.4 Reference Tissue Models

2.4.1 Full Reference Tissue Model

In the Full Reference Tissue Model (FRTM), originally developed in ([20]), the input function is the TAC of a reference region with non-existent (or very low) specific binding for the tracer under analysis.

The model was originally implemented at ROI level and it is not generally used for voxel-wise quantification due to stability problems, even though the model is globally identifiable.

It is common instead to use the SRTM ([21]), which can be easily implemented at voxel level using BFM, but it implies a model simplification which leads to loss of information when the tracer under analysis does not match the assumptions, i.e. very frequently.

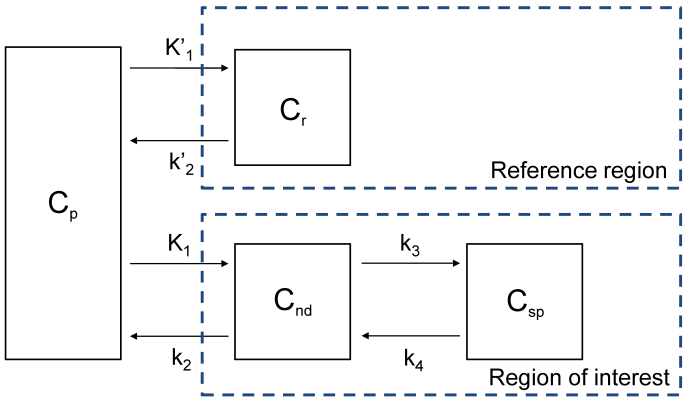

Figure 2.4: Full Reference Tissue Model (FRTM): K_1 (ml/g/min), k_2 (min^{-1}), k_3 (min^{-1}) and k_4 (min^{-1}) are the rate constants for tracer transport from plasma to tissue and return, and from the non displaceable compartment to the specific one and return, respectively. K_1' (ml/g/min) and k_2' (min^{-1}) are the rate constant for transfer from plasma to reference compartment and return, respectively. The tissue is represented by a compartment for the non displaceable component (nd) and a specifically bound fraction (sp).

The FRTM presented in Figure 2.4 includes the arterial plasma component (C_p), two tissue compartments, one describing the non displaceable component (C_{nd}) and one describing the specific binding (C_{sp}), and one reference component (C_r). The blood component is considered negligible. The model is based on the following differential equations:

$$\begin{aligned} \dot{C}_r(t) &= K_1' C_p(t) - k_2' C_r(t) & C_r(0) &= 0 \\ \dot{C}_{nd}(t) &= K_1 C_p(t) - (k_2 + k_3)\, C_{nd}(t) + k_4 C_{sp}(t) & C_{nd}(0) &= 0 \\ \dot{C}_{sp}(t) &= k_3 C_{nd}(t) - k_4 C_{sp}(t) & C_{sp}(0) &= 0 \end{aligned} \tag{2.23}$$

$$C_{VOI}(t) = C_{nd}(t) + C_{sp}(t) \tag{2.24}$$

where K_1 (ml/g/min), k_2 (min^{-1}), k_3 (min^{-1}) and k_4 (min^{-1}) are the rate constants for transfer from plasma to tissue and return, and from the non displaceable compartment to the specific one and return, respectively. K_1' (ml/g/min) is the rate constant for transfer from plasma to reference compartment and k_2' (min^{-1}) is the rate constant for transfer from reference to plasma compartment.

The parameter of interest is the binding potential (BP, unitless) defined as the ratio at equilibrium of specifically bound radioligand to that of non displaceable radioligand in tissue ([31]) and it is defined as:

$$BP = \frac{k_3}{k_4} \tag{2.25}$$

The model described by Eq. 2.23 is not univocally identifiable as the rate constants K_1 and K_1' only enter as a ratio ($R_1 = \frac{K_1}{K_1'}$), accounting for differences in delivery between the region of interest and the reference tissue. Assuming that the volume of distribution of the not specifically bound tracer in both tissues is the same, i.e.:

$$\frac{K_1'}{k_2'} = \frac{K_1}{k_2} \tag{2.26}$$

k_2' can be replaced by k_2/R_1, and the model becomes identifiable. Thus the model parameters are R_1, k_2, k_3 and k_4.

FRTM: linearized

The FRTM can be linearized obtaining the following equation:

$$\begin{aligned} C_{VOI}(t) = -\vartheta_1 \int_0^t C_T(\tau)d\tau - \vartheta_2 \int_0^t \int_0^t C_T(\tau)d\tau d\tau + \vartheta_3 \int_0^t C_r(\tau)d\tau + \\ + \vartheta_4 \int_0^t \int_0^t C_r(\tau)d\tau d\tau + \vartheta_5 C_r(t) \end{aligned} \tag{2.27}$$

with:

$$\begin{aligned} \vartheta_1 &= k_2 + k_3 + k_4 \\ \vartheta_2 &= k_2 k_4 \\ \vartheta_3 &= (k_2 - R_1 k_2) \\ \vartheta_4 &= (k_2 k_3 + k_4 (k_2 - R_1 k_2)) \\ \vartheta_5 &= R_1 \end{aligned} \tag{2.28}$$

The parameters ϑ_1, ϑ_2, ϑ_3, ϑ_4 and ϑ_5 can be estimated with a linear least square estimator.

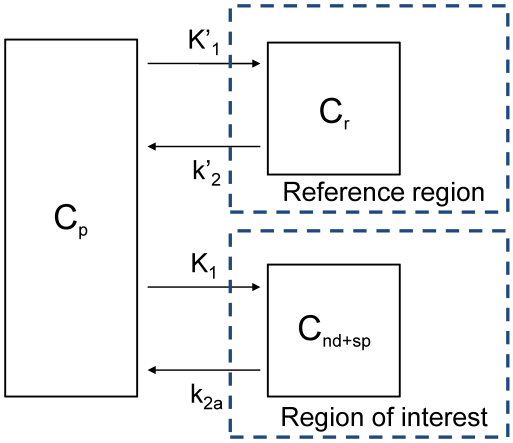

Figure 2.5: Simplified Reference Tissue Model (SRTM): K_1 (ml/g/min) and k_{2a} (min^{-1}) are the rate constants for tracer transport from plasma to tissue and return. K_1' (ml/g/min) and k_2' (min^{-1}) are the rate constant for transfer from plasma to reference compartment.

FRTM: basis functions

From the assumption described above, it is possible to obtain the 2.23 in basis function form, as:

$$C_{VOI}(t) = R_1 C_r(t) + \alpha_1 C_r(t) \otimes e^{-\beta_1 t} + \alpha_2 C_r(t) \otimes e^{-\beta_2 t} \tag{2.29}$$

with:

$$\begin{aligned} \alpha_1 &= \frac{(\beta_1 - k_3 - k_4)(k_2/R_1 - \beta_1)}{\beta_1 - \beta_2} \\ \alpha_2 &= \frac{(k_3 + k_4 - \beta_2)(k_2/R_1 - \beta_2)}{\beta_1 - \beta_2} \\ \beta_1, \beta_2 &= \frac{(k_2 + k_3 + k_4) \mp \sqrt{(k_2 + k_3 + k_4)^2 - 4k_2k_4}}{2} \end{aligned} \tag{2.30}$$

where R_1, α_1 and α_2 can be estimated with a linear estimator, assuming β_1 and β_2 as known, as in [2].

2.4.2 Simplified Reference Tissue Model

SRTM can be used when one compartment can reasonable describe the kinetics of the tracer in tissue ([21]). The SRTM presented in Figure 2.5 includes the

arterial plasma component (C_p), one tissue compartment (C_T) that incorporated the non displaceable fraction (nd) and a specific bound fraction (sp), and one reference component (C_r). The vascular component is considered negligible.
The model is based on the following differential equations:

$$\begin{aligned} \dot{C}_r(t) &= K_1' C_p(t) - k_2' C_r(t) & C_r(0) &= 0 \\ \dot{C}_T(t) &= K_1 C_p(t) - k_{2a}\, C_T(t) & C_T(0) &= 0 \end{aligned} \tag{2.31}$$

where K_1' is the rate constant for transfer from plasma to reference compartment (ml/g/min) and k_2' is the rate constant for transfer from reference to plasma compartment (min^{-1}). K_1 (ml/g/min) and k_{2a} (min^{-1}) are the rate constants for tracer transport from plasma to tissue and return, and $k_{2a} = \frac{k_2}{1+BP}$, with BP defined as in 2.25.
The parameters of the simplified model to be estimated are R_1, k_2 and BP.

SRTM: linearized

The SRTM can be linearized obtaining the following equation:

$$C_T(t) = -\vartheta_1 \int_0^t C_T(\tau)d\tau + \vartheta_2 \int_0^t C_r(\tau)d\tau + \vartheta_3 C_r(t) \tag{2.32}$$

with:

$$\begin{aligned} \vartheta_1 &= \tfrac{k_2}{1+BP} \\ \vartheta_2 &= k_2 \\ \vartheta_3 &= R_1 \end{aligned} \tag{2.33}$$

The parameters ϑ_1, ϑ_2 and ϑ_3 can be estimated with a linear least square estimator.

SRTM: basis functions

The SRTM model is generally solved using basis functions, as described originally in [2]:

$$C_T(t) = R_1 C_r(t) + \alpha_1 C_r(t) \otimes e^{-\beta_1 t} \tag{2.34}$$

with:

$$\begin{aligned} \alpha_1 &= \left[k_2 - \tfrac{k_2 R_1}{1+BP} \right] \\ \beta_1 &= \tfrac{k_2}{1+BP} \end{aligned} \tag{2.35}$$

In this form the model parameters R_1 and α_1 can be estimated with a linear estimator, assuming β_1 as known, as in [2].

Chapter 3

Novel approaches for Bayesian voxel-wise PET quantification

3.1 Bayesian PET modeling

The principle of Bayesian statistics is to incorporate prior knowledge about unknown model parameters in the estimation process, along with a given set of measured data.

In this context, the expression "Bayesian methods" is used when any kind of *a priori* information on the parameters is assumed known and used for the estimation. This knowledge can be obtained from operational or observational data, from previous comparable experiments or from physiological knowledge. When the prior information is derived from the data, the method is referred to as empirical Bayes.

The output of a generic dynamic system can be described in vectorial form by

$$\mathbf{y} = g(\mathbf{p}, \mathbf{t}) + \mathbf{v} \tag{3.1}$$

where $g(\mathbf{p}, \mathbf{t})$ represents the dynamic model of the system with m unknown parameters $\mathbf{p} = [p_1, p_2, \ldots, p_m]^T$ and $\mathbf{y}$ is the n-dimensional vector containing the

measures collected at times t_1, t_2, ..., t_n. The measures are affected by an additive error $\mathbf{v}$ which is assumed to be a zero mean Gaussian vector made of random variables v_1, v_2,..., v_n.

For the sake of simplicity the explicit dependence on time will be omitted, i.e. instead of indicating the function of m parameters p_i as $g(\mathbf{p}, \mathbf{t})$, the simpler $g(\mathbf{p})$ will be employed.

In the Bayesian approach, a probability density function $f_p(\mathbf{p})$ is associated to the unknown parameter vector $\mathbf{p}$ and it is assumed known.

It is possible to define the probability density function of the parameters vector given the data (called *a posteriori* distribution):

$$f_{p|y}(\mathbf{p}\,|\mathbf{y}) \tag{3.2}$$

that, according to Bayes' rule, can be written as:

$$f_{p|y}(\mathbf{p}\,|\mathbf{y}\,) = \frac{f_{y|p}(\mathbf{y}\,|\mathbf{p})f_p(\mathbf{p})}{f_y(\mathbf{y})} \tag{3.3}$$

where $f_y(\mathbf{y})$ is the prior probability density function of the measurements vector $\mathbf{y}$.

Maximum a Posteriori (MAP) estimator derives the estimates by maximizing Eq. 3.3:

$$\hat{\mathbf{p}}_{MAP} = \arg\max_p f_{p|y}(\mathbf{p}\,|\mathbf{y}) \tag{3.4}$$

where *arg max* stands for the argument of the maximum.

Using Bayes' rule and as $f_y(\mathbf{y})$ is independent from $\mathbf{p}$, the MAP estimator can be described as:

$$\hat{\mathbf{p}}_{MAP} = \arg\max_p f_{y|p}(\mathbf{y}\,|\mathbf{p})\ f_p(\mathbf{p}) \tag{3.5}$$

The expression for $f_{y|p}(\mathbf{y}\,|\mathbf{p})$ is simplified considerably if specific assumptions regarding the distributions of $\mathbf{v}$, $f_v(\mathbf{v})$, $\mathbf{p}$ and $f_p(\mathbf{p})$ are made. For instance, let

us assume that both $\mathbf{v}$ and $\mathbf{p}$ are independent and normally distributed. Then:

$$\hat{\mathbf{p}}_{MAP} = \arg\min \left[\mathbf{y} - G(\mathbf{p})\right]^T \Sigma_v^{-1} \left[\mathbf{y} - G(\mathbf{p})\right] + (\mathbf{p} - \mu_p)^{-1} \Sigma_p^{-1} (\mathbf{p} - \mu_p) \quad (3.6)$$

where $G(\mathbf{p})$ indicates the structural model of the system, $\mathbf{z}$ the vector of the measured data, Σ_v the covariance matrix of the measurement error, $\mathbf{p}$ the vector of the model parameters. μ_p and Σ_p are, respectively, the mean and covariance of the prior probability of $\mathbf{p}$.
This prior information is updated from the observed data, generating the *a posteriori* probability density function. Thus the MAP estimator realizes a compromise between the *a priori* and *a posteriori* information.

As said, the Bayesian methods require an assumption on the *a priori* probability distribution of $\mathbf{p}$.
It is common practice in PET modeling to use the terms "Bayesian" and "prior" in a wider sense: not only when *a priori* information is available on the probability density function of the unknown parameter vector itself, but also when it is possible to obtain some kind of a *a priori* knowledge on the tracer kinetics. This was the approach used and developed in Section 3.3.

In Bayesian methods for quantitative PET, the major problem is how to derive the *a priori* knowledge, i.e. μ_p and Σ_p (mean and covariance of $\mathbf{p}$), because there is not a unique way.
The *a priori* information can be derived from *in vitro* data, or from literature, or as in [7] from a previous voxel-based analysis of subjects sharing similar characteristics using the mean and standard deviation (SD) value of the voxel estimates to represent the *a priori* probability of the parameters of each voxel of the subject under analysis.
An alternative approach is to assume that the voxels belonging to a ROI have to share similar proprieties and will have estimates similar to those obtained by

using the mean TAC derived from the ROI itself. This is not a novel approach but it can be found in [6], [32] and [33] where the voxel is considered as an individual in a population and assuming that it shares certain characteristics with the other individuals belonging to the same population (i.e. the ROI).
Consequently the priors are different for each subject of the dataset, and moreover they are different for each ROI and they allow taking into account the inter-ROI variability.

The proposed approaches are both developed following a multi-stage hierarchical scheme where, starting from the kinetic analysis of the whole brain, information is cascaded to anatomical systems that are akin in terms of receptor densities, and then down to the voxel level.
A priori classes of voxels are generated either by anatomical atlas segmentation or by functional segmentation using unsupervised clustering.

The anatomical atlas is a standardized space where each voxel is labeled to the ROI which it is more likely to belong to. The regions are already defined and they can be applied easily to PET images. The atlas used for this work was the Maximum Probability Hammersmith BrainAtlas, developed by [27], made available by the Imperial College.
To extract functional information, various algorithms were implemented. For the majority of the tracer the k-means partitioning method ([34]), widely used for pattern recognition, was appropriate for the ROI definition.
In alternative, the Fuzzy C-Means partitioning method ([35], [36]) was considered, in its original version or combined with k-means method (details given in Section 4.2 and Chapter 5).

A representation of the hierarchical process is presented in Figure 3.1. The PET image was segmented using either anatomical or functional information. For each

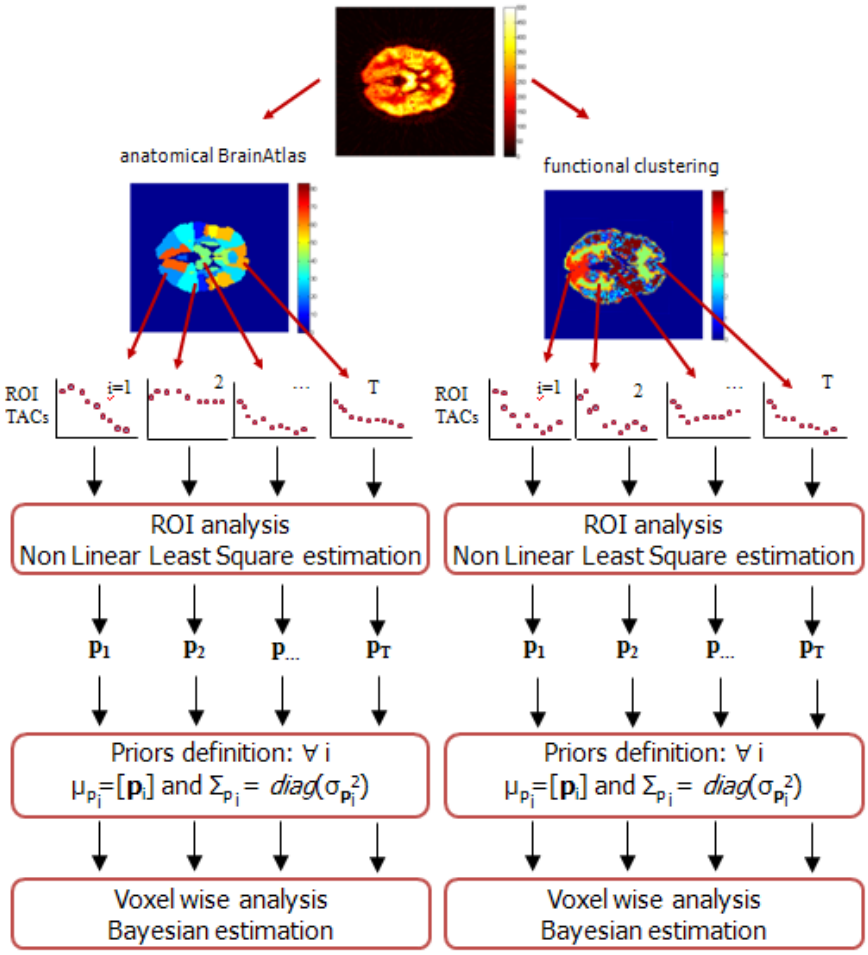

Figure 3.1: Pipeline describing the hierarchical process. The PET image is segmented using either anatomical or functional information. The ROI TACs are extracted from the regions (or clusters) and the optimal model used to describe the data is solved for each ROI with WNLLS. From the ROI estimates $\mathbf{p_i}$, one set of prior is defined for each region with $\mu_p = \mathbf{p_i}$ and $\Sigma_p = diag(\sigma^2_{\mathbf{p_i}})$. The voxel-wise analysis is then implemented, using as prior the one defined for the region which the voxel belongs to.

ROI ($ROI_1, ROI_2, \ldots, ROI_T$, with T number of region which the brain was segmented into) the mean TAC was extracted from the regions (or clusters) and the optimal model used to describe the data was solved with a weighted nonlinear least square estimator (WNLLS). From the ROI analysis, one set of estimated parameter vectors was obtained for each region (i.e., $\mathbf{p_i}$), and from these values one set of priors was defined for each region with $\mu_p = \mathbf{p_i}$ and $\Sigma_p = diag(\sigma^2_{\mathbf{p_i}})$. The voxel-wise analysis was then implemented, using as prior the one defined for

the region which the voxel belongs to.

3.2 Hierarchical Maximum a Posteriori (H-MAP)

Hierarchical MAP is a new hierarchical approach for the generation of PET parametric maps where the estimates are obtained using a linear MAP estimator applied at the voxel level. The method can be applied to any linear or linearized PET model described in Chapter 2. The priors for the Bayesian estimator are generated automatically from the data, and as a consequence are user-independent.

As described in Chapter 3, H-MAP requires at first the model to be solved at the ROI level. For each region, the mean TAC is extracted and the model is identified with a non linear estimator, which represents the gold standard.
The model is then linearized and solved at voxel level using the MAP estimator of Eq. 3.6 to account for the bias introduced with the linearization of the model. The solution of Eq. 3.6 for a linear model leads to a closed form ([37], [38]):

$$\hat{\mathbf{p}}_{MAP} = \left(\mathbf{G}^T\Sigma_v^{-1}\mathbf{G} + \Sigma_p^{-1}\right)^{-1}\left(\mathbf{G}^T\Sigma_v^{-1}\mathbf{C_T} + \Sigma_p^{-1}\mu_p\right) \tag{3.7}$$

where C_T is the nx1 vector with the noisy measures, $G(\mathbf{p})$ is the predicted model output with size depending on the model used, n is the number of the tissue measures. The measurement error is assumed to be additive, uncorrelated, from a Gaussian distribution with zero mean and covariance matrix Σ_v, a nxn diagonal matrix estimated *a posteriori*, according to a relative weighting scheme, where Σ_v is known less than a scale factor γ ([39], [40]). $\mathbf{p}$ is the unknown parameter vector having a normal prior probability with mean μ_p and covariance matrix Σ_p, which is defined diagonal.
The prior knowledge (i.e. μ_p and Σ_p) is extracted from the PET data. The

estimates obtained at ROI level are used to define one set of priors for the MAP estimator for each region. The mean μ_p of the normal prior distribution is set equal to the estimates obtained with WNLLS for the mean TAC.
The covariance matrix Σ_p is calculated directly from the standard deviation of the accuracy of the WNLLS estimates. The accuracy relates the variability of the estimates to the expected variability of the measurements. Thus, its value is assumed to represent the uncertainty associated with μ_p.

3.3 Hierarchical Basis Function Method (H-BFM)

Hierarchical Basis Funtion Method (BFM) is a new hierarchical method for PET quantification to apply BFMs to mono- and multi-compartmental models. The method allows to solve the compartmental model at voxel level in its non linear version, overcoming the limitations related to the grids described in Chapter 1, making them user-independent and subject and ROI specific.
This method is considered a Bayesian approach in PET, even if it does not rely on a Bayesian estimator, because additional information are added to the data to be analyzed. In particular, the grids used to create the basis functions for the analysis at voxel level are defined from the information obtained solving the model at ROI level, in a hierarchical top-down approach. Consequently, even if the *a priori* knowledge is not on the actual parameters to be estimated, the grid selection implies to determinate an interval of physiologically plausible values.

As for H-MAP, following Chapter 3, at first the model is solved at the ROI level for each region with a non linear estimator (gold standard).
For each time frame ($i = 1,\ldots, n$, with n number of frames), basis functions can be pre-calculated for the non linear terms involving $C_p(t)$ (or $C_r(t)$, if a reference

input model is considered) as:

$$B_{jl}(t_i) = C_p(t_i) \otimes e^{-\beta_{jl} t_i} \qquad l = 1, \ldots, M \tag{3.8}$$

with M number of elements of the grid, $j = 1$ for 1T and 3K model and $j = 2$ for 2T model.

The local grids for the basis functions for the voxel-by-voxel analysis are defined *a priori*, generated automatically from the data, specifically for each ROI, from the estimates obtained with the ROI analysis.

The exponent coefficients β_j of each convolution of the measurement equation are evaluated from the ROI estimated individual rate constants and one grid for each convolution for each ROI is defined. The grids are created based on a sampling of Gaussian distributions, whose means are the exponents estimated at ROI level and the standard deviations are calculated directly from the precision of the estimates.

An example of the grid definition for the 2T model (i.e. the more complex model

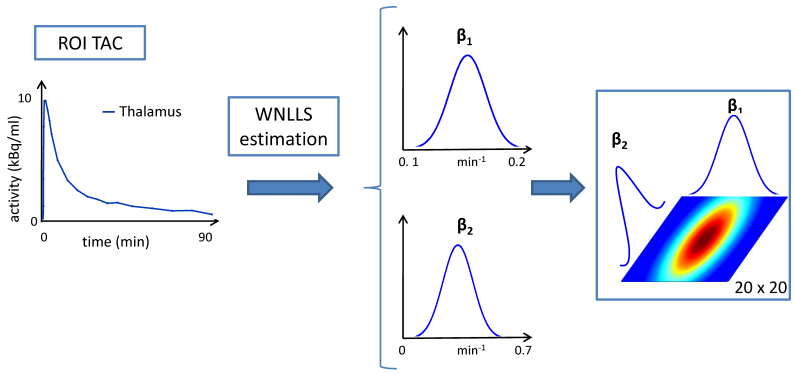

Figure 3.2: Pipeline describing the grid definition.

in PET receptor studies, which requires two convolutions to be solved) is presented in figure 3.2.

As in general it is not possible to make any assumption on the correlation of β_j,

the grids are defined 2-dimensional. Consequently the size of the grids is to be chosen appropriately, such a way to not be too computational demanding, but to give enough information to describe the data.

The model expressed in basis functions is then solved with linear least squares for each element of the grids, calculating the Weighted Residual Sum of Squares (WRSS), as in [2]:

$$WRSS_l = \sum_{i=1}^{n} w_i \left[C_T(t_i) - C_l(t_i)\right]^2 \tag{3.9}$$

where C_T is the nx1 vector of the measures, w_i is the inverse of the measurement error variance and C_l is the model output for the l^{th} element of the grids. The best solution is the one which minimizes WRSS and the individual kinetic rate constants are calculated from the estimated α_j.

Chapter 4

Image Acquisition and Processing

4.1 Datasets and Processing

4.1.1 [^{11}C]DPN (Opioid receptor ligand)

[^{11}C]DPN is a reversible non-subtype selective antagonist at opioid receptors and has often been used, mainly in studies of pain, neurodegeneration, epilepsy and addiction ([41]). It has high affinity at μ, κ and δ opioid receptors ([42], [43]), being an antagonist at μ and δ subtypes, but has a weak efficacy at the κ opioid receptor, where it acts as a partial agonist ([44]).

[^{11}C]DPN has rapid cerebral uptake and in humans, *in vivo*, it has high uptake in regions such as thalamus, temporal, frontal, and parietal cortices, which are known from post mortem studies to have high concentrations of μ, κ and δ opioid receptors ([42]). Relative to the duration of a PET study, [^{11}C]DPN has very slow kinetics, with binding close to irreversible, representing a challenge to the estimation of the parameters of interest, particularly at the voxel level.

PET studies

Data from previously reported studies ([45]) of five healthy control subjects (each of them scanned twice) were made available by the Imperial College. The criteria for subject inclusion and the procedure for [^{11}C]DPN PET studies are described in detail in [45]. Briefly, all subjects underwent paired 90-min dynamic [^{11}C]DPN PET test-retest scans on a Siemens/CTI ECAT EXACT3D PET camera. Acquisition was performed in list-mode (event by event) and scans were rebinned into 32 time frames of increasing duration (variable length background frame, 3 x 10s, 7 x 30 s, 12 x 120 s, 6 x 300 s, 3 x 600 s).

The subjects were positioned optimally within the field of view and thirty seconds after the scan start they were injected with $\sim$ 185 MBq (185 $\pm$ 4, range 181 - 191) of [^{11}C]DPN over a total of 30 s. Data were reconstructed using the reprojection algorithm ([46]) and then corrected for movement. The reconstructed voxel sizes were 2.096 mm x 2.096 mm x 2.43 mm.

Arterial blood was continuously withdrawn at a sampling rate of 5 ml/min for the first 15 min, then discrete blood samples were taken in all subjects for cross calibration and for determination of blood radioactivity at 5, 10, 15, 20, 30, 40, 50, 60, 75 and 90 min after start of scan. Seven of these samples were also used for quantification of the fraction of radioactivity attributable to unmetabolized parent radiotracer, generating the metabolite-corrected arterial plasma input function for all subjects.

The tissue, blood and plasma data were corrected for decay of ^{11}C.

Anatomical ROI segmentation

Each subject also had high-resolution 3D T1 weighted MR scans. The MRI data sets were used only for region definition, using Statistical Parametric Mapping (SPM8, Wellcome Department of Imaging Neuroscience, Institute of Neurology,

UCL, London, UK), running under Matlab®(The Mathworks Inc., Natick, MA, USA).

An individualized Maximum Probability Hammersmith Brain Atlas ([27]), based on thirty atlas data sets subdivided into 83 anatomical regions each ([47]) in standard stereotaxic space (MNI/ICBM 152), was created for every subject and provided already in the individual MRI space. The rigid transformation for MRI-to-PET coregistration was then derived from SPM8's normalized mutual information option ([48]) and applied to the original MRI and the transformed maximum probability atlas, resulting in all the images being in register with the given unchanged PET image data set. Finally the atlas was multiplied in PET space and the 83 ROIs TACs were derived, obtained meaning the voxel TACs belonging to each of the 83 anatomical regions.

The regions were chosen following previous studies ([49], [45]): one small central structure with high opioid receptor density (thalamus), one larger region from the frontal cortex with intermediate signal (inferior frontal gyrus), two regions with low signal (cerebellum and brainstem), one region from the occipital cortex with minimal receptor density (lingual gyrus), one small anisotropic region with special interest in epileptology and memory research (hippocampus) and another small region among the central structures (putamen). For comparison with previous published data left and right regions combined were considered.

4.1.2 [^{11}C]FLB457 (Dopamine receptor ligand)

[^{11}C]FLB457 is a radioligand for quantification of dopamine D_2/D_3 receptor binding in extrastriatal brain regions and it is used mostly in research studies on neuropsychiatric disorders.

Extrastriatal dopamine receptors have since long been proposed as targets for antipsychotic drugs ([50]) and neuroimaging and pharmacological evidence has supported the view that limbic cortical dopamine D_2/D_3 receptors may be the main target of antipsychotic medication ([51], [52], [53]).

Quantification of dopamine receptors in extrastriatal regions is generally hampered by the low receptor density which in most such regions is 1 to 10% of that in the striatum ([54]), thus it is necessary a radioligand with very high affinity to accurately measure small receptor densities in regions that can also have small volume.

[^{11}C]FLB457 is a substituted benzamide with very high affinity for D_2/D_3 dopamine receptors, whereas the affinity to other putative central receptors is negligible ([55]). It can be used to visualize and quantify low density dopamine receptor populations in the human brain and the distribution of radioactivity is consistent with the known distribution of dopamine D_2/D_3 receptors ([54]).

PET studies

Data from previously reported studies ([56]) of four depressed subjects were made available by the Imperial College. The criteria for subject inclusion and the procedure for [^{11}C]FLB457 PET studies are described in detail in [56].

Briefly, four depressed subjects underwent a 90-min dynamic PET study in a CTI ECAT EXACT3D tomography after a bolus injection of 280 MBq to 380 MBq of [^{11}C]FLB 457. All PET data were acquired in 3-dimensional mode, corrected for attenuation, detector efficiency, random events, and scatter, and reconstructed into tomographic images using filtered back-projection.

Acquisition was performed in list-mode (event by event) and scans were rebinned into 32 time frames of increasing duration (variable length background frame, 9 x 10 s, 4 x 30 s, 2 x 60 s, 2 x 120 s, 1 x 180 s, 10 x 300 s, 3 x 600 s). The reconstructed voxel sizes were 2.096 mm x 2.096 mm x 2.43 mm.

After injection of [^{11}C]FLB457 the radioactivity concentration in blood was measured continuously and in addition serial discrete blood samples were taken at increasing time intervals throughout the study for the measurement of the radioactivity in blood and plasma. Eight of these samples were also used for quantification of the fraction of radioactivity attributable to unmetabolized parent

radiotracer, generating the metabolite-corrected arterial plasma input function for all subjects.

The tissue, blood and plasma data were corrected for decay of ^{11}C.

Anatomical ROI segmentation

Each subject also had high-resolution 3D T1 weighted MR scans. The MRI data sets were used only for region definition, using SPM8, running under Matlab.

A Maximum Probability Brain Atlas ([27]) subdivided in 73 regions defined in standard stereotaxic space (MNI/ICBM152) was used to define the ROI. The MR MNI template was normalized to each subject's MR image using SPM8 and the atlas was applied to the subject's MR space by applying the normalization parameters. Then for each subject, the MRI was coregistered to the summed PET using SPM8, with normalized mutual information option ([48]) and the normalization parameters were applied to the transformed maximum probability atlas, resulting in all the images being in register with the given unchanged PET image data set. Finally the atlas was multiplied in PET space and the 73 ROIs TACs were derived, obtained meaning the voxel TACs belonging to each of the 73 anatomical regions.

Following previous studies ([54]) the hippocampus, amygdale, cerebellum, thalamus, frontal cortex, temporal cortex and anterior cingulate were selected. The right and left hemispheres were considered combined.

The striatum was not considered because the study duration was shorter than the time required to reach equilibrium in this D_2/D_3 receptor-rich region ([57]).

4.1.3 [^{11}C]WAY100635 (Serotonin receptor ligand)

[^{11}C]WAY100635 (from here on, [^{11}C]WAY100635 indicates [*carbonyl*-C^{11}]WAY-100635) is a selective antagonist with high affinity and selectivity for serotonin 5HT$_{1A}$ receptors, which are of central interest in research on the pathophysiology and treatment of psychiatric disorders ([58], [59]).
[^{11}C]WAY100635 provides high-contrast delineation of brain regions that are rich in 5-HT$_{1A}$ receptors ([60]) It shows rapid clearance of the compound from the cerebellum and high uptake in cortical and raphe regions. It also presents rapid clearance from plasma [61].

PET studies

A dataset of four healthy male subjects was made available by the Imperial College. Each subject underwent a 90-min dynamic PET study in a CTI ECAT EXACT3D tomography after a bolus injection of [^{11}C]WAY 100635. All PET data were acquired in 3-dimensional mode, corrected for attenuation, detector efficiency, random events, and scatter, and reconstructed into tomographic images using filtered back-projection.
Acquisition was performed in list-mode (event by event) and scans were rebinned into 23 time frames of increasing duration (two variable length background frame, 3 x 5 s, 2 x 15 s, 4 x 60 s, 7 x 300 s, 5 x 600 s). The reconstructed voxel sizes were 2.096 mm x 2.096 mm x 2.43 mm.
After injection of [^{11}C]WAY100635 , the radioactivity concentration in blood was measured continuously and in addition serial discrete blood samples were taken at increasing time intervals throughout the study for the measurement of the radioactivity in blood and plasma. Nine of these samples were also used for quantification of the fraction of radioactivity attributable to unmetabolized parent radiotracer, generating the metabolite-corrected arterial plasma input function

for all subjects.

The tissue, blood and plasma data were corrected for decay of ^{11}C.

Anatomical ROI segmentation

Each subject also had high-resolution 3D T1 weighted MR scans. The MRI data sets were used only for region definition, using SPM8, running under Matlab.
As for the dataset of [^{11}C]FLB 457, a Maximum Probability Brain Atlas ([27]) subdivided in 73 regions was used to define the ROI, with the same procedure as in Section 4.1.2. The atlas was registered on PET space as described above and the 73 ROIs TACs were derived, obtained meaning the voxel TACs belonging to each of the 73 anatomical regions. The ROIs were selected on the base of previous studies: cerebellum, thalamus as region with low binding and insula cortex, cingulate cortex, frontal cortex, raphe nucleus, temporal cortex as regions rich of $5HT_{1A}$ receptor ([62]). Right and left hemispheres were considered combined.

4.1.4 [^{11}C]SCH442416 (Adenosine receptor ligand)

[^{11}C]SCH442416 is a nonxanthine radioligand which binds selectively and reversibly to striatal A_{2A} receptors, which are abundant in basal ganglia, vasculature and platelets ([63]). A_{2A} receptor interacts structurally and functionally with the dopamine D_2 receptor and this interaction is of particular interest as it is thought to be central to basal ganglia dysfunction in Parkinson's disease. ([64]).
Preclinical studies on rats and nonhuman primates suggest that [^{11}C]SCH442416 is suitable for the *in vivo* imaging of adenosine A_{2A} receptors with PET because of its high affinity and selectivity, good signal-to-noise ratio, and low levels of radioactive metabolites in the brains ([63],[65]).
To the author's knowledge, there are only few previous works where [^{11}C]SCH-442416 data were analyzed in humans: in [66] data from 15 healthy subjects were

analyzed with kinetic modeling, to demonstrate the efficacy of vipadenant as potential treatment of Parkinson's disease. In [67] and [68] 4 normal subjects and 12 patients with Parkinson's disease with and without levodopa-induced dyskinesia respectively were studied with spectral analysis.
Nevertheless a proper analysis to identify the optimal compartmental model to describe the data has never been carried out. A preliminary work was proposed in [69] in which both data- and model-driven methods were used.

PET studies

Data of [^{11}C]SCH442416 of six healthy subjects were made available by the Imperial College. Each subject underwent a 90-min dynamic PET scanning in a Siemens ECAT EXACT HRD scanner after a bolus injection of an average of 612 MBq of [^{11}C]SCH442416 over 10 seconds, 30 seconds after the start of the scan. All PET data were acquired in 3-dimensional mode, corrected for attenuation, detector efficiency, random events, and scatter, and reconstructed into tomographic images using filtered back-projection.
Acquisition was performed in list-mode (event by event) and scans were rebinned into 34 time frames of increasing duration (variable length background frame, 6 x 10s, 3 x 20s, 3 x 30s, 4 x 60s, 6 x 120s, 8 x 300s, 3 x 600s). The reconstructed voxel sizes were 2.096 mm x 2.096 mm x 2.43 mm.
After injection of [^{11}C]SCH442416 the radioactivity concentration in blood was measured continuously for the first 15 minutes with discrete blood samples taken at baseline, 5, 10, 15, 20, 30, 40, 50, 60, 75, and 90 minutes. Eight of these samples were also used for quantification of the fraction of radioactivity attributable to unmetabolized parent radiotracer, generating the metabolite-corrected arterial plasma input function for all subjects.
The tissue, blood and plasma data were corrected for decay of ^{11}C.

Anatomical ROI segmentation

Each subject had a volumetric T1-weighted MRI performed with a Philips 1.5 T Eclipse system. The MRI data sets were used only for region definition, using SPM8, running under Matlab.

The same procedure used for [^{11}C]FLB457 and [^{11}C]WAY100635 data as in Section 4.1.2 was also applied for the ROI segmentation for this dataset. A Maximum Probability Brain Atlas ([27]) subdivided in 73 regions was registered on PET space as described above and the 73 ROIs TACs were derived, obtained meaning the voxel TACs belonging to each of the 73 anatomical regions.

The ROIs selected for the analysis were cerebellum, thalamus, frontal and temporal cortices, anterior cingulate, pallidum and striatum. Right and left hemispheres were considered combined.

4.1.5 [^{11}C]MDL100907 (Serotonin receptor ligand)

[^{11}C]MDL100907 is a high affinity PET ligand which allowed an improvement in the *in vivo* quantification of 5-HT$_{2A}$ receptor, which has been localized throughout the brain, including cortical regions, prefrontal cortex, caudate nucleus, nucleus accumbens, olfactory tubercle and hippocampus ([70]).

Previous studies with [^{11}C]MDL100907 have revealed high-quality images of receptor availability, which correspond well with the known distribution of 5-HT$_{2A}$ binding sites from post-mortem studies ([71], [72]). [^{11}C]MDL100907 is a competitive antagonist with subnanomolar affinity for 5-HT$_{2A}$ receptor at least 100 times higher than the affinity for the other 5-HT receptors. Imaging studies in man have shown that it binds specifically to 5-HT$_{2A}$ receptors with high specific to nonspecific binding ([73]). The 5-HT$_{2A}$ receptor has been implicated in the pathophysiology of various neuropsychiatric disorders, including schizophrenia, major depression, anxiety, sleep disorders and Obsessive Compulsive Disorder

(OCD) ([74], [75], [76]). Both postmortem and brain imaging studies have evidenced the role of 5-HT_{2A} receptor in the pathophysiology of depressive illness and in the action of antipsychotics ([77]).

PET studies

We analyzed [^{11}C]MDL100907 binding to 5-HT_{2A} receptors *in vivo* in two different datasets, made available by Imperial College of London (UK) and by San Raffaele Scientific Institute (HSR) of Milan (Italy).

Imperial dataset Data from previously reported studies ([78]) of six healthy control subjects were used in the current study. The criteria for subject inclusion and the procedure for [^{11}C]MDL100907 PET studies are described in detail in [78]. Briefly, six healthy subjects undergone twice a 90-min PET scan in a ECAT EXACT3D scanner following injection of 361 MBq of [^{11}C]MDL100907 (under baseline condition and after administration of a single dose of mirtazapine, a 5-HT_{2A} blocking). Mirtazapine is an antidepressant, which acts by blocking 5-$HT_{2A/2C}$ and 5-HT_3 receptors ([79]).

For all the PET exams at baseline plasma input functions were available. Only for one subject the plasma input function was available after administration of mirtazapine, consequently it was used only as case study and to validate the effect of the blockade on the tracer binding. Acquisition was performed in list-mode (event by event) and scans were rebinned into 28 time frames of increasing duration (30 s background frame before injection, then 3 x 10 s, 3 x 20 s, 3 x 30 s, 3 x 60 s, 4 x 120 s, 6 x 300 s and 5 x 600 s). The reconstructed voxel sizes were 2.096 mm x 2.096 mm x 2.43 mm.

Arterial whole-blood activity was continuously withdrawn for the first 15 min then discrete blood samples were taken in all subjects at 5, 10, 15, 20, 30, 40, 50, 60, 75 and 95 min. Eight of these samples were also used for quantification of the

fraction of radioactivity attributable to unmetabolized parent radiotracer, generating the metabolite-corrected arterial plasma input function for all subjects.
The tissue, blood and plasma data were corrected for decay of ^{11}C.

HSR dataset HSR dataset consisted in both healthy subjects and drug-naïve OCD patients. In particular, 6 healthy subjects, 3 of them scanned twice in baseline condition, and 12 OCD patients, scanned twice (baseline condition and after administration of fluvoxamine) were available. Fluvoxamine is a potent Selective Serotonin Reuptake Inhibitor (SSRI) with high affinity for the serotonin transporters and negligible affinity for the dopamine transporter or any other receptor. Plasma input functions were available for four of the healthy subjects for the first PET exam.
All subjects underwent a 90-min PET in a GE Advance scanner after injection of 190 to 370 MBq of [^{11}C]MDL100907 . After tracer injection, 17 sequential of increasing length were acquired (4 x 60 s, 3 x 120 s, 6 x 300 s, 2 x 600 s, 2 x 900 s). Trans-axial images were reconstructed using a Shepp-Logan filter (cut-off 5 mm filter width) in the transaxial plane, and a Shepp-Logan filter (cut-off 8.5 mm) in the axial direction. The reconstructed voxel sizes were 2.5 mm x 2.5 mm x 4.25 mm.
Twenty discrete blood samples were manually taken in 4 healthy subjects at specific times: 10 samples at close range until 1 min, then at 3, 5, 10, 20, 30, 40, 50, 60, 75 and 90 min. The concentration of the tracer in the plasma uncorrected for the metabolites was generated. Part of these measures in some subjects were also used for quantification of the fraction of radioactivity attributable to unmetabolized parent radiotracer, in order to generate the metabolite-corrected arterial plasma input function.
The tissue, blood and plasma data were corrected for decay of ^{11}C.

Anatomical ROI segmentation

Imperial dataset Each subject had high-resolution 3D T1 weighted MR scans in a 1 T Philips Medical Systems HPQ+ Scanner. The MRI data sets were used only for region definition, using SPM8, running under Matlab.
The same procedure described in Section 4.1.2 was also applied for the ROI segmentation for this dataset. A Maximum Probability Brain Atlas ([27]) subdivided in 73 regions was registered on PET space as described above and the 73 ROIs TACs were derived, obtained meaning the voxel TACs belonging to each of the 73 anatomical regions.
The following 9 ROI were chosen for generation of side-averaged regional TACs: hippocampus, amygdale, frontal cortex, temporal cortex, anterior cingulate, posterior lobe and occipital lobe (regions with high serotonin receptor density), thalamus (a region with intermediate signal) and cerebellum (a region with minimal receptor density).

HSR dataset For this dataset no MRI scans were available, so a Maximum Probability Brain Atlas ([27]) divided in 73 ROIs was used to generate the regions, as described in Section 4.1.2, coregistering the atlas on each individual summed PET scan, using SPM8. The same 9 regions already selected for the Imperial dataset were considered: hippocampus, amygdale, cerebellum, thalamus, frontal cortex, temporal cortex, anterior cingulate, posterior lobe and occipital lobe.

4.2 Automatic generation of ROIs: atlas vs cluster

In order to verify the sensitivity of the solution to the *a priori* information generated from the ROIs, an alternative segmentation was adopted that used functional instead of anatomical information through an unsupervised clustering that extracted kinetically homogeneous regions. In the unsupervised clustering, no representative patterns of the classes are known *a priori*.

Various partitioning approaches are available in literature, both supervised and unsupervised methods, such as Support Vector Machine (widely applied in bio-engineering studies, e.g. [80]), but in imaging these approaches can not be used at voxel level because too computationally heavy.
The most usable approaches that can be applied to PET images are k-means partitioning method ([34]) and Fuzzy C-Means partitioning method ([35], [36]).

In the partitioning (or non hierarchical) approach, the number of clusters in which the data will be divided must be defined by the user.
The first algorithm considered to define the clusters was the k-means partitioning method ([34]), which is widely used in imaging. It allows partitioning B observations into K ($K \leq B$) clusters, in which each observation belongs to the cluster with the nearest mean. It leads to a hard (exclusive) assignment, in which every observation is assigned to only one cluster.
The distance that must be minimized can be defined in various ways, the most common measure is the Euclidean distance, which was the one chosen as metric to separate the observations into different clusters.

Another partitioning method considered was the Fuzzy C-Means partitioning method ([35], [36]), implemented using the Euclidean distance as metric to separate the data into different clusters.
In this method, the assignment to a certain cluster is not exclusive (soft or overlapping assignment), i.e. for each data point the probability that it belongs to a certain cluster is obtained. The clusters are then defined using a deterministic threshold on the probability map: only the data which have more than a given probability to belong to a certain cluster are considered for that cluster, in the other case the data is discarded.

These methods were applied to [^{11}C]DPN and [^{11}C]FLB457 data on the whole

kinetic voxel TACs with good results, but when applied to noisier datasets did not performed well. Thus a solution *ad hoc* was developed, implementing a parametrization of the tracer's kinetics, considering the combination of both k-means and Fuzzy C Means. To the best of this author's knowledge this approach has never been applied to PET data and thus it represents a novelty.

The parameters used to characterize the voxel concentration curves were the Area Under the Curve (AUC), the slope and the intercept of the regression line of the last points of the voxel TACs.

This alternative clustering approach consisted in an initial functional segmentation of the parameters relative to the whole brain volume using the Fuzzy C-Means partitioning method, using the Euclidean distance as metric to separate the data into different clusters. Different values for the threshold to apply to the probability map were evaluated, ranging from 80% to 95%.

Moreover the clusters were further segmented through an exclusive clustering approach: each cluster was divided in two sub-clusters using the k-means partitioning method, using the Euclidean distance as metric as for the Fuzzy C-Means. This new clustering method was applied successfully to both [^{11}C]WAY100635 , [^{11}C]SCH442416 and [^{11}C]MDL100907 data.

Chapter 5

Application on datasets

5.1 H-MAP on [^{11}C]DPN

H-MAP was applied on the [^{11}C]DPN dataset, whose kinetics are best described at voxel level by a 1T model (Figure 2.3). The parameter of interest was V_T, calculated according to Eq. 2.19.

The data were affected by a measurement error, which was assumed to be additive, uncorrelated, from a Gaussian distribution with zero mean and covariance matrix Σ_v, estimated as the square of the known standard deviation less than a scale factor γ.

The proportionality constant γ was estimated *a posteriori* as in [39] and [40].

Tracer arrival delay was calculated as in [81].

ROI analysis

As explained in Section 3.2, for each region, the 1T model was solved at the ROI level with WNLLS, using a Levenberg-Marquardt minimization procedure as implemented in Matlab. The relative weights for the individual data points were defined as the inverse of the variance of the decay-corrected activity, i.e. frame length over whole brain activity, as in [82].

In order to compare 1T ROI level estimates of V_T, the data were also analyzed

using a graphical method to have a reliable comparison term with the results at voxel level inside the same ROIs.

For the reversible [^{11}C]DPN tracer, the method of choice at ROI level was the Likelihood Estimation in Graphical Analysis (LEGA) ([83]), a bias free alternative to the Logan plot ([10]).

In LEGA, the original Logan plot equation is rearranged making the error term additive obtaining for $i = k, k+1, \ldots, n$:

$$R_i^* = \frac{\sum_{j=1}^{i-1} R_j^* (s_j - s_{j-1}) + \frac{1}{8} R_{i-1}^* (s_i - s_{i-1}) - \beta \int_0^{(s_i - s_{i-1})/2} C_p(s) ds}{\delta - \frac{3}{8} (s_i - s_{i-1})} \quad (5.1)$$

where n is the number of frames, R_i^* is the model or 'noise free' TAC which is fitted to the R_i (i.e. the measured noisy TAC) in the time t_i with $t_i = (s_i + s_{i-1})/2$ and s_i the end point of the i$^{\text{th}}$ PET scan frame. β and δ correspond to the slope (i.e. volume of distribution) and intercept of the Logan plot.

Thus, if the measurement error, ϵ, of the measured R_i values is assumed to be additive and Gaussian (i.e., $R_i = R_i^* + \epsilon_i, i = 1, 2, \ldots, n$), then the maximum likelihood estimator is obtained by minimizing with WNLLS the cost function $\sum_{i=k}^{n} w_i (R_i - R_i^*)$ where w_i is the inverse of the measurement error variance. In this implementation, w_i is defined as for the compartmental modeling quantitative process.

It is to be noted that here the same symbols used in the original paper are presented, i.e. R_i is to be intended as $TAC(t_i)$.

The optimal value for k (equivalent to the equilibrium point after which the Logan plot becomes linear) was chosen by visual inspection of several Logan plots and set to use the last 14 frames for the estimation.

Voxel analysis

The 1T model was linearized as in Eq. 2.20, and solved at voxel level using the MAP estimator of Eq. 3.7 to account for the bias introduced with the linearization of the model.

For the 1T model, the predicted model output $G(\mathbf{p})$ is:

$$G = \begin{bmatrix} \int_0^{t_1} C_p(\tau)d\tau & -\int_0^{t_1} C_T(\tau)d\tau \\ \int_0^{t_2} C_p(\tau)d\tau & -\int_0^{t_2} C_T(\tau)d\tau \\ \vdots & \vdots \\ \int_0^{t_n} C_p(\tau)d\tau & -\int_0^{t_n} C_T(\tau)d\tau \end{bmatrix} \tag{5.2}$$

with dimension nx2, C_T has dimensions nx1, Σ_v and Σ_p have dimensions nxn and 2x2 respectively, and μ_p is a 2x1 vector.

Thus, the required computational cost is comparable to that of a linear least squares estimator.

The relative weights at the voxel level, i.e. Σ_v^{-1}, were defined in the same way as at the ROI level. The unknown scale factor γ has been estimated as in ([39], [40]):

$$\gamma = \frac{WRSS(\hat{p})}{m - n_p + n_b}\frac{m}{n} \tag{5.3}$$

where $WRSS(\hat{p})$ is the weighted residual sum of squares evaluated at minimum, n is the number of measured data points, m the total number of data points, n_p the number of estimated parameters, n_b the number of Bayesian parameters.

While for least squares estimators γ does not have any impact on the parameter estimates, in a MAP context it is otherwise.

Thus, after deriving the MAP estimates by initializing γ to one, it was necessary to repeat the MAP estimation procedure, in order to obtain the final results.

These were computed by applying Eq. 3.7 in which the updated Σ_v takes into account the estimated γ value.

As described in Section 4.2, two different ways to derive the prior information were used and compared.

Voxel analysis extracting the priors via anatomical segmentation

The ROIs were defined using the Maximum Probability Hammersmith Brain Atlas, under the hypothesis that voxels being part of the same ROI are likely to have a similar kinetic behavior.
For each ROI the mean TAC was extracted and the 1T model was identified as described above. The resulting estimates were used to define one set of priors for the MAP estimator for each region. The mean μ_p of the normal prior distribution was set equal to the estimates obtained with WNLLS for the mean TAC. The covariance matrix Σ_p was calculated directly from the standard deviation of the accuracy of the WNLLS estimates.
The resulting voxel by voxel parametric images derived with MAP were then sampled in the seven regions described in Section 4.1.1.

Voxel analysis extracting the priors via functional clustering

In order to verify the sensitivity of the solution to the prior, an alternative segmentation was adopted, using the k-means partitioning algorithm on the whole tracer kinetics, as explained in Section 4.2. Once the kinetic curves of the cerebral volume were grouped into K clusters, the 1T model was identified with MAP, where the priors were Gaussian distributions whose means and covariance matrices were calculated with WNLLS on the mean TAC of each cluster, with the same settings as described above.

In Figure 5.1 the pipeline of the generation of the parametric maps is presented. The ROI TACs extracted in the two alternative ways (BrainAtlas and k-means clustering) are identified with 1T model and solved with WNLLS. A set of priors

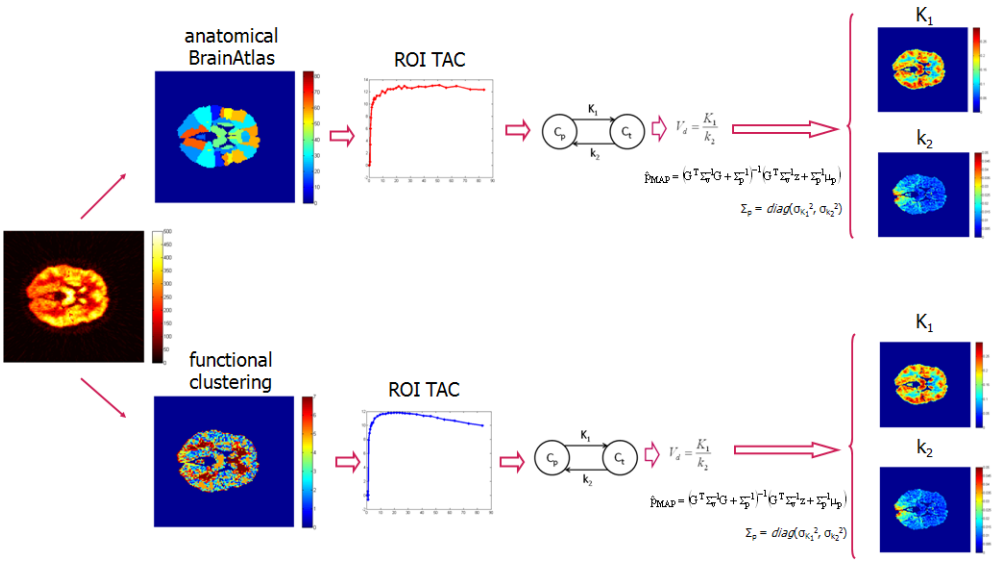

Figure 5.1: K_1 and k_2 parametric maps estimation pipeline. The dynamic PET images have been segmented using the anatomical Maximum Probability BrainAtlas or k-means clustering. The ROI TACs have been extracted and identified with the 1T model using WNLLS, obtaining the priors for the two parameters. From the MAP estimation of the linearized 1T model the parametric maps for K_1 and k_2 were obtained.

for each region is determined. At voxel level, the 1T model is solved with a MAP estimator, and the parametric maps for K_1 and k_2 are obtained. Finally, the volume of distribution is calculated according to Eq. 2.19.

Assessment of the estimates

For parametric maps resulting from both types of priors, values of $V_T < 0$ and $V_T > 100$ were not considered, because negative values of $V_T$have no biological explanation and values over 100 were clearly non-physiological, given the fact that the higher values in literature do not overcome 46.8 ml/g ([45]). Thus the upper bound was more than twice larger than the highest value reported in literature and for this reason the range was considered very large in such a way that outliers do not to have any impact on the final results.

The results obtained at the voxel level with priors extracted from the atlas and

the results obtained with priors extracted from functional clustering will be referred to as 'H-MAP A' and 'H-MAP C' respectively.

The H-MAP A estimates were compared with the results obtained at the ROI level using both LEGA and the 1T model estimated with WNLLS on each ROI's TAC. More in detail, for each ROI the V_T estimates obtained with H-MAP A were averaged in the voxels composing the ROI area, and these average values were compared to the ROI estimates.

The correlation among the results with a regression analysis was evaluated: the slope and the intercept of the fitted regression line with ROI LEGA as independent variable and the mean of H-MAP A in each ROI as dependent variable were calculated for each subject. Pearson's R^2 values were reported as the correlation measure.

For the assessment of the test-retest estimates, for each subject, slope and intercept of the fitted regression line were calculated, with the mean of test and retest H-MAP A estimates in each ROI as independent and dependent variable respectively. Pearson's R^2 values were added as correlation measures.

To evaluate the H-MAP C results the effects that the change of the method for extracting the priors has on the estimates were assessed, so the H-MAP C results were compared with the estimates obtained with H-MAP A and reported as percentage, according to:

$$difference\% = \frac{1}{N}\sum_{i=1}^{N} \frac{\frac{1}{P}\sum_{j=1}^{P} V_{T,cluster}^{i,j} - \frac{1}{P}\sum_{j=1}^{P} V_{T,atlas}^{i,j}}{\frac{1}{P}\sum_{j=1}^{P} V_{T,atlas}^{i,j}} * 100 \qquad (5.4)$$

where N is the number of subjects (considering test and retest together), P the number of voxels of the ROI, $V_{T,cluster}^{i,j}$ the value of the H-MAP C estimate in the j^{th} voxel for the i^{th} subject and $V_{T,atlas}^{i,j}$ the value of the H-MAP A estimate in the j^{th} voxel for the i^{th} subject. An additional criterion to evaluate the performance of H-MAP A and H-MAP C was the quantification of the coefficient of variation

of the parameters to assess their precision.

To further assess the reliability of the method the intraclass correlation coefficient (ICC) for repeated test-retest PET studies was also calculated:

$$ICC = \frac{MS(bs) - MS(ws)}{MS(bs) + MS(ws)} \tag{5.5}$$

where MS = mean sum of squares, bs = between subjects and ws = within subjects.

For test-retest data acquired under similar conditions, true intrasubject differences will be small, so high ICCs will be expected ([84]). We calculated ICCs using the 'one way random' model reporting the 'single measure' ICC.

5.2 H-BFM on [^{11}C]WAY100635 and [^{11}C]FLB457

H-BFM was tested on both [^{11}C]FLB457 and [^{11}C]WAY100635 datasets. For these tracers the optimal model to describe the kinetic behavior in the brain was the 2T model (Figure 2.1, of Eq. 2.1 and Eq. 2.2). The parameter of interest was V_T, calculated according to Eq. 2.3.

The data were affected by a measurement error, which was assumed to be additive, uncorrelated, from a Gaussian distribution with zero mean and covariance matrix Σ_v, estimated as the square of the known standard deviation less than a scale factor γ. The proportionality constant γ was estimated *a posteriori* as in [39] and [40] according to Eq. 5.3. As no Bayesian estimator is employed, $m = n$ and $n_b = 0$.

Basis Functions

As explained in Section 3.3, the 2T model was at first solved at the ROI level for each region with WNLLS, using a Levenberg-Marquardt minimization procedure

as implemented in Matlab.

The relative weights for the individual data points were defined as the inverse of the variance of the decay-corrected activity, i.e. frame length over whole brain activity, as in [82].

The local grids for the basis functions were generated automatically from the data, from the estimates obtained at ROI level, according to Figure 3.2.

The exponent coefficients β_1 and β_2 of the two convolutions were evaluated from the ROI individual rate constants as in Eq. 2.8 and from these values one grid for each convolution of the measurement equation for each region was defined. The grids were created 2-dimensional, based on a sampling of Gaussian distributions, whose means are the exponents estimated at ROI level and the standard deviations are calculated directly from the precision of the estimates.

The size of the grids was chosen appropriately to limit the required computational time but also to give enough information for the voxel-wise analysis. The size was set equal to 20x20.

Then starting from Eq. 2.7 for each time frame ($i = 1, \ldots, n$, with n number of frames), basis functions were pre-calculated for the non linear terms involving $C_p(t)$ according to Eq. 3.8, obtaining one set of $B_{1l}(t)$ and $B_{2l}(t)$, for each element $l = 1, \ldots, M$ of the grids β_1 and β_2 (as defined in Eq. 2.8).

Thus, Eq. 2.7 became:

$$C_{VOI} = [B_{1l}\ B_{2l}\ C_b] \begin{bmatrix} \alpha_1 \\ \alpha_2 \\ V_b \end{bmatrix} \tag{5.6}$$

where C_{VOI} is the vector of the measures with dimension nx1, C_b has dimension nx1 and the parameters to be estimated are α_1, α_2 and V_b. B_{1l} and B_{2l} are the nx1 basis functions for the two convolutions for the l^{th} element of the grids,

defined as in Eq. 3.8 as:

$$B_{jl}(t_i) = C_p(t_i) \otimes e^{-\beta_{jl} t_i} \qquad l = 1, \ldots, M \tag{5.7}$$

Eq. 5.6 was then solved with weighted linear least squares for each element of the grids, choosing as best solution the one which minimizes the WRSS (Eq. 3.9), as in [2] and the individual kinetic rate constants were calculated from the estimated α_1 and α_2.

Voxel analysis extracting the priors via anatomical segmentation

The ROIs were defined using the Maximum Probability Brain Atlas and for each ROI the mean TAC was extracted and the 2T model was identified as described in the previous section. The resulting estimates were used to define two grids for the basis functions for each region, based on the sampling of Gaussian distributions.

The mean was set equal to the estimates obtained with WNLLS for the mean TAC. The covariance matrix was calculated directly from the standard deviation of the accuracy of the WNLLS estimates.

The resulting voxel by voxel parametric images derived with H-BFM were then sampled in the seven regions selected for [^{11}C]FLB457 and [^{11}C]WAY100635 dataset, as described in Section 4.1.2 and Section 4.1.3 respectively.

Voxel analysis extracting the priors via functional clustering

In order to investigate the impact of varying the grid specifications, an alternative cluster segmentation was implemented, applying the k-means partitioning algorithm on the whole tracer kinetics of [^{11}C]FLB457 dataset, as explained in Section 4.2.

Instead, on [^{11}C]WAY100635 dataset a more complex clustering algorithm based

on the parametrization of the kinetics was implemented, as described in Section 4.2. The slope and the intercept of the regression line were evaluated on the last 5 points of the voxel TACs, corresponding to the last 40 minutes of the PET exam. The threshold applied to the probability map obtained from the Fuzzy C-means was set equal to 85%, an high value not too restrictive.

Once the kinetic curves of the cerebral volume were grouped into K clusters, the 2T model was identified with H-BFM, where the grids were created from the sampling of Gaussian distributions whose means and covariance matrices were calculated with WNLLS on the mean TAC of each cluster, with the same settings as described above.

Assessment of the estimates

For parametric maps resulting from both types of grids, for both datasets, values of $V_T < 0$ were not considered, because negative values have no biological explanation. Moreover a higher bound for V_T was set, i.e. $V_{Tcutoff} = 25$ for [^{11}C]FLB457 and $V_{Tcutoff} = 10$ for [^{11}C]WAY100635 , as values for the volume of distribution higher than the cutoff are clearly non-physiological.

In fact for these tracers the maximum values of V_T in literature are 16.2 ml/g and 6.7 ml/g respectively ([56], [62]) and the bounds were 50% higher than these values, resulting in a very large range in order for outliers to not have any impact on the final results.

The results obtained at the voxel level with grids extracted from the atlas and the results obtained with grids extracted from functional clustering will be referred to as 'H-BFM A' and 'H-BFM C' respectively.

The H-BFM A estimates were compared with the results obtained at voxel level using 2T model solved with WNLLS at voxel level. More in detail, for each ROI the V_T estimates obtained with H-BFM A in the voxels composing the ROI area were averaged, and these average values were compared to the average of the V_T

estimates obtained with WNLLS in the same voxels.

The correlation among the results was evaluated with a regression analysis: the slope and the intercept of the fitted regression line with the mean of V_T WNLLS in each ROI as independent variable and the mean of H-BFM A in each ROI as dependent variable were calculated for each subject. Pearson R^2 values were reported as the correlation measure.

To evaluate the H-BFM C results, the effect that the change of the methods chosen to define the grids has on the estimates was quantified with Eq. 5.4, where $V_{T,cluster}^{i,j}$ is the value of the H-BFM C estimate in the j^{th} voxel for the i^{th} subject and $V_{T,atlas}^{i,j}$ the value of the H-BFM A estimate in the j^{th} voxel for the i^{th} subject.

Another criterion to evaluate the performance of H-BFM A and H-BFM C was the coefficient of variation of the parameters to assess their precision.

Chapter 6

Results

6.1 H-MAP results

ROI analysis

In Figure 6.1 the scatterplot of V_T values obtained at the ROI level with compartmental analysis (x axis) and LEGA at ROI level (y axis) is presented. All the 700 ROIs considered for the 10 studies (five test, five retest, subscribed 'a' and 'b' respectively) were included. The ventricles and some small structures giving rise to noisy data were excluded (subcallosal area, nucleus accumbens, substantia nigra). There was excellent agreement and strong correlation among the 1T and LEGA estimates at ROI level ($R^2 = 0.96$), as already found previously ([85]) and the regression line was nearly a bisector even if it seems to detect some difference at high V_T values.

Voxel analysis - priors from atlas

Figure 6.2 shows the parametric maps of V_T obtained with H-MAP A for a representative subject (subject 3_a), on the three planes (coronal, top left; sagittal, top right; transverse, bottom image). The percentage of voxels out of the range defined in Chapter 5 was less than 0.4% for this subject: $< 0.21\%$ of voxels esti-

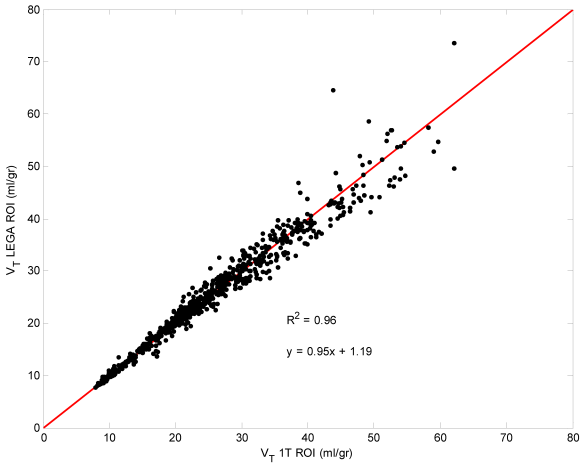

Figure 6.1: Scatterplot of ROI analysis V_T values estimated using WNLLS (x axis) and LEGA (y axis), obtained for all 700 ROIs considered for the 10 studies (five test, five retest). The red line is the identity line. Pearson's correlation coefficient R^2 is reported and the value of slope and intercept of the fitted regression line are presented.

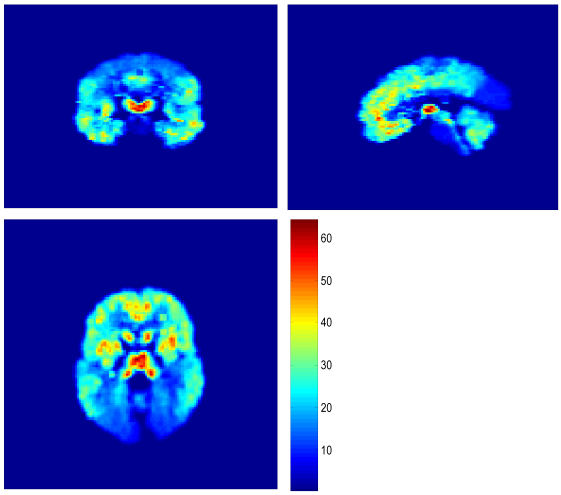

Figure 6.2: Parametric map of V_T obtained with H-MAP A for subject 3_a, shown in the three planes: coronal (top left), sagittal (top right), and transverse (bottom image). A Gaussian filter (FWHM 1.18 mm) was used to smooth the images before visualization. Note the high signal in the thalamus (top left and bottom image) and the intermediate signal of the frontal cortex (top right and bottom image).

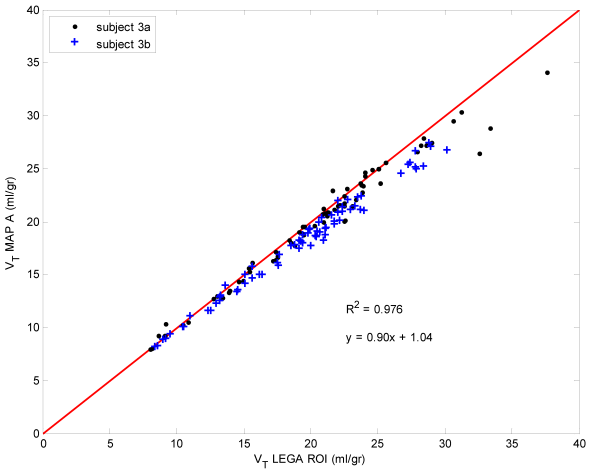

Figure 6.3: Scatterplot of V_T values estimated using LEGA on ROI data (x axis) versus the average of all voxels in the ROIs, after correction for non physiological estimates of V_T values estimated using H-MAP A (y axis) for subject 3. Black dots (o) correspond to test data (subject 3_a) and blue crosses (+) correspond to retest data (subject 3_b). The red line is the identity line. Pearson's correlation coefficient R^2 are reported for each test and the value of slope and intercept of the fitted regression line are presented.

mates were negative, and $< 0.18\%$ of voxels had V_T values above 100. In general for all the subjects the percentage out of the range was always less than 1.4% for $V_T < 0$ and less than 1.2% for $V_T > 100$.

The regional distribution of V_T was consistent with known opioid receptor distribution ([49]). More specifically, it can be seen in Figure 6.2 that the thalamus had the highest signal (top left and bottom images), followed by frontal cortex (top right and bottom images). The cerebellum (not present in the images) and the occipital cortex had the lowest signal.

In Figure 6.3 the scatterplot of V_T values estimated using LEGA at the ROI level (x axis) versus the average values of V_T calculated from the H-MAP A parametric map for each ROI (y axis) is presented for a representative subject (3_a and 3_b). There was good agreement and strong correlation among the estimates (for this subject global $R^2 > 0.97$) and the regression line was nearly a bisector.

In Table 6.1 the values of the Pearson's value and the estimated slope of the fitted regression line are reported for each subject (test and retest). On average,

	correlation coefficient R^2	*regression line (slope)*
sub 1_a	0.95	0.81
sub 1_b	0.94	0.76
sub 2_a	0.96	0.83
sub 2_b	0.96	0.81
sub 3_a	0.98	0.90
sub 3_b	0.98	0.89
sub 4_a	0.99	0.85
sub 4_b	0.97	0.77
sub 5_a	0.81	0.65
sub 5_b	0.94	0.85
mean	**0.94**	**0.81**
SD %	**5%**	**7%**

Table 6.1: Summary statistics (Pearson's value R^2 and slope of the fitted regression line) for the 10 studies (five subjects, one test and one retest data set each), subscribed 'a' and 'b' respectively) for LEGA ROI versus H-MAP A V_T (average of all voxels in the ROIs).

ROI	V_T *ROI LEGA [ml/g]*	V_T *ROI WNLLS 1T [ml/g]*	V_T *H-MAP A [ml/g]*
Hippocampus	17.7 ± 3.7	17.0 ± 3.5	17.1 ± 3.0
Cerebellum	15.2 ± 2.4	16.0 ± 3.1	15.1 ± 2.5
Brainstem	11.2 ± 2.3	11.2 ± 2.4	12.4 ± 2.3
Inferior frontal gyrus	28.5 ± 5.1	28.8 ± 6.5	26.8 ± 4.6
Thalamus	35.6 ± 7.2	35.7 ± 8.9	32.8 ± 6.0
Lingual gyrus	11.3 ± 7.2	11.4 ± 2.4	11.1 ± 1.7
Putamen	41.6 ± 9.2	42.3 ± 10.5	38.6 ± 7.7

Table 6.2: Inter subject regional values of V_T obtained from the parametric maps of H-MAP A (average of all voxels in the ROIs) are compared with the values of V_T obtained from ROI analysis (LEGA and WNLLS applied to the 1T compartmental model). The values are reported as mean ± SD.

there was very strong correlation among the methods ($R^2 = 0.94$), and just for one subject (5_a) R^2 was < 0.9. In Table 6.2 the values of V_T obtained with H-MAP A are compared with the V_T values estimated by ROI analysis. The H-MAP A method provided good results, similar to the ROI methods, even if there was a small underestimation of less than 3% of H-MAP A compared with the ROI methods. The average estimate precision, expressed as between subject SDs, improved, being on average 4.0 ml/g against 4.5 ml/g for ROI LEGA and 5.3 ml/g for ROI WNLLS.

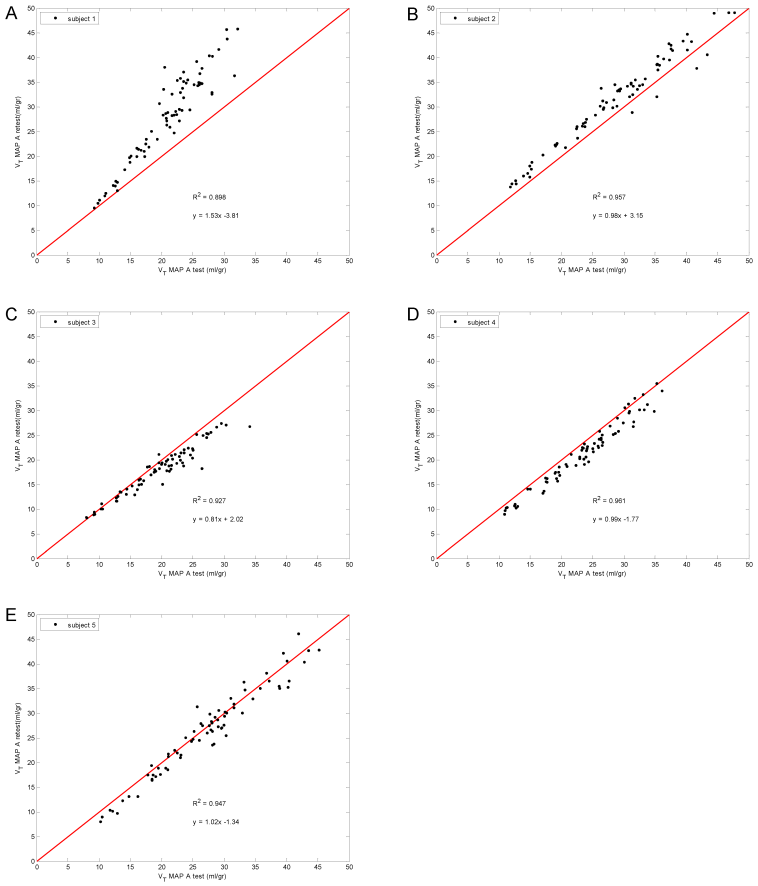

Figure 6.4: (A - E) Scatterplot of test and retest V_T values (x axis and y axis, respectively) estimated using H-MAP A for each subject (1-5). The values are calculated as the average of all voxels in the ROIs, after elimination of non-physiological estimates. The red line is the identity line. In each scatterplot the value of slope and intercept of the fitted regression line and Pearson's R^2 value are reported.

To assess the test-retest estimates for each subject the results obtained with H-MAP A were compared, where the values were the averages of all voxels in the ROIs after elimination of non physiological estimates.

In Figure 6.4 (A - E) the five scatterplots of V_T values obtained with H-MAP A for every subject, test (x axis) versus retest (y axis), are presented. In each subplot the estimated equation of the regression line and Pearson's R^2 are reported. These values, completed with their average between subjects, are also summarized in Table 6.3.

There was good test-retest reliability for all subjects but the first, who had the

	correlation coefficient R^2	*regression line (slope)*
sub 1	0.90	1.53
sub 2	0.96	0.98
sub 3	0.93	0.81
sub 4	0.96	0.99
sub 5	0.95	1.02
mean	**0.94**	**1.07**
SD %	**3%**	**27%**

Table 6.3: Summary statistics (Pearson's value R^2 and slope of the fitted regression line) for the estimates obtained with H-MAP A (average of all voxels in the ROIs) in test versus retest data for the five subjects.

	H-MAP A	*H-MAP C*
sub 1_a sub 1_b	0.51	0.56
sub 2_a sub 2_b	0.93	0.94
sub 3_a sub 3_b	0.91	0.92
sub 4_a sub 4_b	0.93	0.92
sub 5_a sub 5_b	0.97	0.96
mean	**0.85**	**0.86**
SD %	**22%**	**20%**

Table 6.4: correlation coefficients (ICCs) are presented for V_T values obtained with H-MAP A and H-MAP C for all the subjects in the seven ROIs described in the text.

smallest Pearson's value ($R^2 < 0.9$), whereas for all other subjects $R^2 > 0.92$ (average $R^2 > 0.93$), and the regression line was similar to the bisector. Subject 1 also had the slope furthest from unity, and the largest intercept, among the subjects.

For H-MAP A, the average ICC value among the subjects for each of the seven ROIs was 0.85, and it was lowest (0.51) for the first subject, as expected (Table 4). ICCs between 0.82 and 0.96 have been rated as good or excellent ([86]).

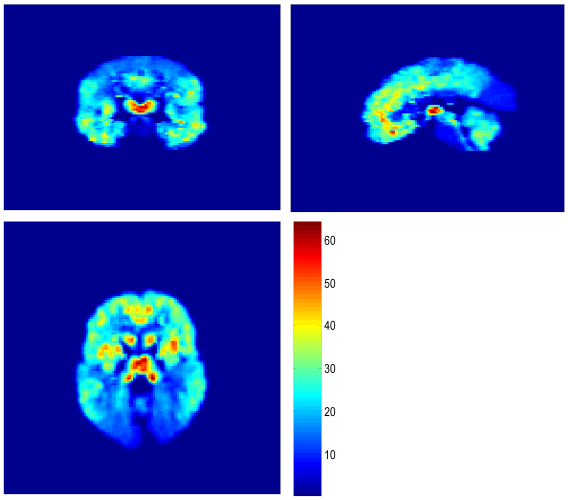

Figure 6.5: Parametric map of $_T$ obtained with H-MAP C method for subject 3_a (i.e. the same as in Figure 6.5). The priors have been extracted via functional clustering; for this particular scan the data were divided into seven clusters. A Gaussian filter (FWHM 1.18 mm) was used to smooth the images before visualization.

Voxel analysis - priors from functional cluster

In Figure 6.5 the parametric map of V_T obtained with H-MAP C for subject 3_a (i.e. the same as in Figure 6.5) is presented. In this case PET data were divided in seven different clusters. The final map is shown in the three planes (coronal, top left; sagittal, top right; transverse, bottom image).

H-MAP C resulted in 0.8% of voxels having negative V_T values and 0.75% values of $V_T > 100$. Visual comparison of Figure 6.2 and Figure 6.5 indicates that the way in which the priors were extracted did not affect the images qualitatively. The average percentage difference (Eq. 5.4) among all 83 ROIs of each subject varied between a minimum of -1% (subject 4_b) and a maximum of 2% (subject 1_a) (data not presented).

In Table 6.5, a comparison between the average estimates of V_T obtained with H-MAP A and H-MAP C is presented. The percentage difference in the estimates (average between subjects) for the ROIs examined varied between -1% and 1.7%, being more prominent in small and noisy ROIs, but on average there was no

ROI	V_T *H-MAP A [ml/g]*	V_T *H-MAP C [ml/g]*	*% difference*
Hippocampus	17.1 ± 3.0	16.9 ± 3.1	-1.0%
Cerebellum	15.1 ± 2.5	15.3 ± 2.6	1.2%
Brainstem	12.4 ± 2.3	12.6 ± 2.3	1.7%
Inferior frontal gyrus	27.2 ± 4.8	28.8 ± 6.5	1.6%
Thalamus	32.8 ± 6.0	33.2 ± 5.8	1.1%
Lingual gyrus	11.1 ± 1.7	11.2 ± 1.7	0.4%
Putamen	38.6 ± 7.7	38.8 ± 7.8	0.3%

Table 6.5: Regional values of V_T (mean of all voxel in the ROIs) and their average percentage differences obtained from H-MAP C parametric maps compared with values of V_T obtained with H-MAP A. The values are reported as inter-subjects mean ± SD.

difference among the two methods. The average estimate precision did not vary either.

ICCs for H-MAP C estimates were also calculated as a measure of reliability. The average ICC was excellent at 0.86, and it was again lowest for the first subject (0.56) as in Table 6.4.

6.1.1 Discussion

The method was tested on a 1T model, but it can be applied to any linear or linearized PET model. The priors for the Bayesian estimator are generated automatically from the data, and as a consequence are user-independent, overcoming the limitations of such methods as spectral analysis. Unlike methods like GLLS or GTS, this method does not require any iteration, and the bias introduced by the linearization of the model is resolved by the Bayesian estimation, so the critical choice of a termination criterion is avoided.

In comparison with the Bayesian method proposed in [7] also based on a Maximum a Posteriori estimator, this method differs in several fundamental aspects such as here a linear MAP estimator is used instead of a more computational expensive nonlinear estimator, the unknown scale factor of the variance matrix of the measurement error is derived on the basis of the reproducible method de-

scribed in [39] and in [40] and it does not require the use of additional images besides the data of the subject under analysis to define the *a priori* information. Differently from the Bayesian approach proposed in [7], H-MAP assumes a population composed by voxels, and relies on the hypothesis that the parameter estimates derived at ROI level (or by clustering) are representative of the expected model parameter values of the voxels composing the ROI itself (or cluster). The standard deviation of the parameter estimation error, derived from the inverse of Fisher's matrix, represents the between-voxels (i.e. between-subjects) possible variability.
The method is robust, as it allows a reliable estimation of model parameters in all but a few brain voxels. It is based on a linear optimization process, so it is not time consuming and suitable to analyze large amounts of data, as for example in voxel by voxel analyses.

The performance of the novel method for quantifying [^{11}C]DPN data was assessed. The H-MAP A and H-MAP C results had strong agreement with those obtained by using both graphical analysis and compartmental model solved by WNNLS, applied at the ROI level, and the identified regional distribution of opioid receptors was consistent with those found in previous studies ([49]). The reliability among test-retest estimates was also very good for all subjects but one.
The high variability in test-retest results for subject 1 is to be attributed to movement artifacts (see Figure 1 in [45]). The movement was substantial and it is likely that it had not been completely eliminated during the movement correction step, affecting consequently the test - retest estimates.

In literature, [^{11}C]DPN kinetics have mainly been described with a 2T model ([49], [43]), but it was difficult to obtain reliable estimates of k_3/k_4 values from a single [^{11}C]DPN tracer study.

Therefore to understand whether this difficulty was due to over-parameterization, both 1T and 2T models were applied to [^{11}C]DPN dataset and compared at the ROI and voxel level, solving them with WNLLS.

The performance of the models in fitting ROI TACs was assessed using the Akaike Information Criterion (AIC); the precision of the estimates expressed as their between-subject standard deviation and the percentage of model failures at the voxel level. For further comparison also the values estimated via LEGA applied to ROIs were used, as they are supposed to be unbiased.

Both at the ROI and voxel level, the 1T model best described the available [^{11}C]DPN dataset.

6.2 H-BFM results

[^{11}C]FLB457

In Figure 6.6 the parametric maps of V_T estimated with H-BFM A (Figure 6.6A) and H-BFM C (Figure 6.6B) are presented for a representative subject (subject 3). For this subject the percentage of a out-physiological-range voxels (as described in Section 5.2) was less than 2% for H-BFM A and less than 3% for H-BFM C. In general for all the subjects for both methods the percentage out of range was always less than 2% for $V_T < 0$ and less than 6% for $V_T > 25$ (taking in account that around 1.5% of the voxels higher than the cutoff belongs to the striatum which is not considered due to the too short scanning protocol).

Instead, WNLLS V_T estimates out of range were in general $> 30\%$ (for this subject, more than 36% of voxels had $V_T > 25$) being the non linear estimator more sensitive to noise in the data.

The regional distribution of V_T was consistent with known dopamine receptor distribution ([54]). More specifically, it can be seen in Figure 6.6A and Figure 6.6B that the striatum had the highest radioactivity concentration. Beside

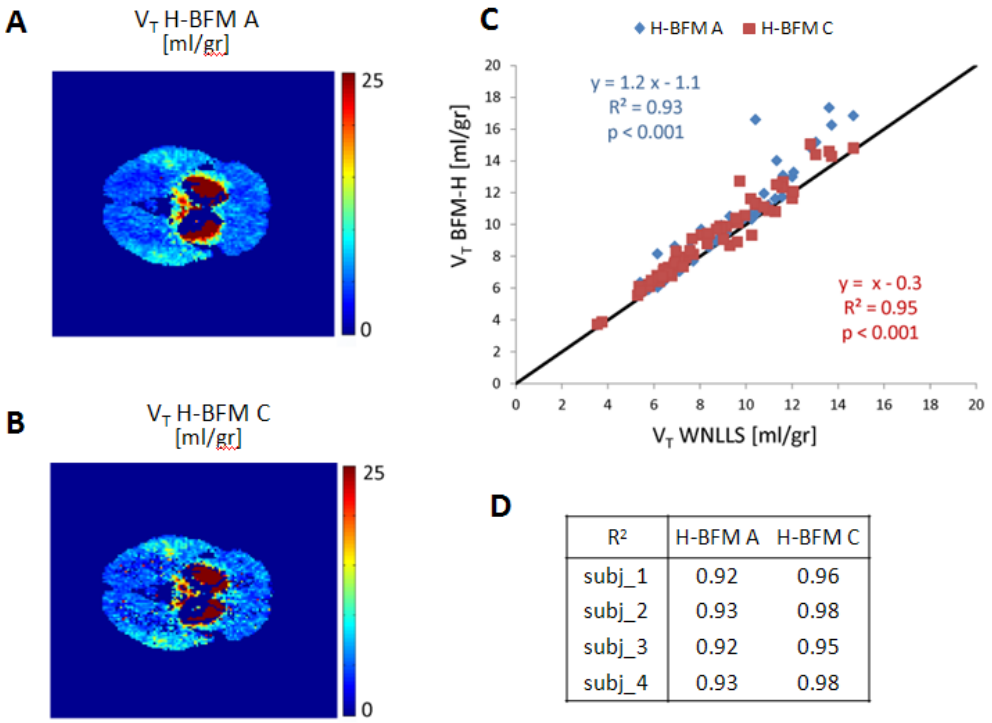

R²	H-BFM A	H-BFM C
subj_1	0.92	0.96
subj_2	0.93	0.98
subj_3	0.92	0.95
subj_4	0.93	0.98

Figure 6.6: (A-B) Parametric maps of [^{11}C]FLB457 V_T estimated with H-BFM A (A) and H-BFM C (B) of a representative subject (subject 3). Note the high signal in the striatum and in extrastriatal regions as thalamus, temporal and frontal cortices. (C) Scatterplot of the average values of V_T estimated using WNLLS at voxel level (x axis) versus the average values of V_T calculated from the H-BFM parametric map for each ROI (y axis) of the same subject (H-BFM A, blue diamonds, and H-BFM C, red squares). The black line is the identity line. Pearson's correlation coefficients R^2 are reported for each test and the value of slope and intercept of the fitted regression line are presented. (D) Pearson's values for each subject (H-BFM A and H-BFM C)

.

the striatum, not considered due to the too short scanning protocol, conspicuous radioactivity was found in extrastriatal regions as thalamus, temporal and frontal cortices. The cerebellum (not present in the images) had the lowest signal.

In Figure 6.6C the scatterplot of the average values of V_T estimated using WNLLS at voxel level (x axis) versus the average values of V_T calculated from the H-BFM parametric map for each ROI (y axis) is presented for the same subject (H-BFM A, blue diamonds, and H-BFM C, red squares). There was good agreement and strong correlation among the estimates (for this subject $R^2 > 0.93$ for H-BFM A and $R^2 > 0.98$) and the regression line was nearly a bisector. In Figure 6.6D the values of the Pearson's value are reported for each subject (H-BFM A and H-BFM C). On average, there was very strong correlation among the methods (in average $R^2 > 0.92$ and $R^2 > 0.96$ respectively).

In Figure 6.7A the values of V_T obtained with H-BFM A and H-BFM C are compared with the V_T values estimated by voxel WNLLS analysis. In average there was no difference in the estimates when the grids are defined based on anatomical or functional segmentation.

The H-BFM methods provided good results, with no difference in the estimates of H-BFM A and H-BFM C, which were similar to those obtained with the non linear estimator, even if there was a small overestimation of less than 10% of H-BFM compared with the WNLLS methods. As said, more than 30% of WNLLS estimates are eliminated, while only $< 8\%$ of H-BFM results are out of range (also taking in account striatum voxels), so H-BFM estimates were compared only in the voxels with reliable WNLLS values of V_T. In this case, as expected, there is still no difference in the results of H-BFM C compared to H-BFM A, and the difference previously reported between H-BFM results compared to WNLLS estimates lowers to less than 1%.

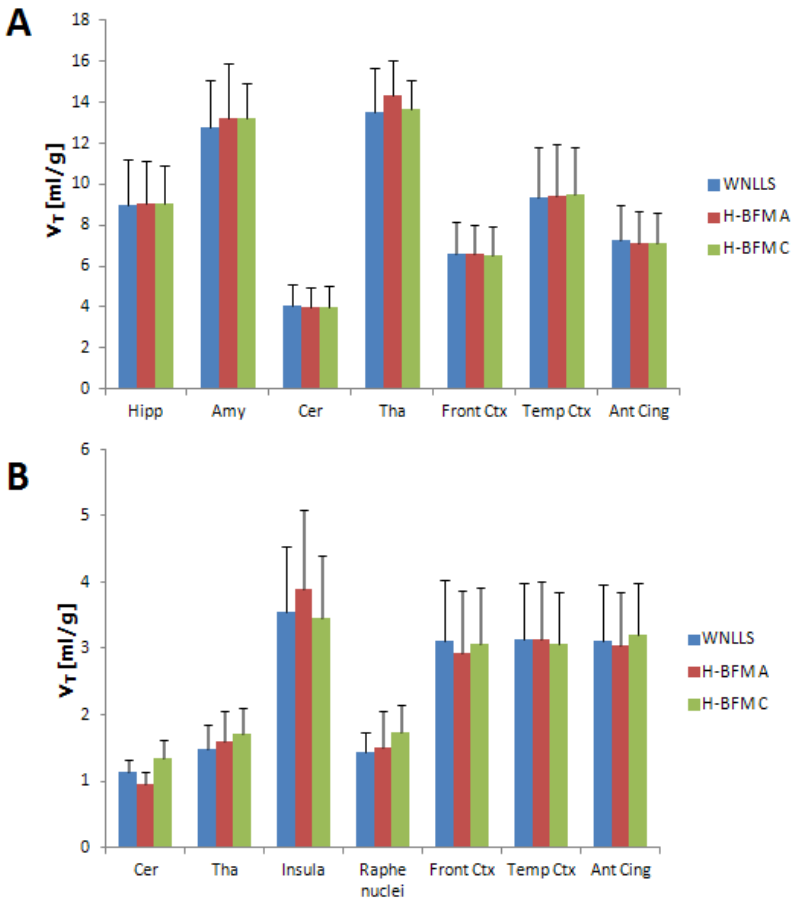

Figure 6.7: Inter subject regional values of V_T obtained with H-BFM A and H-BFM C are compared with the V_T values estimated by voxel WNLLS analysis for [^{11}C]FLB457 data (A) and for [^{11}C]WAY100635 data (B). The average estimate precision is expressed as between subject SDs. Hipp = hippocampus, Amy = amygdala, Cer = cerebellum, Tha = thalamus, Front Ctx = frontal cortex, Temp Ctx = temporal cortex, Ant Cing = anterior cingulate.

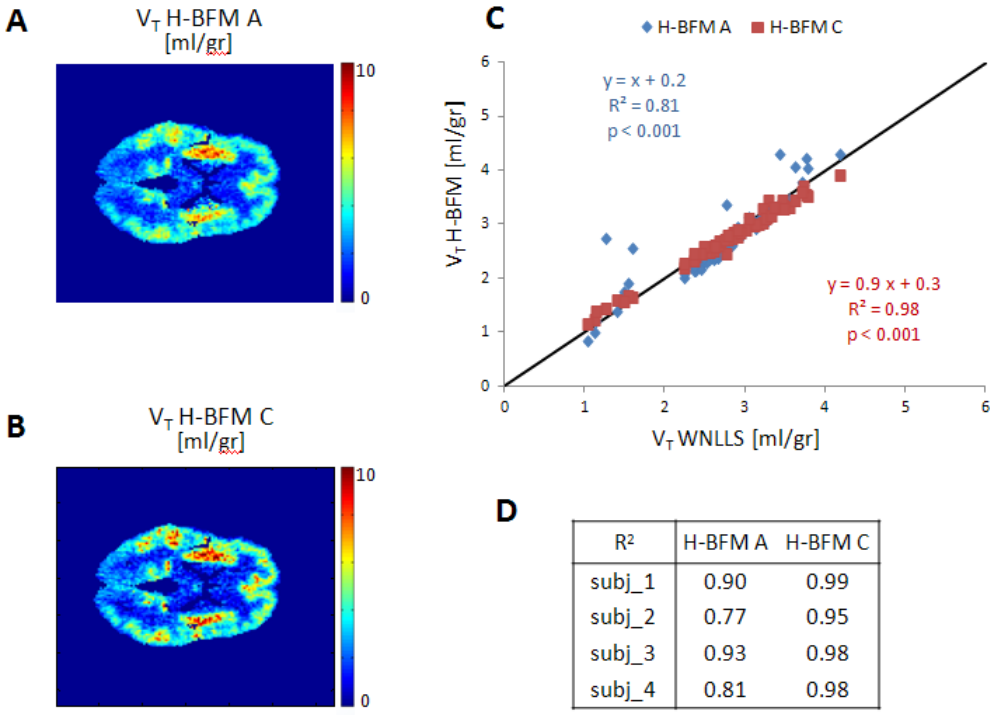

R^2	H-BFM A	H-BFM C
subj_1	0.90	0.99
subj_2	0.77	0.95
subj_3	0.93	0.98
subj_4	0.81	0.98

Figure 6.8: (A-B). Parametric maps of [^{11}C]WAY100635 V_T estimated with H-BFM A (A) and H-BFM C (B) of a representative subject (subject 4). Note the high signal in the insula followed by frontal and temporal cortices and anterior cingulate. (C) Scatterplot of the average values of V_T estimated using WNLLS at voxel level (x axis) versus the average values of V_T calculated from the H-BFM parametric map for each ROI (y axis) of the same subject (H-BFM A, blue diamonds, and H-BFM C, red squares). The black line is the identity line. Pearson's correlation coefficients R^2 are reported for each test and the value of slope and intercept of the fitted regression line are presented. (D) Pearson's values for each subject (H-BFM A and H-BFM C).

[^{11}C]WAY100635

In Figure 6.8 the parametric maps of V_T estimated with H-BFM A (Fig 6.8A) and H-BFM C (Fig 6.8B) are presented for a representative subject (subject 4). For this subject the percentage of voxels of out physiological range was less than 1% for both H-BFM A and H-BFM C.

In general for both methods the percentage out of range was always less than 2% for $V_T < 0$ and less than 1% for $V_T > 25$. Instead, WNLLS V_T estimates out of range were in general $> 30\%$ (for this subject, more than 32% of voxels had

$V_T > 25$).

The regional distribution of V_T was consistent with known serotonin receptor distribution ([87]). More specifically, the insula had the highest signal, followed by frontal and temporal cortices and anterior cingulate, as it can be seen in Figure 6.8A and Figure 6.8B. The cerebellum (not present in the images) and the thalamus had the lowest signal.

In Figure 6.8C the scatterplot of the average values of V_T estimated using WNLLS at voxel level (x axis) versus the average values of V_T calculated from the H-BFM parametric map for each ROI (y axis) is presented for the same subject (H-BFM A, blue diamonds, and H-BFM C, red squares).

There was good agreement and strong correlation among the estimates (for this subject $R^2 > 0.81$ for H-BFM A and $R^2 > 0.98$ for H-BFM C) and the regression line was nearly a bisector. In Figure 6.8D the values of the Pearson's value are reported for each subject (H-BFM A and H-BFM C). On average, there was very strong correlation among the methods ($R^2 > 0.85$ and $R^2 > 0.97$ respectively).

In Figure 6.7B the values of V_T obtained with H-BFM A and H-BFM C are compared with the V_T values estimated by voxel WNLLS analysis. In average there was a small overestimation of 8% of H-BFM C compared to H-BFM A, especially in low binding regions like cerebellum and raphe nucleus. Not considering the cerebellum, the difference lowered to $< 3\%$. This can be due to the heterogeneity of cerebellum ([88]) and the relatively high concentration of 5-HT_{1A} receptors in the cerebellar vermis ([89]), that is not taken in account with the anatomical segmentation, but that is partially overcome with a functional segmentation.

The H-BFM methods provided good results, similar to those obtained with the non linear estimator. The average estimate precision, expressed as between subject SDs, was similar between H-BFM A and H-BFM C estimates and improved

especially in high binding regions using H-BFM C, being on average 0.71 ml/g against 0.63 ml/g for H-BFM A.

6.2.1 Discussion

The performance of the novel method for quantifying [^{11}C]FLB457 and [^{11}C]WAY 100635 data was assessed. The H-BFM A and H-BFM C results had strong agreement with those obtained by using compartmental model solved by WNNLS, applied at the voxel level, and the identified regional distribution of receptors was consistent with those found in previous studies ([54], [87]).
In average, the difference in the estimates between WNLLS and H-BFM was less than 1% (once considering H-BFM estimates only in the voxels with reliable WNLLS values of V_T).

H-BFM is robust and faster than WNLLS (at least three times faster) and its application on both [^{11}C]FLB457 457 and [^{11}C]WAY100635 allows accurate quantification of V_T and good quality parametric maps.
H-BFM allows user-independent PET quantification, where the grids are defined automatically from the data, subject and ROI specific. To the author's knowledge there are only two previous works which developed the BFM for multi-compartmental models ([3] and [4]), but in that approach the grids were global and user-defined.
In particular, in [3] the grids were 2-dimensional, each dimension constituted by 100 logarithmically spaced element. The ranges were defined, fixed for all voxels regardless of the anatomical region, from values presented in literature.
Grids defined in such a way imply the linear estimation process to be repeated 10'000 times for each voxel, resulting in a very demanding computational analysis.
In [3] and in [4], BFMs were also applied to a 3K model, with 1-dimensional grid

with 100 basis function. Having only one convolution to be solved, the grid can be dense with no particular effect on the required computational time. Nevertheless the grids were defined logarithmically and fixed for all cerebral voxels and all subjects.

6.3 Results based on functional clustering

K-means on whole kinetics: [^{11}C]DPN and [^{11}C]FLB457

For both datasets, the partitioning method of choice was the k-means, applied to the whole tracer kinetics, as described in Chapter 5.

The optimal number of clusters, K, was automatically selected as the greatest possible number which keeps the centroids statistically different between each other. The statistical difference was tested with the Wilcoxon's test, as implemented in Matlab.

For [^{11}C]DPN data, for all subjects but one, six or seven clusters were enough to describe all significantly different kinetics within the brain. For subject 1_a and 1_b, the optimal number of clusters was eight and nine for the test and retest scans, respectively.

In this case the way to derive the priors does not affect the final results: the images did not differ qualitatively, and the average percentage difference of estimates was less than 1% (Table 6.5).

The different segmentations had no impact on [^{11}C]FLB457 final estimates, as no differences in the results were detected, as can be seen in Figure 6.7. Note that for both tracers, in the final masks, even if the clusters were created grouping the TACs on the base only of their kinetics, it was easy to verify also good agreement with anatomical segmentation, as can be seen in Figure (6.9).

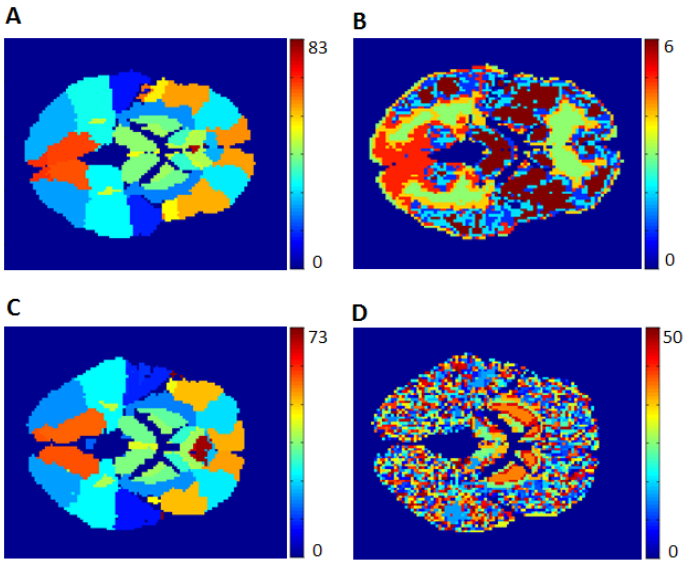

Figure 6.9: Example of a BrainAtlas (A) and of a functional mask (B) (6 clusters) for subject 3_a of [^{11}C]DPN dataset and of a BrainAtlas (C) and of a functional mask (D) (50 clusters) for subject 1 of [^{11}C]FLB457 dataset: each color corresponds to a cluster, and it easy to see that the clusters are distributed also in accord to anatomical ROIs (see for example thalamus and striatum).

New parametric clustering method: application on [^{11}C]WAY100635, [^{11}C]SCH442416 and [^{11}C]MDL100907

The clustering algorithm presented above (k-means applied on the whole TACs) did not perform well applied on [^{11}C]WAY100635 , [^{11}C]SCH442416 and [^{11}C]MDL 100907 data and consequently a new clustering algorithm was developed, based on the parametrization of the tracer's kinetics, as described in Chapter 5, and applied on these three datasets.

The optimal number of clusters, K, was again automatically selected as the greatest possible number which keeps the centroids statistically different between each other (tested with the Wilcoxon's test).

Also for these tracers, in the final masks it was easy to verify also good agreement with anatomical segmentation (in Figure 6.10 is reported an example for [^{11}C]WAY100635 data).

For [^{11}C]WAY100635 data, there was a small overestimation of $< 3\%$ in the final

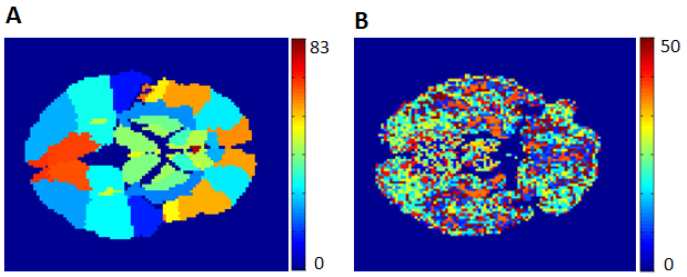

Figure 6.10: Example of a BrainAtlas (A) and of a functional mask (B) (50 clusters) for subject 2 of [^{11}C]WAY100635 dataset: each color corresponds to a cluster, and it easy to see that the clusters are distributed also in accord to anatomical ROIs.

estimates comparing the two different segmentations, not considering the cerebellum. H-BFM C overestimated of about 8% compared to H-BFM A, but more than 5% was due to heterogeneity of cerebellum ([88]) and the relatively high concentration of 5-HT$_{1A}$ receptors in the cerebellar vermis ([89]).

In fact, this heterogeneity can not be taken in account with the anatomical segmentation, but can be partially overcome with a functional segmentation. This shows how functional clustering can allow generating informative grids which will take in account the voxel-wise local variation of the tracer distribution, which could be useful especially if the method was to be applied on a tracer with spotty distribution.

Chapter 7

Additional work: development of novel compartmental models for quantification of PET tracer kinetics

As described previously, both novel methods H-MAP and H-BFM are model-driven methods, based on compartmental models. When the optimal model to be used to describe the data was not already presented in literature it has been necessary to develop the compartmental model to quantify the tracer under study using model- and data-driven methods. In particular, new compartmental models for [^{11}C]SCH442416 and for [^{11}C]MDL100907 data were developed. [^{11}C]SCH442416 data have never been quantified with compartmental models in humans before and for [^{11}C]MDL100907 the model presented in literature was not appropriate for the fit of the available data.

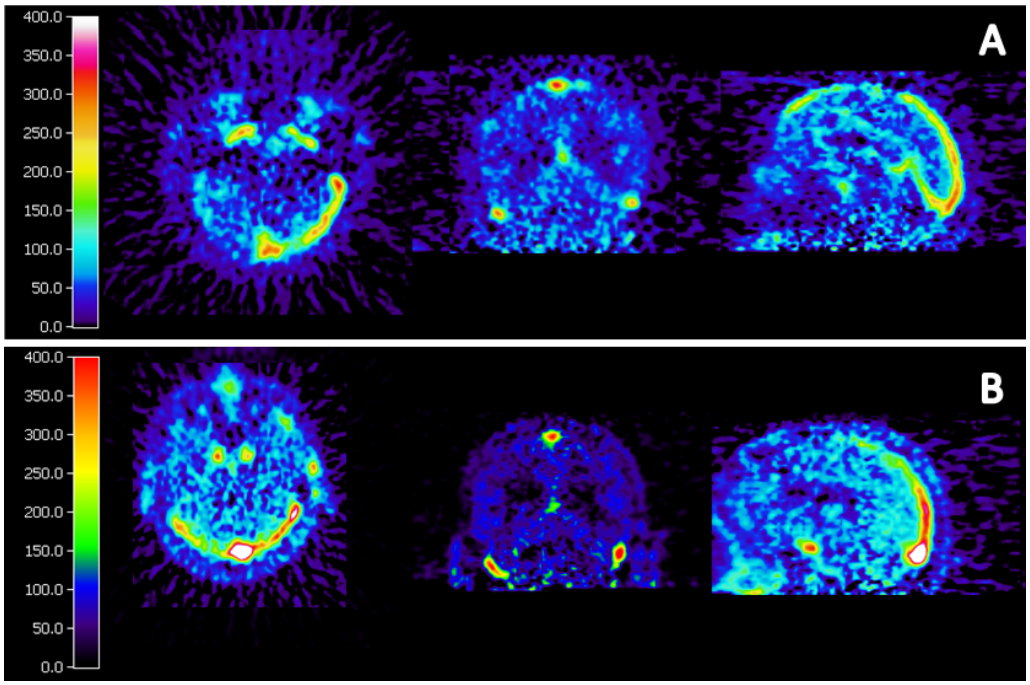

Figure 7.1: Dynamic PET images summed over the first 2 min, shown in the three plane (transverse, coronal, sagittal), of subject 1 (A) and subject 5 (B). For both subjects the vascular component is clearly detectable.

7.1 Modeling [^{11}C]SCH442416 dataset

As described in Section 4.1.4, quantitative assessment of A_{2A} receptor expression from [^{11}C]SCH442416 PET images in human brain have been made by using spectral analysis ([67] and [68]) revealing the presence of both reversible and irreversible components.

The aim of this study is to develop the compartmental model to quantify [^{11}]SCH 442416 kinetics at voxel level in healthy control subjects, based on the results presented in [69], using the dataset described in Section 4.1.4.

In order to develop the model, a preliminary analysis on the tissue and plasma data was carried out. [^{11}C]SCH442416 showed an important vascular component in all subjects, especially for two subjects. As it can be seen from the dynamic PET summed over the first 2 min (in Figure 7.1), for both subjects (subject 1,

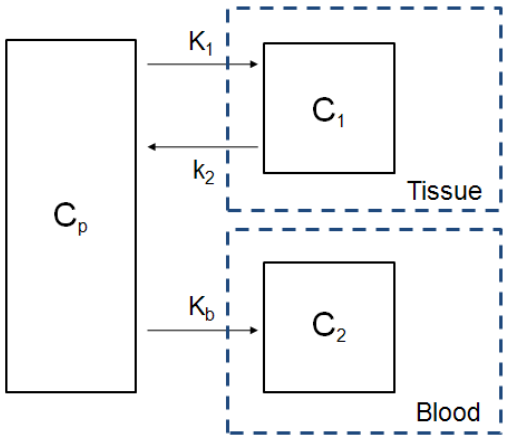

Figure 7.2: Two tissue-three rate constants in parallel (3K-parallel) compartmental model. K_1 (ml/g/min) and k_2 (min^{-1}) represent first order rate constants for transport of ligand from plasma to tissue (C_1) and vice versa. K_b (ml/g/min) is the rate constant from plasma to the trapping vascular component (C_2).

A, and subject 5, B) a notable vascular component was clearly detectable. This vascular component made it very difficult to generate the atlas and to properly estimate the model parameters. Moreover, a clear asymmetry in the vascular contribute was recognized.

A preliminary assessment on the model structure was carried out.

7.1.1 Model structure

Two tissue-three rate constants compartmental model in parallel (3K-parallel)

In Figure 7.2 the two tissue-three rate constants in parallel (3K-parallel) compartmental model proposed by [69] is presented. The tissue (C_1) is represented by one compartment for the non displaceable component (nd) plus a specifically

bound fraction (sp), according to:

$$\begin{aligned} \dot{C}_1(t) &= K_1 C_p(t) - k_2 C_2(t) & C_1(0) &= 0 \\ \dot{C}_2(t) &= K_b C_p(t) & C_2(0) &= 0 \end{aligned} \tag{7.1}$$

$$C_{VOI}(t) = (1 - V_b)\, C_1(t) + V_b\, (C_2(t) + C_b(t)) \tag{7.2}$$

where K_1 (ml/g/min) and k_2 (min^{-1}) represent first order rate constants for transport of ligand from plasma to tissue and vice versa. K_b (ml/g/min) is the rate constant from plasma to the trapping vascular component C_2.
The parameter of interest is the total volume of distribution (V_T, ml/g), which is calculated from the ratio of the two tissue parameters as in Eq. 2.19.
As already described in Chapter 2, the model was solved with basis functions obtaining the following equation:

$$C_{VOI}(t) = (1 - V_b)\, K_1 C_p(t) \otimes e^{-k_2 t} + V_b K_1 \int_0^t C_p(\tau) d\tau + V_b C_b(t) \tag{7.3}$$

The model was solved with H-BFM, as in Chapter 3, where the local grid for the parameter k_2 was defined for each region from the ROI estimates, solving the model above with WNLLS. The grid was still created based on a sampling of a Gaussian distribution, whose mean was the parameter k_2 estimated at ROI level and the standard deviation was calculated directly from the estimate precision. As there was only one convolution to be solved, the grid was 1-dimensional and the size was set equal to 100.

Three tissue-four rate constants compartmental model in parallel with two input functions (4K-2IF)

The initial model presented in [69] was not appropriate to describe the data of two subjects of the dataset (subject 1 and subject 5). An alternative model was

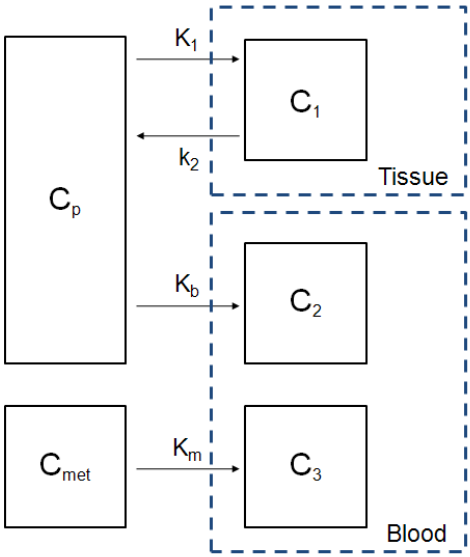

Figure 7.3: Three tissue-four rate constants in parallel compartmental model with two input functions (4K-2IF). K_1 (ml/g/min) and k_2 (min^{-1}) represent first order rate constants for transport of ligand from plasma to tissue (C_1) and vice versa. K_b (ml/g/min) is the rate constant from plasma to the trapping vascular component (C_2). K_m (ml/g/min) is the rate constant from metabolites to the trapping vascular component (C_3).

proposed (Figure 7.3). The three tissue-four rate constants model in parallel with two input functions (4K-2IF) includes the arterial plasma component (C_p), the concentration of metabolites over time (C_{met}), one tissue compartment (C_1, accounting for the non displaceable component plus the specific binding) and two trapping components (C_2 and C_3), according to:

$$\begin{aligned} \dot{C}_1(t) &= K_1 C_p(t) - k_2 C_1(t) & C_1(0) &= 0 \\ \dot{C}_2(t) &= K_b C_p(t) & C_2(0) &= 0 \\ \dot{C}_3(t) &= K_m C_{met}(t) & C_3(0) &= 0 \end{aligned} \tag{7.4}$$

$$C_{VOI}(t) = (1 - V_b)\, C_1(t) + V_b\, (C_2(t) + C_3(t) + C_b(t)) \tag{7.5}$$

where K_1 (ml/g/min) and k_2 (min^{-1}) represent first order rate constants for transport of ligand from plasma to tissue and vice versa. K_b (ml/g/min) is the rate constant from plasma to the trapping vascular component (C_2). K_m (ml/g/min) is the rate constant from metabolites to the trapping vascular component (C_3).

The parameter of interest is the total volume of distribution (V_T, ml/g), which is calculated from the ratio of the two tissue parameters as in Eq. 2.19.
As already described in Chapter 2, the model was solved with basis functions obtaining the following equation:

$$C_{VOI}(t) = (1 - V_b)\, K_1 C_p(t) \otimes e^{-k_2 t} + V_b K_b \int_0^t C_p(\tau) d\tau + \\ + V_b K_m \int_0^t C_{met}(\tau) d\tau + V_b C_b(t) \tag{7.6}$$

The model was solved with H-BFM, as in Chapter 3, where the local grid for the parameter k_2 was defined as above for model 3K-parallel.

The best model was chosen on the basis of *a priori* identifiability, *a posteriori* numerical identifiability, and Akaike criterion. Goodness of the fit, estimates included in the physiological interval and precision estimates were also evaluated.

7.1.2 4K-2IF model results

ROI analysis

At ROI level, for two subjects the optimal model to describe [^{11}C]SCH442416 kinetics was the 4K-2IF one, while for the remaining 4 subjects the optimal model was 3K-parallel. In particular, the presence of the second trapping component, linked to the concentration of metabolites over time, was fundamental to obtain a proper fit of the late part of the ROI curve for subject 1 and subject 5. In Figure 7.4 is reported an example of fit of 3K-parallel (dashed lines) and 4K-2IF model (dot dashed lines) to the tissue TAC of cerebellum (circles) for subject 1, where it can be seen as 3K-parallel model is insufficient to properly describe the data.
Instead 4K-2IF did not perform well applied to the other 4 subjects of the

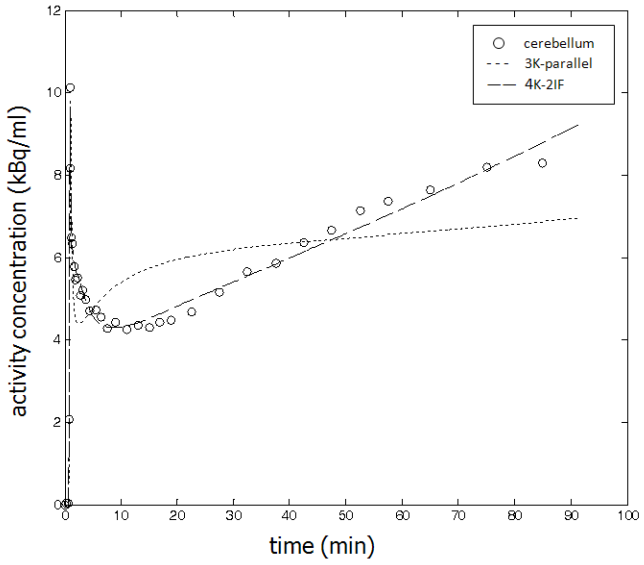

Figure 7.4: Example of fit of 3K-parallel (dashed lines) and 4K-2IF model (dot dashed lines) to the tissue TAC of cerebellum (circles) for subject 1.

datasets, as K_m always tended to 0, resulting in 3K-parallel to be the best model.

Voxel analysis

For subject 1 and 5, 4K-2IF model failed at voxel level, V_T was estimated negative (i.e. not physiological) for more than 25% of the voxels, although the parametric maps were quite uniform. In presence of higher level of noise (typical of the voxel-wise analysis), the second vascular component was difficult to detect, and it was often not estimated. Moreover, the model estimates suffered of the difficulties due to the heavy vascular component, as shown in Figure 7.1. The same difficulties will be found also for the simpler model. When a voxel was mainly vascular, k_2 tended to be very high, meaning that the tracer did not enter the tissue, and consequently the exchange between C_p and C_1 was too fast to be detected and the structure collapsed.

Various attempts to separate the tissue and vascular information were made. At

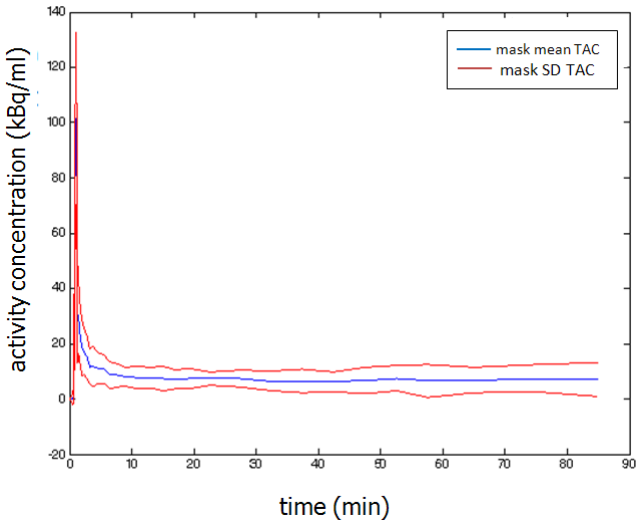

Figure 7.5: Mean TAC obtained averaging the mask voxels, whose TAC presented a peak value higher than 100 kBq/ml (blue line) and the corresponding standard deviation (red line).

first a simple masking was implemented, eliminating the voxels whose TAC presented a peak value higher than 100 kBq/ml (the maximum peak value for the ROI TACs was less than 30 kBq/ml). From a visual inspection, the mean curve obtained from the masked voxel was a clear example of the time course of the vascular component with a narrow standard deviation, as shown in Figure 7.5.
The voxels belonging to the mask were eliminated from the atlas and H-BFM was applied using the new atlas, obtaining grids "cleaned" from the vascular components.
The grid calculated from the ROI analysis was more compact (with an average reduction of the mean SD associated to the parameter k_2 of 5%), but the final estimates did not change quantitatively.

As second attempt, a hierarchical clustering was applied on the data: the standard partitioning k-means (i.e. on the whole kinetics, Section 4.2) was implemented iteratively on the images, up to three times. This approach did not ameliorate the results. In fact, in two steps it was possible to separate the vas-

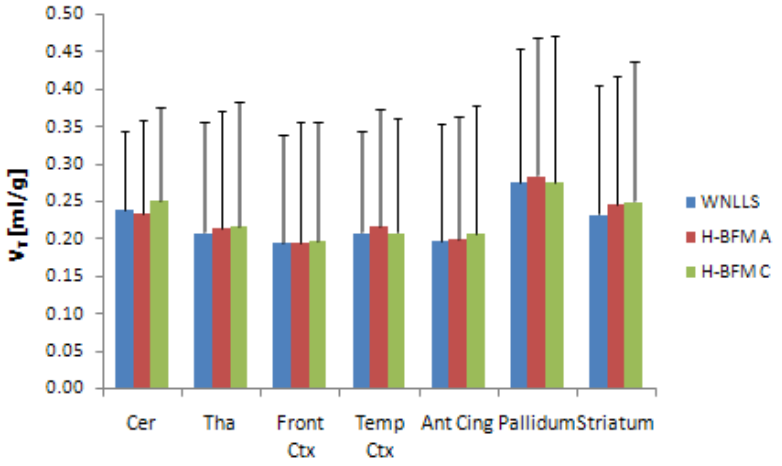

Figure 7.6: Inter subject regional values of V_T obtained with H-BFM A and H-BFM C are compared with the V_T values estimated by voxel WNLLS analysis for [^{11}C]SCH442416 data. The average estimate precision is expressed as between subject SDs.

cular information from the tissue, obtaining a mask similar to the one obtained with the previous attempt, but once extracted the tissue information, it was no possible to properly segment the image. The cluster analysis only managed to segment the white matter from the gray matter, with no use for an appropriate brain segmentation.

H-BFM was applied anyway using the clustered regions, and the same observations made for the results obtained with anatomical segmentation held: when a voxel contained mainly vascular information, k_2 was very high and the model collapsed.

7.1.3 3K-parallel model results

The model of choice to describe [^{11}C]SCH442416 data is 3K-parallel, as already found in [69].

The 3K-parallel model was applied to all subjects and solved with H-BFM as described above.

In Figure 7.6 the values of V_T obtained with H-BFM A and H-BFM C are com-

pared with the V_T values estimated by voxel WNLLS analysis. In average there is almost no difference in the estimates when the grids are defined based on anatomical or functional segmentation (difference% was less than 1%).
The H-BFM methods provided good results, with no difference in the estimates of H-BFM A and H-BFM C, which were similar to those obtained with the non linear estimator, with only a small overestimation of less than 3% of H-BFM compared with the WNLLS methods.

V_T estimates showed a large variability, considering for example the striatum, in which V_T ranged from a value of 0.09 ml/g (subject 1) up to 0.57 ml/g (subject 3). The lower V_T estimates were found for subject 1 and subject 5 (in striatum $V_T = 0.11$ ml/g), as expected, being the subjects with the higher vascular component. As already noted, the presence of a vascular contribute led to high estimates of K_b (for these subjects in average values higher than 150% compared to the other subjects) and especially of k_2 (values in average higher than 200% compared to the other subjects), resulting in very low estimates of V_T.
In Figure 7.7 the parametric maps of V_T estimated with H-BFM A (Fig. 7.7A) and H-BFM C (Fig.7.7B) are presented for a representative subject (subject 3). Less than 10% of voxels had $V_T < 0$ and less of 1% of voxel presented $V_T > V_{Tcutoff} = 1$.
The regional distribution of V_T reflected the known physiological distribution of adenosine receptor ([63], [68]).
In Figure 7.7C the scatterplot of the average values of V_T estimated using WNLLS at voxel level (x axis) versus the average values of V_T calculated from the H-BFM parametric map for each ROI (y axis) is presented for the same subject (H-BFM A, blue diamonds, and H-BFM C, red squares). There was good agreement and strong correlation among the estimates (for this subject $R^2 > 0.85$ for H-BFM A and $R^2 > 0.90$) and the regression line was nearly a bisector. In Figure 7.7D the values of the Pearson's value are reported for each subject (H-BFM A and

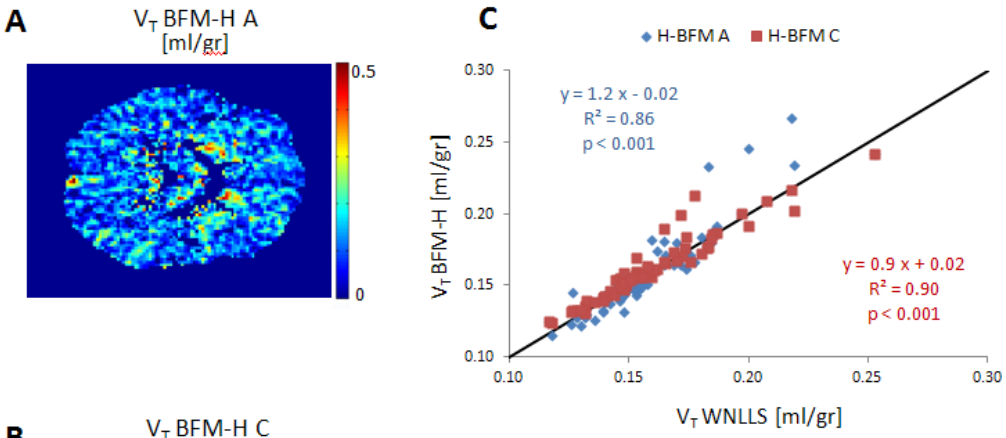

D

R²	atlas	cluster
2269	0.902	0.821
2318	0.727	0.935
2414	0.718	0.841
2457	0.858	0.902
2467	0.563	0.719
2480	0.957	0.893

Figure 7.7: (A-B) Parametric maps of [^{11}C]SCH442416 V_T estimated with H-BFM A (A) and H-BFM C (B) for a representative subject (subject 3). (C) Scatterplot of the average values of V_T estimated using WNLLS at voxel level (x axis) versus the average values of V_T calculated from the H-BFM parametric map for each ROI (y axis) of the same subject (H-BFM A, blue diamonds, and H-BFM C, red squares). The black line is the identity line. Pearson's correlation coefficients R^2 are reported for each test and the value of slope and intercept of the fitted regression line are presented. (D) Pearson's values for each subject (H-BFM A and H-BFM C)

.

H-BFM C). On average, there was very strong correlation among the methods (in average $R^2 > 0.78$ and $R^2 > 0.85$ respectively).

In general, H-BFM C showed a better correlation with WNLLS results compared to H-BFM A. This effect was expected because of the high heterogeneity due to the notable vascular component present in all subjects, which could not be taken in account with the anatomical segmentation, but was partially overcome with a functional segmentation.

The same attempt already made for 4K-2IF model to reduce the vascular contribute with functional hierarchical clustering was applied to subject 4. The cluster identifying the vascular component was eliminated from the anatomical atlas and H-BFM A was applied on the new atlas.

The ROI estimates did not change, but the correlation with WNLLS results improved ($R^2 > 0.9$), confirming the vascular correction to be a promising approach for [^{11}C]SCH442416 estimation at voxel level with H-BFM.

7.1.4 Discussion

4K-2IF model gave good results at ROI level for 2 subjects out of 6 (probably due to heterogeneity). The additional component was necessary for a proper fit of the tail of the region TACs, but for [^{11}C]SCH442416 data the best model to be applied on voxel level was a three compartmental one.

An analysis on tissue and input data for subject 1 and 5 was carried out. A possible explanation for the necessity of a different model to properly fit the data could be related to difference in metabolism. In fact from a comparison of $C_{met}(t)$ it resulted that the concentration of the metabolites increased in the late part of the PET exam, i.e. the value of the slope of the curve evaluated from 20 min to the end of the scan was positive, in contrast with the values for the other subjects which were negative.

The possibility that the two components detected with spectral analysis ([67], [68], [69]) could refer to a 3K model in series (as in Figure 2.2, Eq. 2.9, Eq. 2.10) was discussed. In this case the trapping component could be due to binding to receptors or production of metabolites in the tissue.
From physiological data, adenosine A_{2A} receptors are known to be abundant in basal ganglia, vasculature and platelets. Consequently V_T is expected to be high in striatum, pallidum and nucleus accumbens.
If k_3 is related to receptor binding, the macroparameter K is expected to be high in rich receptor density ROIs (same ROIs with high V_T).
If k_3 is related to production of metabolites in the tissue, V_T should be related to receptor density.

When applied to [^{11}C]SCH442416 data, the 3K model presented physiological estimates of V_b ($V_b \sim 0.05$) and V_T estimates well correlated with known receptor distribution but much higher than spectral analysis values (up to ten times higher). Also the exchange between the plasma and non displaceable compartment resulted higher than expected.
Moreover, in rich receptor density ROIs high V_T values were detected, but a low K was estimated, indicating that the trapping was not related to binding to receptors.
Instead, 3K-parallel model provided physiological values of V_b ($V_b \sim 0.05$) and the estimated V_T was well correlated with the known receptor density and comparable to spectral analysis results.

In 3K-parallel model, K_b represents the trapping to the vascular component and it is expected to be correlated to receptor density in vascular system. Previous studies showed that A_{2A} receptors are expressed in the vessels and platelets ([90], [91]), confirming the model interpretation, but it should be elaborated on how to justify this physiological interpretation.

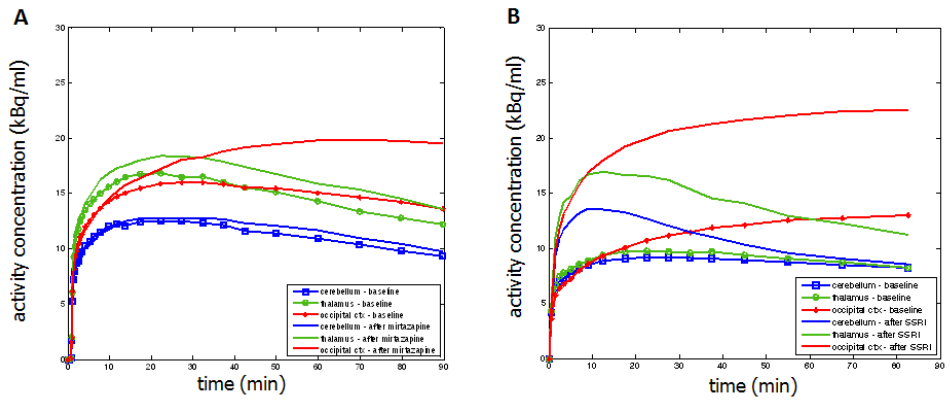

Figure 7.8: TACs of subject 1 (Imperial dataset, A) and subject 4 (OCD, HRS dataset, B): cerebellum (blue squares and blue solid line, respectively), thalamus (green circles and green solid line, respectively), occipital cortex (red dots and red solid line, respectively).

7.2 Modeling [^{11}C]MDL100907 dataset

On the basis of Region of Interest (ROI) analysis, [^{11}C]MDL100907 is usually assumed to be reversible as its kinetics are well described by a 2T model ([78], [92]). In literature [^{11}C]MDL100907 data have been previously evaluated only with plasma input reversible compartmental models ([78], [92]) and with reference input models (graphical and compartmental models) ([93]).

This study aimed to define the best quantitative model for [^{11}C]MDL100907 considering its kinetics at voxel level and using spectral analysis in order to avoid the problem of tissue heterogeneity implied by the ROI approach. Moreover using a data-driven approach such as spectral analysis there was no necessity to define a model structure *a priori* and neither reversibility nor irreversibility were imposed on the tracer kinetics.

[^{11}C]MDL100907 activity distributed in regions according to the 5-HT$_{2A}$ receptor density (Figure 7.8), i.e. high level of activity was seen in cortical regions, intermediate in several medial temporal lobe structures, low in hippocampus, amyg-

dale, and lowest in thalamus and cerebellum. At baseline, for both datasets, in cerebellum, thalamus and hippocampus, activity peaked relatively early (12-22 min), while in medial temporal lobe structures it peaked later (27-45 min). In neocortical regions, peak activity was reached slowly (55-90 min).

For Imperial dataset, there was a clear qualitative difference in the tracer activity in neocortical regions at baseline and blocked condition for each subject (Figure 7.8), while no relative changes were observed in cerebellum and thalamus kinetics.

In HSR dataset, no changes were detected in neocortical regions after administration of SSRI (Figure 7.8), while it was possible detect a change in the kinetics of low binding regions (cerebellum and thalamus).

7.2.1 Metabolite curve fitting

Both Imperial data and HSR dataset included plasma measures not corrected for metabolites.

Various models are available in literature for the fit of the unmetabolized parent fraction of [^{11}C]MDL100907 ([72] and [78]). The model reported in [78] refines the previous model of [72], which was derived empirically. The novel model contains an additional parameter q_3 which reflects the proportion of radioactivity in plasma at time zero, which is not due to parent compound. Positive values of this parameter could represent radiochemical impurities or rapidly formed radiolabelled metabolites in the body, and probably it is related to the rapid metabolism of [^{11}C]MDL100907 as it is the parameter with the greatest inter- and intra-subject variability.

This model was appropriate for the fit of the unmetabolized parent radiotracer measures of both Imperial and HSR dataset. The model is described by:

$$Ppf(t) = \left(1 + (q_1 t)^2\right)^{-q_2} - q_3 \qquad with\ q_1 > 0, q_2 > 0, q_3 > 0 \tag{7.7}$$

where $Ppf(t)$ is the parent plasma fraction. The model was solved with WNLLS, using a Levenberg-Marquardt minimization procedure as implemented in Matlab. The relative weights for the individual data points were defined as the inverse of the variance associated to the data, up to a scale factor γ, where the variance was modeled assuming Poisson statistics. The proportionality constant γ was estimated *a posteriori* as in [39] and [40].

For the subjects without any metabolites data (HSR dataset) the estimates obtained from the fit of the average of all measures were used for the description of the unmetabolized parent fraction.

After the generation of the individual PPf, for each sampling time t_i ($i = 1, \ldots, n$, with n total number of frames) the parent plasma input function (C_p) was obtained for each subject by multiplying the Ppf with the measures of tracer concentration in plasma uncorrected for metabolites (C_{meas}) as in:

$$C_p(t_i) = C_{meas}(t_i) \cdot Ppf(t_i) \tag{7.8}$$

Finally, the concentration of the radioactivity in the whole blood (C_b) was calculated as:

$$C_b(t_i) = (1 - 0.3 \cdot H)\, C_{meas}(t_i) \tag{7.9}$$

where H is the hematocrit, set by default at 0.8 ([94]).

7.2.2 Classic Spectral Analysis (SA)

Spectral analysis (SA) utilizes a general input-output model to identify the kinetic components of tissue tracer activity without any specific compartmental model assumptions ([5], [95]). The system output is described by the convolution of the input function with an exponential impulse response that has real-valued, decaying exponents. Once the spectrum of kinetic components has been esti-

mated, knowledge of the tracer's biochemical and/or physiololgical properties can be used to relate parameters of the identified spectrum to measures of the process of interest.

In spectral analysis, the concentration of radioactivity in tissue at time t, $C_T(t)$, is modeled as a convolution of the plasma time-activity curve, $C_p(t)$, with the sum of M+2 distinct exponential terms as:

$$C_T(t) = \sum_{j=0}^{M+1} C_p(t) \otimes \alpha_j e^{-\beta_j t} = \sum_{j=0}^{M+1} \alpha_j \int_0^t C_p(\tau) e^{-\beta_j (t-\tau)} d\tau \qquad (7.10)$$

where α_j and β_j are assumed to be real-valued and nonnegative. In Eq. 7.10 the maximum number of terms to be included in the model, $M+2$, is predefined and set to an arbitrary large number, e.g., 100.

Possible values of β_j are fixed to cover a biological plausible spectral range, and values of α_j are estimated from blood and tissue TACs by a nonnegative least squares procedure. In practice, only a few components with $\alpha_j > 0$ are detected ([96]). The factors determining which components are identified are the definition of the grid, the measurement error affecting the data, the sensitivity of the radioactivity to the changes in the intervals of the exponents, the algorithm chosen and the convergence criteria ([95]).

From Eq. 7.10 it can be observed that "high-frequency" components, i.e., components with very large β_j, become proportional to $C_p(t)$, accounting for the fast passage of the tracer in the vascular space of the ROI (vascular volume or spillover component, V_b), whereas "low-frequency" components, i.e., those with $\beta_j = 0$ or near zero, become proportional to $\int C_p(t)dt$ and account for trapping of tracer. Components with intermediate values of β_j reflect tissue compartments within the ROI that exchange material directly or indirectly with plasma, giving an indication of tissue heterogeneity.

It must be recalled that the spectra components do not depend on a specific model and the interpretation of the parameters of the different components can

be derived only on the basis of a structural model. However from the estimated parameters is possible to derive the total binding rate constant (K, ml/g/min) for irreversible tracers, or the total volume of distribution (V_T, ml/g).
Eq. 7.10 can be written to explicitly show the trapping of tracer and the vascular component V_b as:

$$C_T(t) = \alpha_0 \int_0^t C_p(\tau)d\tau + \sum_{j=1}^{M} \alpha_j \int_0^t C_p(\tau)e^{-\beta_j(t-\tau)}d\tau + V_b C_b(t) \qquad (7.11)$$

The SA in its original version presents some problems, first of all the so called "line doubling". As the β_j's values of the grid are discrete, often the true spectra components fall between two consecutive values and the algorithm cannot always place a component in the exact position that would yield the best fit of the data: in this case the respective β_j are estimated with low precision ([39]). Also, the method requires the β_j to be positive. Among the most common problems, there is also the identification of very slow components ("phantom"), which are not present in the original data. The shorter the scanning schedule and the higher the noise level, the broader the distribution of phantom components ([95]). In general, a lower cutoff frequency, β_{cutoff}, is defined and all the components in the tissue with $0 < \beta_j < \beta_{cutoff}$ are considered resulting from noise in the data, shifting trapping components from their true position in $\beta_j = 0$, while components with $\beta_j > \beta_{cutoff}$ are assumed to correspond to real equilibrating process in the system. This value of cutoff is generally calculated as in [95], i.e. $\beta_{cutoff} = 1/T_{end}$, where T_{end} is the end time of the scan.

7.2.3 Non Linear Spectral Analysis (NLSA)

A new SA method (Non Linear Spectral Analysis, NLSA) was proposed in [39] by revisiting the classic SA as an exponential impulse response identification problem and overcoming the issues described in the previous section (the non

negativity constraint for α_j, the low precision of the estimates, the line doubling and the impossibility to convert the estimated parameters in kinetic variables).
In this revised approach, it is not necessary to define a grid for the eigenvalues and to estimate the corresponding amplitudes, but the impulsive response function is identified by estimating the number of exponentials necessary to fit the data solving models of increasing order using WNLLS. Then model parsimony criteria as Akaike Information Criterion (AIC) are used to choose the best model. It is to be noted that no constraints are required for α_j and β_j: in fact, even if the impulsive response of a generic compartmental model must be always positive, its coefficient do not have to be positive, unless input and output are in the same compartment.
In the current study, six different models of increasing complexity were compared, from a model with the only trapping component up to a model with three reversible components, with the following equations:

$$C_T(t) = (1 - V_b)\left(\alpha_0 \int_0^t C_p(\tau)\, d\tau\right) + V_b C_b(t) \tag{7.12}$$

$$C_T(t) = (1 - V_b)\left(\alpha_1 \int_0^t C_p(\tau)\, e^{-\beta_1 (t-\tau)} d\tau\right) + V_b C_b(t) \tag{7.13}$$

$$C_T(t) = (1 - V_b)\left(\alpha_0 \int_0^t C_p(\tau)\, d\tau + \alpha_1 \int_0^t C_p(\tau)\, e^{-\beta_1 (t-\tau)} d\tau\right) + V_b C_b(t) \tag{7.14}$$

$$C_T(t) = (1 - V_b)\left(\alpha_1 \int_0^t C_p(\tau)\, e^{-\beta_1 (t-\tau)} d\tau + \alpha_2 \int_0^t C_p(\tau)\, e^{-\beta_2 (t-\tau)} d\tau\right) + V_b C_b(t) \tag{7.15}$$

$$\begin{aligned} C_T(t) = (1 - V_b)\Bigg(\alpha_0 \int_0^t C_p(\tau)\, d\tau + \alpha_1 \int_0^t C_p(\tau)\, e^{-\beta_1 (t-\tau)} d\tau + \\ + \alpha_2 \int_0^t C_p(\tau)\, e^{-\beta_2 (t-\tau)} d\tau\Bigg) + V_b C_b(t) \end{aligned} \tag{7.16}$$

$$\begin{aligned} C_T(t) = (1 - V_b)\Bigg(\alpha_1 \int_0^t C_p(\tau)\, e^{-\beta_1 (t-\tau)} d\tau + \alpha_2 \int_0^t C_p(\tau)\, e^{-\beta_2 (t-\tau)} d\tau + \\ + \alpha_3 \int_0^t C_p(\tau)\, e^{-\beta_3 (t-\tau)} d\tau\Bigg) + V_b C_b(t) \end{aligned} \tag{7.17}$$

where V_b, α_j and β_j were estimated with WNLLS, and the choice of the optimal model to describe the data was based on AIC, goodness of the fit, estimates included in the physiological interval and precision estimates.
It is to be noted that in this approach it is possible to obtain also the precisions of β_j, and not only of α_j, and the problem of line doubling is clearly avoided. Thus this approach provides model-independent information allowing selecting the compartmental model appropriate for the description of the data.

7.2.4 NLSA results: ROI analysis

At ROI level, NLSA was implemented in order to avoid the problems related to the classical version, given the low number of TACs to be analyzed and the higher signal-to-noise ratio of the ROI curves.
The models selected for the implementation of the NLSA were described by Eq. 7.12 - 7.17, and the parameters were estimated at ROI level with a WNLLS estimator, using a Levenberg-Marquardt minimization procedure as implemented in Matlab. The relative weights were defined as the inverse of the variance of the decay-corrected activity, i.e. frame length over TAC activity, less than a scale factor γ, as defined in [39] and [40].
The value of cutoff was calculated as $\beta_{cutoff} = 1/T_{end} = 0.011$ ([95]).

Results In Table 7.1 and Table 7.2 the results of the NLSA applied on ROI are reported for Imperial and HSR datasets respectively. For both datasets, in all subjects the majority of the regions were described by the model of Eq. 7.14, i.e. one reversible and one irreversible component. Estimated parameters values of α_0, α_1 and β_1 and their precisions are reported.
As regard the Imperial dataset, for all subjects but one all the ROIs were best described by the model of Eq. 7.14. For one subject, the amygdale, the frontal cortex and the arterial cingulate were described by a model with only one re-

ROI	V_b *[unitless]*	α_1 *[ml/g/min]*	β_1 *[min^{-1}]*	α_0 *[ml/g/min]*
Hippocampus	0.055 ± 0.028	0.280 ± 0.053	0.027 ± 0.011	0.134 ± 0.049
Amygdala[a]	0.062 ± 0.022	0.238 ± 0.048	0.022 ± 0.006	0.134 ± 0.049
Cerebellum	0.051 ± 0.034	0.319 ± 0.070	0.032 ± 0.002	0.067 ± 0.021
Thalamus	0.061 ± 0.037	0.420 ± 0.056	0.028 ± 0.004	0.076 ± 0.026
Frontal cortex[a]	0.051 ± 0.034	0.278 ± 0.044	0.019 ± 0.004	0.169 ± 0.032
Temporal cortex	0.047 ± 0.027	0.229 ± 0.056	0.019 ± 0.003	0.158 ± 0.031
Anterior cingulate	0.074 ± 0.043	0.328 ± 0.073	0.018 ± 0.003	0.199 ± 0.039
Posterior lobe[a]	0.049 ± 0.030	0.250 ± 0.047	0.020 ± 0.004	0.180 ± 0.036
Occipital lobe	0.046 ± 0.028	0.281 ± 0.065	0.017 ± 0.004	0.159 ± 0.057

[a] Values are mean ± SD for 5 subjects.

Table 7.1: Inter-subject regional estimated parameters values of α_0, α_1 and β_1 obtained from ROI analysis with NLSA (Imperial dataset). The values are reported as mean ± SD for 6 subjects, except where indicated.

ROI	V_b *[unitless]*	α_1 *[ml/g/min]*	β_1 *[min^{-1}]*	α_0 *[ml/g/min]*
Hippocampus	0.055 ± 0.011	0.206 ± 0.036	0.028 ± 0.003	0.181 ± 0.041
Amygdala	0.060 ± 0.021	0.181 ± 0.055	0.034 ± 0.011	0.215 ± 0.048
Cerebellum	0.046 ± 0.003	0.279 ± 0.042	0.035 ± 0.006	0.177 ± 0.043
Thalamus	0.056 ± 0.011	0.307 ± 0.032	0.029 ± 0.006	0.150 ± 0.041
Frontal cortex[a]	0.040 ± 0.006	0.212 ± 0.183	0.030 ± 0.006	0.291 ± 0.019
Temporal cortex[a]	0.046 ± 0.002	0.185 ± 0.130	0.035 ± 0.005	0.296 ± 0.015
Anterior cingulate[a]	0.064 ± 0.006	0.190 ± 0.126	0.036 ± 0.021	0.354 ± 0.048
Posterior lobe[a]	0.045 ± 0.001	0.121 ± 0.004	0.030 ± 0.006	0.295 ± 0.019
Occipital lobe[a]	0.044 ± 0.004	0.144 ± 0.007	0.026 ± 0.005	0.314 ± 0.005

[a] Values are mean ± SD for 3 subjects.

Table 7.2: Inter-subject regional estimated parameters values of α_0, α_1 and β_1 obtained from ROI analysis with NLSA (HSR dataset). The values are reported as mean ± SD for 4 subjects, except where indicated.

versible component, but the estimated $\beta_1 < \beta_{cutoff}$, becoming compatible with the irreversibility found in the other regions.
The irreversible component was especially detected in cortical regions with the ratio α_0/α_1 ranging from 0.6 to 0.75, while in cerebellum and thalamus this ratio was around 0.2, but the trapping was still clearly identified. The results confirmed what already presented in previous studies, i.e. tracer binding was high in cortical regions, intermediate in temporal regions, low in hippocampus, amygdale, and lowest in thalamus and cerebellum ([73], [78], [92]).
The fact that in some regions the results did not show the trapping line may be due to a too short observation interval. In this interval the steady state was not reached, and the model was consequently not definite yet, as the estimates obtained for the reversible component model were not physiological.

The same held also for the HSR dataset. For all subjects but one, all ROIs were best described by the model of Eq. 7.14, with one reversible and one irreversible component. For one subject, the frontal and temporal cortex, the arterial cingulate, the posterior and occipital lobe were described by a model with only one reversible component, but the estimated $\beta_1 < \beta_{cutoff}$, becoming compatible with the irreversibility found in the other regions. As for the Imperial dataset, the irreversible component was especially detected in cortical regions with the ratio α_0/α_1 ranging from 1.4 to 2.4, while in cerebellum and thalamus this ratio was around 0.5, but the trapping was still clearly identified.

7.2.5 SA results: voxel analysis

As the TACs derived from a single voxel are characterized by a low signal-to-noise ratio, and given the high number of TACs to be analyzed, the use of nonlinear estimators can be difficult and unwieldy because of their computational cost. Consequently, at voxel level the classical version of SA was implemented.

The grid for the β_j's was defined as a logarithmic distribution of β_j, $j = 1, 2, \ldots, M$ ([97], [95]), with $M + 1$ set equal to 100. The lower limit of the distribution was defined as $\beta_1 = 1/(3T_{end})$ where T_{end} is the end time of the scan, and the upper limit was $\beta_M = (3/T_{in})$ where T_{in} is the duration of the first scan ([95]). Therefore the spacing of the β_j's was fixed as:

$$\beta_j = \frac{1}{T_j} \quad and\, T_j = T_{j-1}\left[\frac{T_{end}}{T_{in}}\right]^{\frac{1}{M-1}} \qquad for\; j = 2, 3, ..., M \tag{7.18}$$

The M+1 unknown values α_j were estimated with the weighted nonnegative linear least squares algorithm implemented in Matlab by the *lsqnonneg* function. The relative weights for the individual data points were defined as the inverse of the variance of the decay-corrected activity, i.e. frame length over whole brain activity. The whole brain activity was used instead of the activity in the voxel due to the high noise of the voxel TACs. The value for the cutoff frequency was $\beta_{cutoff} = 1/T_{end}$ as in [95].

Results SA results clearly showed at voxel level the presence of an irreversible component, especially in cortical regions, thus confirming the results obtained at ROI level with NLSA.

In Figure 7.9 the parametric map of the amplitude of irreversible component K estimated with SA is presented for two representative subjects (subject 1 of Imperial dataset, A, and subject 3 of HSR dataset, B). For both datasets, the irreversible component was identified in more than 70% of the voxel.

In Table 7.3 the inter-subject average values (of all voxels in the 9 selected ROIs) of K estimated with SA on the Imperial and HSR datasets are presented. The values are reported as mean ± SD. Both from Figure 7.9 and Table 7.3 it can be seen that the regional distribution of K was consistent with the known serotonin receptor distribution ([73], [78], [92]). More specifically, in both datasets, the cortical regions had the highest signal (the anterior cingulate, followed by

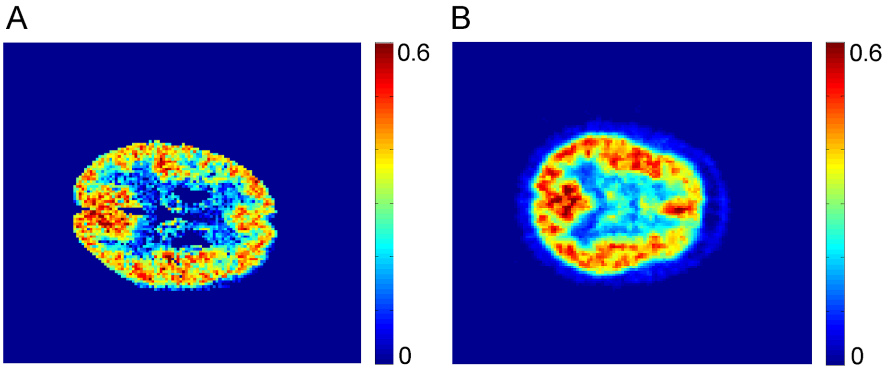

Figure 7.9: Parametric map of the amplitude of the irreversible component K [ml/g/min] estimated with classic SA for subject 1 of the Imperial dataset (A) and for subject 3 of the HSR dataset (B), shown in the transverse plane.

ROI	*Irreversible component Imperial dataset [ml/g/min]*	*Irreversible component HSR dataset [ml/g/min]*
Hippocampus	0.166 ± 0.022	0.231 ± 0.040
Amygdala	0.167 ± 0.026	0.250 ± 0.037
Cerebellum	0.082 ± 0.027	0.214 ± 0.039
Thalamus	0.113 ± 0.023	0.209 ± 0.043
Frontal cortex	0.236 ± 0.033	0.318 ± 0.022
Temporal cortex	0.216 ± 0.039	0.308 ± 0.025
Anterior cingulate	0.291 ± 0.042	0.382 ± 0.019
Posterior lobe	0.236 ± 0.037	0.320 ± 0.022
Occipital lobe	0.249 ± 0.068	0.344 ± 0.034

Table 7.3: Inter-subject average values (of all voxels in the 9 selected ROIs) of the amplitude of the irreversible component estimated with SA on the Imperial and HSR datasets. The values are reported as mean ± SD.

posterior lobe and frontal cortex), while thalamus and cerebellum (not present in the images) had the lowest signal. Only in cerebellar and thalamus voxels it was possible to properly identify also a very slow reversible component, probably due to the lack or reduced density of 5-HT_{2A}.
In Figure 7.10 the weighted frequency spectrum, normalized to the peak considering all subjects of the datasets, is presented (Imperial, A, and HSR, B), with the cerebellum (upper panel, red), thalamus (middle panel, black), temporal cortex (lower panel, blue). The temporal cortex is a good representative of the other cortical regions. As previously reported, in both cerebellum and thalamus it was possible to clearly identify a reversible component almost as important as the irreversible one (Figure 7.10, upper and middle panel), while for the cortex the reversible component was generally lower and less frequent (Figure 7.10, lower panel).

7.2.6 Discussion

Irreversibility of [^{11}C]MDL100907 kinetic

Both at ROI and voxel level, an irreversible component was found in both dataset, especially in cortical regions. At ROI level, only for one subject in each dataset, some regions were described by a model with only one reversible component, but the estimated $\beta_1 < \beta_{cutoff}$, becoming consistent with the irreversibility found in the other regions. The fact that in some regions the results did not show the trapping line may be due to a too short observation interval. In this interval the steady state was not reached, and the model was consequently not definite yet, as the estimates obtained for the one exponential model were not physiological.
At voxel level, the irreversible component was identified in more than 70% of the voxel, especially in cortical regions, with a distribution consistent with the known serotonin receptor distribution ([73], [78]), thus confirming the results obtained

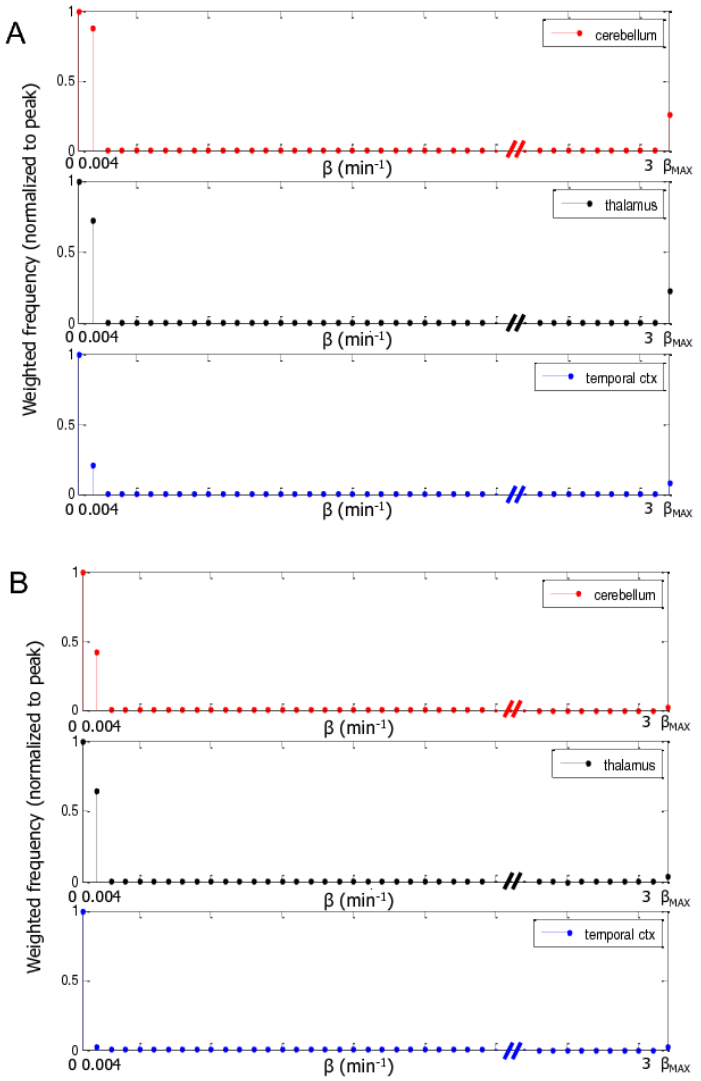

Figure 7.10: Weighted frequency spectrum normalized to the peak considering all subjects of the datasets (Imperial, A, and HSR, B): cerebellum (upper panel, red), thalamus (middle panel, black), temporal cortex (lower panel, blue). The temporal cortex is a good representative of the other cortical regions.

at ROI level with NLSA. Only in cerebellar and thalamus voxels it was possible to properly identify also a very slow reversible component, probably due to the lack or reduced density of 5-HT_{2A}.

In order to confirm the results obtained at voxel level with the classic SA, NLSA was also implemented at voxel level for two subjects of both datasets, with the same models (Eq. 7.12 - 7.17) and the same settings as for the estimation at ROI level. The results confirmed those obtained with linear SA, the majority of the voxel TACs were best described by the model of Eq. 7.12 i.e. one irreversible component, (70% of voxels) while the remaining voxel TACs were best fitted by the model of Eq. 7.14, i.e. one reversible and one irreversible component.
These results are in agreement with those found with the classic SA, as in high binding regions only a small number of voxels had a second component, while in low binding regions (cerebellum and thalamus), the second component was very slow, but detectable.
As future work, an iterative filtered version of classical SA (Spectral Analysis with Iterative Filter, [98]) will be applied to [^{11}C]MDL100907 data in order to overcome the problems of the original SA detailed above and to improve the accuracy and the precision of the estimated spectrum.
The iterative filtered version has not been applied from the beginning to [^{11}C]MDL 100907 data, as it works only on irreversible tracers and the presence of a trapping component in [^{11}C]MDL100907 kinetics was not proved yet.

A recent work ([92]) confirmed what already found previously in [78], particularly the reversibility of the [^{11}C]MDL100907 kinetics. It must be firstly highlighted that this study is the first one to quantify [^{11}C]MDL100907 data with a data-driven model, i.e. not defining any *a priori* model structure neither imposing reversibility or irreversibility of the tracer. It must be noted in this sense that all previous studies had always quantified [^{11}C]MDL100907 data only with reversible

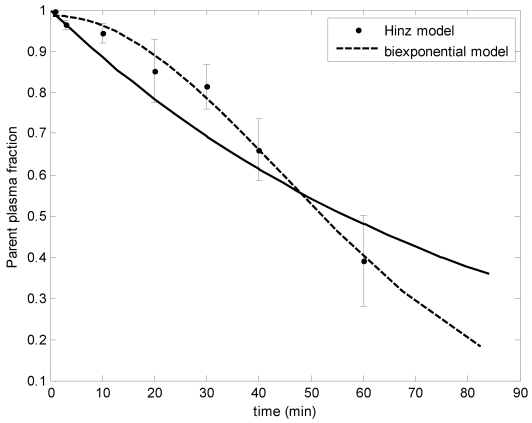

Figure 7.11: Average of fraction of unmetabolized parent fraction of [^{11}C]MDL100907 in plasma (HSR dataset). The plotted bars are the mean values ± SD for the 3 available subjects. The dashed line is the fit of the metabolite model of Eq. 7.7, the solid line is the fitted constrained biexponental model.

models, and no irreversible models have ever been proposed.

Another main difference is in the model chosen for the fit of the unmetabolized parent measures. The model proposed in [92] is a constrained biexponential model, a simplified model compared with the one presented in [78] (described by Eq. 7.7).

Consequently the performance of the two different models were compared, i.e. model of Eq. 7.7 and the constrained biexponential model, as in [92], in describing the unmetabolized parent measures of Imperial and HSR dataset.

In Figure 7.11 the average fraction of unmetabolized parent fraction of [^{11}C]MDL100907 in plasma for HSR dataset is reported. The plotted bars are the mean values ± SD for the 3 available subjects. The dashed line is the fit of the model of Eq. 7.7, the solid line is the fitted biexponential model. As it can be seen from the figure, the biexponential model performed poorly compared to the model proposed in [78], with the Residual Sum of Squares (RSS) being in average 174% higher than the RSS of the biexponential model (range: 40% - 438%). The same held also

for Imperial dataset.

Having defined the optimal model for the fit of the unmetabolized measures, in order to assess the impact of a different model on the final estimates, NLSA was applied at ROI level using as forcing function the one obtained with the constrained biexponential model.
The optimal model for the majority of the region was the model of Eq. 7.15, i.e. two reversible components, using as choice criteria only AIC. But once we considered also goodness of fit and particularly the precision of estimates, the optimal model was again the one of Eq. 7.14, i.e. one reversible and one irreversible component. The estimated precision of the microparameters obtained for the more complex model was higher than 200%.
Moreover, considering each compartment estimated kinetics, it was easy to see that the second reversible component constituted a "fake" compartment, i.e. a compartment whose kinetic has rate constant values close to zero.
Consequently, the choice of the model for the fit of the unmetabolized measures is crucial, as it has a substantial impact on the quantification process.

Effect due to mirtazapine

After administration of blockade, there was a clear effect on cortical regions, while low binding regions as thalamus and cerebellum were less affected.
Considering the plasma input function measured on the only one subject after administration of mirtazapine (subject 1_b), it was not possible to observe any change in the arterial input function either.
NLSA was applied at voxel level on subject 1_b, and the results obtained were in agreement with those obtained on the other subjects analyzed at baseline, i.e. 65% voxel TACs were fitted with the model of Eq. 7.12 (one irreversible component) and the remaining voxel TACs were best described by the model of Eq.

7.14 (one reversible and one irreversible component).

On the basis also of previously published studies, the NLSA results could be interpreted as respectively a 1tissue-1 rate constant (1K) model and a 3K model. Once defined the model structure, it was possible to convert the spectral analysis parameters into compartmental model ones.

The model parameters (described in Section 2.2, and indicating with K_1 also the rate constant for transport of tracer from plasma to tissue for model 1K) were then compared between baseline and blocking studies, considering all voxel without anatomical discrimination.

For the voxels where 1K was the optimal model, a reduction of 54% was found in the value of K_1 from baseline to blocking study (baseline: 0.414 ± 0.21; blocked: 0.191 ± 0.192). In the remaining voxels fitted with the 3K model, a reduction of 49% was observed still on the K_1 (baseline: 0.71 ± 0.217; blocked: 0.363 ± 0.287), while k_2 and k_3 remained almost unaltered in the two studies (k_2: baseline: 0.0351 ± 0.0386; blocked: 0.0372 ± 0.052; k_3: baseline 0.0214 ± 0.021; blocked: 0.0211 ± 0.023).

Consequently the blockade seemed to act on the input of the tracer in the tissue, while the trapping was not affected. This resulted in a reduction on the value of K_1 for the 1K model, as in the simplified model the parameter contains information of both the reversible and the irreversible components. Clearly, these are the results of only one subject, and the analysis is not exhaustive, but it can be considered as a general indication of the process.

From a short simulation (data not presented), the possibility that the difference in K_1 could be related to a drug-induced change in a low non-specific kinetic component was excluded, as in this case the main changes would be on k_2 and k_3. The same held also defining a different model structure from the NLSA results, i.e. a model in parallel, as the main effect due to the drug would be still on the k_2 and k_3. The more plausible explanation for the change on the parameter induced by the mirtazapine seemed to be a lowered tracer perfusion.

Effect due to SSRI

The SSRI was administrated only to OCD patients (HSR dataset), but for those subjects the arterial input information was missing. The effect due to the drug on the tracer kinetics was analyzed, and no changes were found in the cortical regions, while it was possible to identify a substantial change in the reference tissue TACs.

Nevertheless, without any arterial input function, the effect due to SSRI was difficult to quantify. In order to evaluate the possible effect on the input function, the Image Derived Input Function (IDIF) was extracted via cluster analysis. The curves were then manually obtained defining the regions over the carotid arteries on the early PET frames and then averaging the TACs of the voxels within the ROI. There were no differences in the IDIF kinetics after administration of fluvoxamine.

7.2.7 Method for the selection of the optimal reference region

As described in Chapter 4 and in Section 7.2, [^{11}C]MDL100907 data have been previously evaluated also with reference input models (graphical and compartmental models) ([93]).

For HSR dataset, no input data were available and consequently an accurate analysis on the suitability of the cerebellum as reference region was necessary.

Data after administration of mirtazapine (from Imperial dataset) were analyzed using the drug's antagonist action at the 5-HT$_{2A}$ receptor to study its effect on the TACs for [^{11}C]MDL100907 binding and especially on the cerebellum. HSR data of OCD patients at baseline and after administration of SSRI were analyzed to study the effect of the drug on the cerebral TACs and on the cerebellum kinetics.

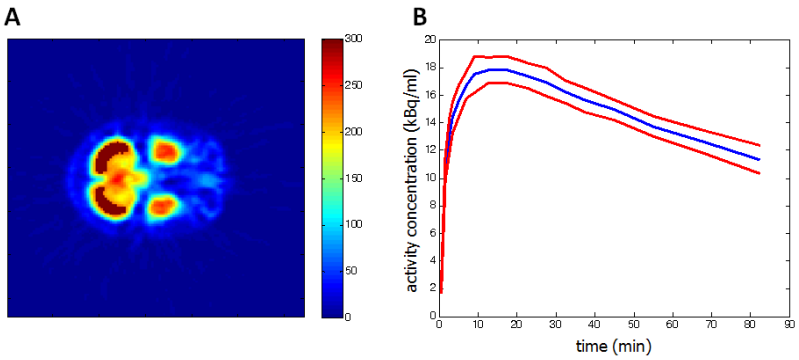

Figure 7.12: (A) Summed PET for subject 2 (OCD) of HSR dataset. The reference region is highlighted. (B) TAC of the reference region drawn in (A) (red line) and its confidence interval calculated on 1 SD (blue line).

In order to evaluate the impact of the different drug treatments, the reference region was automatically extracted from the cerebellum area by using cluster analysis based on the parameterization of the tracer's kinetics, as described in Section 4.2. As for [^{11}C]WAY100635 data, the parameters chosen were the slope and the intercept of the regression line on the last 5 points of the voxel TACs, corresponding to the last 45 minutes of the PET exam. The threshold applied to the probability map obtained from the Fuzzy C-means was set equal to 85%. The total number of clusters was set equal to 8, as the purpose was the segmentation of the whole cerebellum, without fragmenting it.

Having obtained kinetically homogeneous regions, the reference region was manually selected extracting the two symmetrical region of cerebellar cortex.

An example of the resulting reference mask of a parametric clustering on [^{11}C]MDL 100907 data is reported in Figure 7.12A for subject 2 (OCD) of HSR dataset. The reference region is highlighted over the summed PET image. The reference region was identified for all the subjects by cluster analysis in the cerebellum. The cluster analysis allowed selecting an appropriate homogenous reference region, as the voxel TACs were very similar, showing a standard deviation within

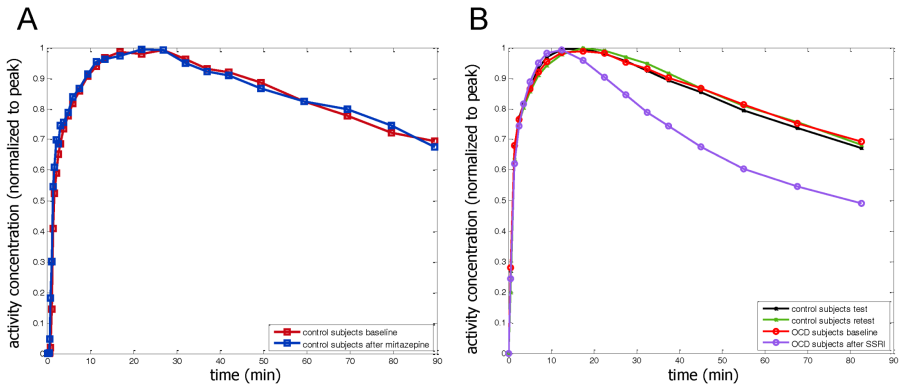

Figure 7.13: Mean of the extracted reference region TACs (normalized to peak) of the two datasets: (A) Imperial dataset, control subjects at baseline (red squares) and after administration of mirtazapine (blue squares), (B) HSR dataset, control subjects at baseline (test and retest: black and green crosses) and OCD subjects at baseline (red circles) and after administration of SSRI (violet circles).

the region lower than 5% (Figure 7.12B).

In Figure 7.13 the means of the extracted reference region TACs (normalized to peak) of the two datasets are presented. Figure 7.13A reports the curves of the control subjects at baseline (red squares) and after administration of mirtazapine (blue squares) for the Imperial dataset, whereas in Figure 7.13B the curves of the control subjects at baseline (test and retest: black and green crosses) and for OCD subjects at baseline (red circles) and after administration of SSRI (violet circles) for the HSR dataset are reported.

The reference region showed no changes in the kinetics for the baseline condition, neither between patients and control subjects (HSR dataset, Figure 7.13B), nor between the two datasets. From a comparison between Figure 7.13A and Figure 7.13B it can be seen that the kinetics are similar, even if there is a slight shift between the two curves, and the mean ratio between the two reference TACs is 0.99 ± 0.11.

After administration of mirtazapine, there was a change in the kinetics of the cortical regions, while this change did not occur in the reference region (Imperial dataset, Figure 7.13A, as already found in [78] and [92]).

Instead after administration of SSRI, there was an alteration in the reference kinetic (Figure 7.13B), while the kinetic of the other regions remained unaltered. To the best of the author's knowledge, this is the first study which assessed the validity of the cerebellum as reference region for [^{11}C]MDL100907 after administration of SSRI in humans.

On the basis of the results obtained, it was not possible to define clearly the causes for this difference in the reference kinetics, but it is hypothesized that there could be a metabolism and/or protein binding dependent effect that can be visible only in the reference region using an high affinity tracer as [^{11}C]MDL100907 because of the small exchangeable compartment of the reference itself.

This finding strongly indicates that cerebellum cannot be used as true reference region in presence of pharmacological treatment that potentially modifies metabolic enzymes like SSRI ([99], [100]).

Chapter 8

Overall discussion

8.1 Compartmental modeling at voxel level

Compartmental modeling represents the gold standard in PET quantification and the methodologies developed aim to use compartmental modeling to quantify PET images at voxel level. In both cases, a hierarchical approach was implemented, using the information obtained at ROI level as *a priori* information for the estimation process at voxel level.

In H-MAP the method uses a linear or linearized compartmental model, which is then solved with a MAP estimator.

In H-BFM, the compartmental model is solved at voxel level in its non linear version applying BFMs for PET quantification.

Both methodologies, as described in Chapter 2, can be applied to any PET receptor compartmental model.

H-MAP was applied to a linearized mono-compartmental model, whereas H-BFM was applied to a 2 tissue compartmental model.

If the methods were to be applied to different models, no effect on the computational time is to be expected. In fact, in the case of H-MAP, the method can be applied on any linear or linearized model, and the size of the state matrix would have no impact on the time required for the estimate.

H-BFM was already applied on one of the more complex model that is used in receptor studies, and the eventual addition of a trapping component would not represent a problem as it would just imply an addition of a linear component to the estimation, without any effect on the grid definition and on the computation cost.

On the contrary, the application of H-BFM to a simpler model (as for example a 1T model, or the model presented in Section 7.1) would imply the definition of only one grid, from the sampling of the Gaussian distribution obtained from the ROI estimates, with the advantage of being able to sample on a denser grid, with no impact on the computational cost.

8.2 Comparison of the novel methods with existing methodologies

As it has been described in Chapter 1, there are other methodologies available for quantification at the voxel level based on compartmental modeling.

The graphical methods (Patlak and Logan plot) allow fast estimation of the parameters of interest. For both methods, though, it is possible to estimate only a macroparameter, with no information on the singular kinetic parameters, unless a model structure is assumed. Moreover, estimates obtained using the Logan approach are affected by bias, both at the ROI and voxel level ([30]).

Likelihood estimation in graphical analysis ([83]) and Empirical Bayesian estimation in graphical analysis ([33]) are two alternative approaches developed to eliminate the bias of the Logan plot results, but both of them still estimate only one system parameter. Moreover, the model used is not linear and thus the methods are not appropriate for voxel-wise PET quantification.

In the linear and non linear ridge regression with spatial constraints ([23], [26])

the *a priori* information is provided for each voxel by the TACs of the voxels in its neighborhood, using thus only a local prior. The method requires two iterations of the regression analysis, making it appropriate only for linear models, as the computational cost would be too high for clinical routine use in case of non linear models.

BFMs and spectral analysis both require an *a priori* definition of a grid, which is user-defined and fixed for all brain voxels. The choice of the grid can heavily penalize the results and can lead to bias in the final estimates, which can also be affected by the presence of noise in the data ([95]). Moreover spectral analysis allow the estimation only of macro parameters, and the relation of these parameters to measures of the physiological process of interest is possible only with knowledge of the biochemical properties of the tracer and with the definition of the model structure.

All the methods described above present critical drawbacks which are instead overcome with the novel approaches proposed in this work.
In fact the methods developed are user-independent and allow a fast, precise and accurate estimation of the parameters of interest. Moreover, one of the main advantage of compartmental modeling at voxel level compared to other methodologies is the possibility to obtain estimates for the microparameters, allowing a much more detailed description of the receptor system and more insight in the physiology.
One example is reported from the results presented in Section 6.2, i.e. H-BFM applied to [^{11}C]FLB457 and [^{11}C]WAY100635 data.
In Figure 8.1 is presented the parametric maps for the parameter k_3 and the Pearson's correlation values between the average of the WNLLS and H-BFM estimates are reported for each subject (H-BFM A and H-BFM C) for both [^{11}C]FLB457 and [^{11}C]WAY100635 datasets. It can be seen that the correlation values were

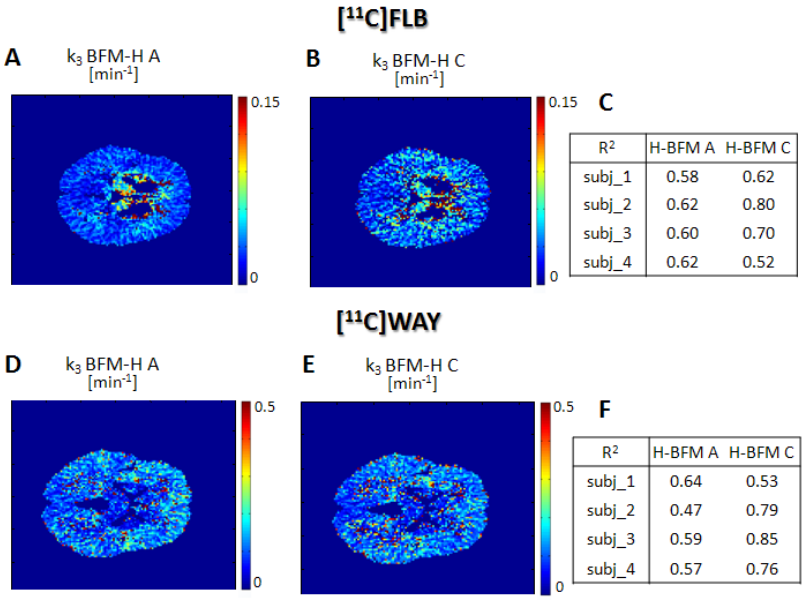

R²	H-BFM A	H-BFM C
subj_1	0.58	0.62
subj_2	0.62	0.80
subj_3	0.60	0.70
subj_4	0.62	0.52

R²	H-BFM A	H-BFM C
subj_1	0.64	0.53
subj_2	0.47	0.79
subj_3	0.59	0.85
subj_4	0.57	0.76

Figure 8.1: (A - B). Parametric maps of [^{11}C]FLB457 k_3 estimated with H-BFM A (A) and H-BFM C (B) of a representative subject (subject 3). (C - D). Parametric maps of [^{11}C]WAY100635 k_3 estimated with H-BFM A (C) and H-BFM C (D) of a representative subject (subject 4). (E - F) Pearson's values between the average within the ROIs of the WNLLS and H-BFM voxel estimates for each subject for both [^{11}C]FLB457 (E) and [^{11}C]WAY100635 (F)

clearly lower than the ones for the volume of distribution presented in Figure 6.6 and Figure 6.8, as expected, but they showed still good correlation with $R^2 > 0.6$ for [^{11}C]FLB457 and $R^2 > 0.57$ for [^{11}C]WAY100635 .

Other methods for the generation of parametric maps are those based on the so called "population approaches" originally developed in the pharmacokinetic/pharmacodynamic literature, in particular Two-Stages iterative algorithms, i.e. Global Two Stages (GTS) and to a minor extent due to computational reasons Iterative Two Stages (ITS, [101]). Consequently, these two methods were investigated applied to [^{11}C]DPN data.

It has been demonstrated that these methods can allow to obtain reliable estimates of individual parameters also in 'data poor' environments, as in voxel-wise estimation with a low signal-to-noise ratio. In these methods, the individuals sharing homogenous characteristics are considered belonging to the same popula-

tion. These subjects are then studied together, thus allowing to obtain not only the individual estimates but also a description of the population distribution.
Both can be applied to the voxel-wise quantification problem considering the voxels belonging to the same ROI as individuals of a population. The parameters derived at ROI level were hypothesized representative of the expected model parameters values of the voxels composing the ROI itself and the standard deviation of the parameters estimation error was assumed to represent the uncertainty of the expected values.

8.2.1 Global Two Stage

This is an iterative method, in which the estimates for each voxel are iteratively updated using both the population variability and the precision of the individual estimates.
The initial estimates were obtained applying at voxel level 1T model linearized (Eq. 2.20), which was solved with a linear least square estimator.
GTS was then applied in order to eliminate the bias introduced with the linearization of the model.
There is no consensus on the criterion to use to stop iterations. Iterations were stopped when the relative difference of each parameter between the current and previous iteration was lower than 1% for at least 90% of the pixels included in the considered population ([6]).

The same sensitiveness for the initial estimates already described in previous works was found. As described in Section 4.1.1 [^{11}C]DPN kinetics are nearly irreversible and this represents a difficulty in the estimation of the parameters of interest, in particular due to k_2 which is estimated with a very low value and an extremely narrow variability.
In fact the estimated variance of k_2 is around 10^{-3} $(\text{min}^{-1})^2$ while the population

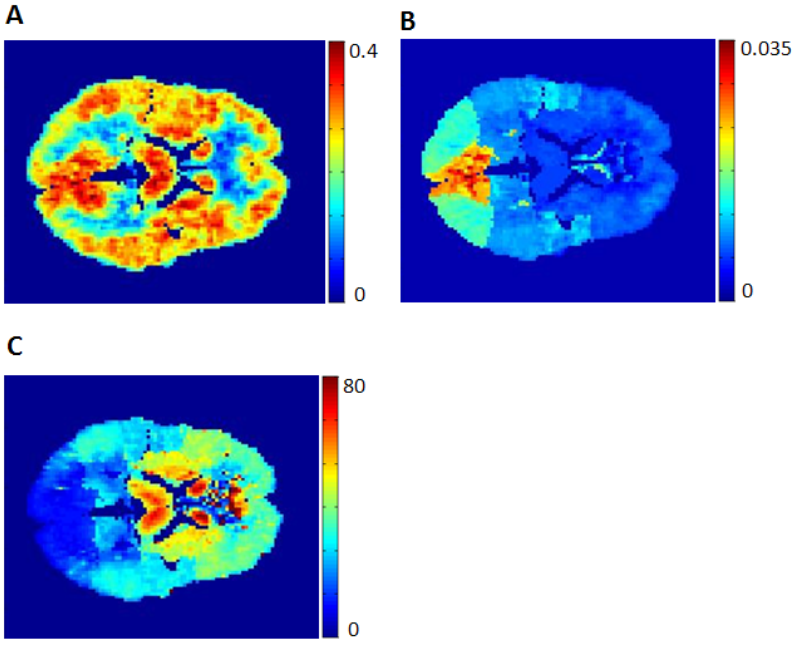

Figure 8.2: Parametric maps of [^{11}C]DPN K_1 (A), k_2 (B) and the derived parameter V_T (C) estimated with GTS for a representative subject (subject 3).

variance (the variability intra-region or intra-cluster) is around 10^{-5} $(min^{-1})^2$. Because of the great difference between the variance of the estimation in the pixel and the population variance (of the prior), the final GTS estimates of k_2 are biased towards the prior (Figure 8.2B), and this affects obviously the derived V_T estimates (Figure 8.2C). Instead, there are no problems in the estimation of K_1 (Figure 8.2C), being a more stable parameter. The use of relative weights with the calculation of γ *a posteriori* did not change the results.

A further attempt to correct the GTS estimates was made, by adding a correcting factor to level up the weight of the data and the population weight, but it did not improve the results.

Despite a small improvement, specific for only few regions and particularly for the right hemisphere, it was not enough to solve the problem. Moreover, it is not possible to enlarge too much the variance of the priors, as the *a priori* information would be lost.

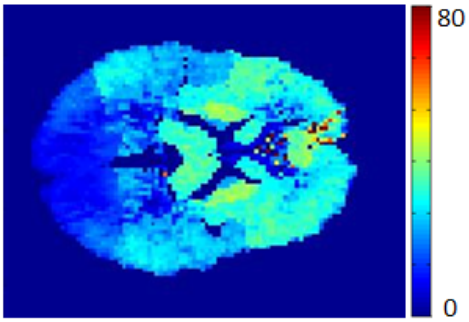

Figure 8.3: Parametric map of [^{11}C]DPN V_T estimated with GTS for a representative subject (subject 3).

Using GTS, with the same settings as above, to estimate directly V_T, i.e. defining an unique prior based on the initial V_T estimates, there was a slight improvement (Figure 8.3). Nevertheless, the estimates were driven towards the priors, as the variance of V_T is calculated from the variance of k_2, using the propagation the rule.

Thus the same considerations already made in [6] and [32] apply also here: if the initial estimates are robust, GTS allows for an improvement of the final estimates. But if the initial estimates are not adequate, GTS is unable to provide good results.

8.2.2 Iterative Two Stage

ITS is an iterative method in which the individual estimates are updated using a MAP estimator, using as empirical prior the mean and variance of the population (i.e. the ROI which the voxel belongs to).

Applied by [101] to ROI curves it gave very promising results.

The initial estimates were obtained applying LEGA (Eq. 5.1) at voxel level, solved with WNLLS, as it has been demonstrated that LEGA provides good results on ROI level, but it fails at pixel level ([83], [85]).

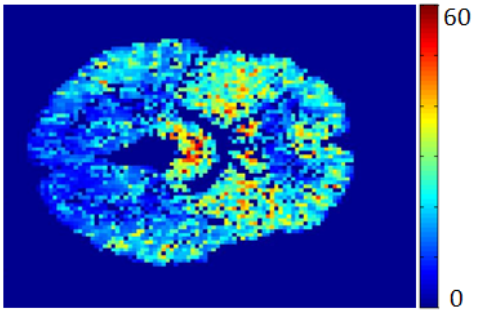

Figure 8.4: Parametric maps of [^{11}C]DPN V_T estimated with ITS for a representative subject (subject 3).

As graphical method, LEGA uses only the last few points in the calculation of the volume of distribution (when the equilibrium is reached), so some difficulties in the estimation can already be expected, because of the slow kinetics of the tracer.

The priors for the MAP estimators were defined from the population mean and variance of the initial estimates within the region/cluster, using only the values in a physiological range (i.e. non negative volume of distribution). With this settings, the iterative analysis was implemented.

The crucial termination criterion was the same as for GTS, i.e. iterations were stopped when the relative difference of each parameter between the current and previous iteration was lower than 1% for at least 90% of the pixels included in the considered population.

In the final results, 15% of voxels failed to converge, presenting a negative volume of distribution.

Despite the non negligible percentage of voxel with non-physiological values, the results are promising, as the final estimates were close to the gold standard, but the parametric maps were very noisy, despite the use of a MAP estimator (Figure 8.4). The non convergence occurred mostly in noisy voxel TACs, where the last points which are used by the graphical method present an increasing trend, leading to a non-physiological V_T.

Attempts to ameliorate the final parametric maps did not succeed, as for example applying GTS as smoothing filter, due to the big difference between the variance of the data and the variance of the priors.
It is thus necessary to modify the method, but the problem it is not trivial. This represents still an open issue and it will require an *ad hoc* solution.

8.3 Development of an alternative clustering algorithm

An additional but not less important result is the development of a new clustering approach which allows the segmentation of the brain volume even for PET data with high level of noise, without effect on the time required (the whole process does not require more than 20 min, when the k-means applied to the whole voxel TACs does not take less than 10 min).
This new approach was used for the ROI extraction for [^{11}C]WAY100635 , [^{11}C]SCH 442416 and [^{11}C]MDL100907 data. Moreover, it was applied on [^{11}C]MDL100907 data to select an appropriate homogenous reference region from the cerebellum.

In general, as described in Section 6.3, the way to derive the priors did not affect the final results: the images did not differ qualitatively, and the average percentage difference of estimates was in general less than 3%, for all the datasets and both H-MAP and H-BFM. For this reason, it can be inferred that priors defined in such a way are appropriate and allow a robust estimation of the model parameters.

The number of ROIs and clusters (when segmenting using anatomical or functional information respectively) had an effect on the quality of the final parametric maps. The BrainAtlas was composed by more than 70 ROIs and resulted in reliable estimates.

The use of a too rich or too poor atlas in terms of ROIs will imply less informative priors and consequently too noisy or too smoothed, respectively, parametric maps.

In particular, the consequence in using an atlas with a relevant richer number of ROIs will be a parametric map of the same quality of one obtained with conventional least square estimators applied at voxel level. In general, from the results obtained with an anatomical atlas with up to 83 regions, it would not be useful an atlas very detailed, with a number of regions bigger than 100 (which would be smaller and better defined), because the priors would be less informative resulting in noisier estimates.

The same considerations hold when functional segmentation is used: if the number of clusters is set smaller than the optimal one, the priors will have bigger SD and consequently there will be a smoothing on the estimates. If the number of clusters is set bigger than the optimal one, the centroids of the clusters will not be statistically different between each other and there will be repetition of the kinetics. The optimal number of cluster (as defined in Section 6.3) was automatically selected as the greatest possible number which keeps the centroids statistically different between each other. The statistical difference was tested with the Wilcoxon's test, as implemented in Matlab. In Figure 8.5 an example of centroids obtained applying k-means to [^{11}C]DPN data, setting K equal to the optimal number of clusters (for this subject $K = 7$, Figure 8.5A) is presented. In Figure 8.5B are presented also the centroids obtained clustering the cerebral volume in 14 regions (overclustering). When the centroids of the clusters are not statistically different between each other, there is repetition of the kinetics less than a scale factor.

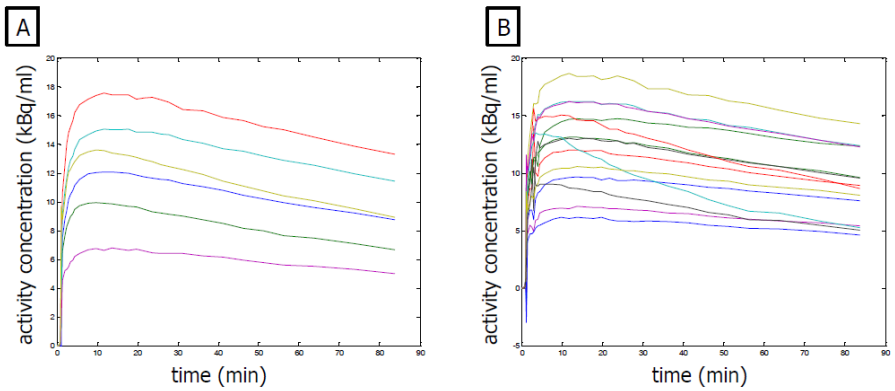

Figure 8.5: Example of centroids obtained with k-means applied on the whole voxel TACs of [^{11}C]DPN (subject 3), subdivided in K = 7 clusters (optimal number, A) and K = 14 clusters (overclustering, B).

8.4 Conclusions

The main results of this work are the development of two methods for voxel-wise quantification of PET data, H-MAP and H-BFM. The methods are fast and robust, and represent a good alternative for the generation of reliable parametric maps. Applied to clinical data are expected to make it easier the detection also of small/specific pathological areas. The first method led to a publication in Neuroimage ([12]), the second was presented during two international conferences (BrainPET2011 and SNM2011) as oral contribute and a publication is ready to be submitted.

The novel methods proposed have been already inserted in PIWAVE, a pre-existing software for voxel-wise PET quantification originally developed by Imperial College of London.

Moreover, as collateral results, new compartmental models were developed for [^{11}C]SCH442416 and [^{11}C]MDL100907 data and a new clustering approach which allow segmenting the brain volume even for PET data with high level of noise was implemented. This new method was also applied for the selection of the optimal reference region for [^{11}C]MDL100907 data.

Bibliography

[1] D. Feng, S. C. Huang, Z. Z. Wang, and D. Ho. An unbiased parametric imaging algorithm for nonuniformly sampled biomedical system parameter estimation. *IEEE Trans Med Imaging*, 15:512–518, 1996.

[2] R. N. Gunn, A. A. Lammertsma, S. P. Hume, and V. J. Cunningham. Parametric imaging of ligand-receptor binding in PET using a simplified reference region model. *Neuroimage*, 6(4):279–87, 1997.

[3] Y. T. Hong and T. D. Fryer. Kinetic modelling using basis functions derived from two-tissue compartmental models with a plasma input function: general principle and application to [18F]fluorodeoxyglucose positron emission tomography. *Neuroimage*, 51:164–172, May 2010.

[4] Y. T. Hong, J. S. Beech, R. Smith, J. C. Baron, and T. D. Fryer. Parametric mapping of [18F]fluoromisonidazole positron emission tomography using basis functions. *J. Cereb. Blood Flow Metab.*, 31:648–657, Feb 2011.

[5] V. J. Cunningham and T. Jones. Spectral analysis of dynamic PET studies. *J Cereb Blood Flow Metab*, 13(1):15–23, 1993.

[6] G. Tomasi, A. Bertoldo, and C. Cobelli. PET parametric imaging improved by global-two-stage method. *Ann Biomed Eng*, 37:419–427, Feb 2009.

[7] N. M. Alpert and F. Yuan. A general method of Bayesian estimation for parametric imaging of the brain. *Neuroimage*, 45:1183–1189, May 2009.

[8] A. Gjedde. Calculation of cerebral glucose phosphorylation from brain uptake of glucose analogs in vivo: a re-examination. *Brain Res.*, 257:237–274, Jun 1982.

[9] C. S. Patlak, R. G. Blasberg, and J. D. Fenstermacher. Graphical evaluation of blood-to-brain transfer constants from multiple-time uptake data. *J. Cereb. Blood Flow Metab.*, 3:1–7, Mar 1983.

[10] J. Logan, J. S. Fowler, N. D. Volkow, A. P. Wolf, S. L. Dewey, D. J. Schlyer, R. R. MacGregor, R. Hitzemann, B. Bendriem, and S. J. Gatley. Graphical analysis of reversible radioligand binding from time-activity measurements applied to [N-11C-methyl]-(-)-cocaine PET studies in human subjects. *J. Cereb. Blood Flow Metab.*, 10:740–747, Sep 1990.

[11] R.E. Carson, C. Cobelli, and L. Filkestein. *The Mathematical Modeling of Metabolic and Endocrine Systems*. Wiley, New York, 1993.

[12] G. Rizzo, F. E. Turkheimer, S. Keihaninejad, S. K. Bose, A. Hammers, and A. Bertoldo. Multi-Scale hierarchical generation of PET parametric maps: Application and testing on a [11C]DPN study. *Neuroimage*, 59:2485–2493, Feb 2012.

[13] R. N. Gunn, S. R. Gunn, F. E. Turkheimer, J. A. Aston, and V. J. Cunningham. Positron emission tomography compartmental models: a basis pursuit strategy for kinetic modeling. *J Cereb Blood Flow Metab*, 22(12):1425–39, 2002.

[14] S. S. Kety. The theory and applications of the exchange of inert gas at the lungs and tissues. *Pharmacol. Rev.*, 3:1–41, Mar 1951.

[15] L. Sokoloff, M. Reivich, C. Kennedy, M. H. Des Rosiers, C. S. Patlak, K. D. Pettigrew, O. Sakurada, and M. Shinohara. The [14C]deoxyglucose method for the measurement of local cerebral glucose utilization: theory, procedure, and normal values in the conscious and anesthetized albino rat. *J. Neurochem.*, 28:897–916, May 1977.

[16] M. A. Mintun, M. E. Raichle, M. R. Kilbourn, G. F. Wooten, and M. J. Welch. A quantitative model for the in vivo assessment of drug binding sites with positron emission tomography. *Ann. Neurol.*, 15:217–227, Mar 1984.

[17] G. Blomqvist, S. Pauli, L. Farde, L. Ericksson, A. Persson, and C. Halldin. *Positron Emission Tomography in Clinical Research: Tracer Modelling and Radioreceptors (Developments in Nuclear Medicine)*. Springer, 1989.

[18] V. J. Cunningham, S. P. Hume, G. R. Price, R. G. Ahier, J. E. Cremer, and A. K. Jones. Compartmental analysis of diprenorphine binding to opiate receptors in the rat in vivo and its comparison with equilibrium data in vitro. *J. Cereb. Blood Flow Metab.*, 11:1–9, Jan 1991.

[19] S. P. Hume, R. Myers, P. M. Bloomfield, J. Opacka-Juffry, J. E. Cremer, R. G. Ahier, S. K. Luthra, D. J. Brooks, and A. A. Lammertsma. Quantitation of carbon-11-labeled raclopride in rat striatum using positron emission tomography. *Synapse*, 12:47–54, Sep 1992.

[20] A. A. Lammertsma, C. J. Bench, S. P. Hume, S. Osman, K. Gunn, D. J. Brooks, and R. S. Frackowiak. Comparison of methods for analysis of clinical [11C]raclopride studies. *J. Cereb. Blood Flow Metab.*, 16:42–52, Jan 1996.

[21] A. A. Lammertsma and S. P. Hume. Simplified reference tissue model for PET receptor studies. *Neuroimage*, 4:153–158, Dec 1996.

[22] Claudio Cobelli and E.R. Carson. *Introduction to modeling in physiology and medicine*. Academic Press series in biomedical engineering. Academic Press, San Diego, 2008.

[23] Y. Zhou, S. C. Huang, and M. Bergsneider. Linear ridge regression with spatial constraint for generation of parametric images in dynamic positron emission tomography studies. *IEEE Transactions on Nuclear Science*, 48:125–130, Feb 2001.

[24] X. Dai, Z. Chen, and J. Tian. Performance evaluation of kinetic parameter estimation methods in dynamic FDG-PET studies. *Nucl Med Commun*, 32:4–16, Jan 2011.

[25] F. E. Turkheimer, R. Hinz, R. N. Gunn, J. A. Aston, S. R. Gunn, and V. J. Cunningham. Rank-shaping regularization of exponential spectral analysis for application to functional parametric mapping. *Phys Med Biol*, 48(23):3819–41, 2003.

[26] Y. Zhou, S. C. Huang, M. Bergsneider, and D. F. Wong. Improved parametric image generation using spatial-temporal analysis of dynamic PET studies. *Neuroimage*, 15:697–707, Mar 2002.

[27] A. Hammers, R. Allom, M. J. Koepp, S. L. Free, R. Myers, L. Lemieux, T. N. Mitchell, D. J. Brooks, and J. S. Duncan. Three-dimensional maximum probability atlas of the human brain, with particular reference to the temporal lobe. *Hum Brain Mapp*, 19:224–247, Aug 2003.

[28] R. A. Koeppe, V. A. Holthoff, K. A. Frey, M. R. Kilbourn, and D. E. Kuhl. Compartmental analysis of [11C]flumazenil kinetics for the estimation of ligand transport rate and receptor distribution using positron emission tomography. *J. Cereb. Blood Flow Metab.*, 11:735–744, Sep 1991.

[29] G. Blomqvist. On the construction of functional maps in positron emission tomography. *J. Cereb. Blood Flow Metab.*, 4:629–632, Dec 1984.

[30] M. Slifstein and M. Laruelle. Models and methods for derivation of in vivo neuroreceptor parameters with PET and SPECT reversible radiotracers. *Nucl. Med. Biol.*, 28:595–608, Jul 2001.

[31] R. B. Innis, V. J. Cunningham, J. Delforge, M. Fujita, A. Gjedde, R. N. Gunn, J. Holden, S. Houle, S. C. Huang, M. Ichise, H. Iida, H. Ito, Y. Kimura, R. A. Koeppe, G. M. Knudsen, J. Knuuti, A. A. Lammertsma, M. Laruelle, J. Logan, R. P. Maguire, M. A. Mintun, E. D. Morris, R. Parsey, J. C. Price, M. Slifstein, V. Sossi, T. Suhara, J. R. Votaw, D. F. Wong, and R. E. Carson. Consensus nomenclature for in vivo imaging of reversibly binding radioligands. *J Cereb Blood Flow Metab*, 27(9):1533–1539, 2007.

[32] G. Tomasi, A. Bertoldo, C. Cobelli, N. Pavese, Y. F. Tai, A. Hammers, and F. E. Turkheimer. Global-two-stage filtering of clinical PET parametric maps: application to [(11)C]-(R)-PK11195. *Neuroimage*, 55:942–953, Apr 2011.

[33] F. Zanderigo, R. T. Ogden, A. Bertoldo, C. Cobelli, J. J. Mann, and R. V. Parsey. Empirical Bayesian estimation in graphical analysis: a voxel-based approach for the determination of the volume of distribution in PET studies. *Nucl. Med. Biol.*, 37:443–451, May 2010.

[34] J. B. MacQueen. Some methods for classification and analysis of multivariate observations. In L. M. Le Cam and J. Neyman, editors, *Proc. of the fifth Berkeley Symposium on Mathematical Statistics and Probability*, volume 1, pages 281–297. University of California Press, 1967.

[35] J.C. Dunn. A fuzzy relative of the isodata process and its use in detecting compact well-separated clusters. *Journal of Cybernetics*, 3:32–57, 1973.

[36] J.C. Bezdek. *Pattern Recognition with Fuzzy Objective Function Algorithms*. Plenum, 1981.

[37] Thomas Kailath, Ali H. Sayed, and Babak Hassibi. *Linear Estimation*. Prentice Hall, 2000.

[38] H. Vincent Poor. *An Introduction to Signal Detection and Estimation (Springer Texts in Electrical Engineering)*. Springer, 1994.

[39] A. Bertoldo, P. Vicini, G. Sambuceti, A. A. Lammertsma, O. Parodi, and C. Cobelli. Evaluation of compartmental and spectral analysis models of [(18)F]FDG kinetics for heart and brain studies with PET. *IEEE Trans Biomed Eng*, 45(12):1429–48, 1998.

[40] B. M. Bell, J. V. Burke, and Schumitzky A. A relative weighting method for estimating parameters and variances in multiple data sets. *Comput Stat Data Anal*, 22:2: 119–135, 1996.

[41] A. Hammers and A. Lingford-Hughes. Opioid imaging. *Neuroimaging Clin. N. Am.*, 16:529–552, Nov 2006.

[42] A. K. Jones, S. K. Luthra, B. Maziere, V. W. Pike, C. Loc'h, C. Crouzel, A. Syrota, and T. Jones. Regional cerebral opioid receptor studies with [11C]diprenorphine in normal volunteers. *J. Neurosci. Methods*, 23:121–129, Mar 1988.

[43] B. Sadzot, J. C. Price, H. S. Mayberg, K. H. Douglass, R. F. Dannals, J. R. Lever, H. T. Ravert, A. A. Wilson, H. N. Wagner, and M. A. Feldman. Quantification of human opiate receptor concentration and affinity using high and low specific activity [11C]diprenorphine and positron emission tomography. *J. Cereb. Blood Flow Metab.*, 11:204–219, Mar 1991.

[44] J. W. Lewis and S. M. Husbands. The orvinols and related opioids–high affinity ligands with diverse efficacy profiles. *Curr. Pharm. Des.*, 10:717–732, 2004.

[45] A. Hammers, M. C. Asselin, F. E. Turkheimer, R. Hinz, S. Osman, G. Hotton, D. J. Brooks, J. S. Duncan, and M. J. Koepp. Balancing bias, reliability, noise properties and the need for parametric maps in quantitative ligand PET: [(11)C]diprenorphine test-retest data. *Neuroimage*, 38:82–94, Oct 2007.

[46] P. E. Kinahn and J. G. Rogers. Analytic 3D image reconstruction using all detected events. *IEEE Trans Nucl Sci*, 36:964–968, Feb 1989.

[47] I. S. Gousias, D. Rueckert, R. A. Heckemann, L. E. Dyet, J. P. Boardman, A. D. Edwards, and A. Hammers. Automatic segmentation of brain MRIs of 2-year-olds into 83 regions of interest. *Neuroimage*, 40:672–684, Apr 2008.

[48] F. Maes, A. Collignon, D. Vandermeulen, G. Marchal, and P. Suetens. Multimodality image registration by maximization of mutual information. *IEEE Trans Med Imaging*, 16:187–198, Apr 1997.

[49] A. K. Jones, V. J. Cunningham, S. K. Ha-Kawa, T. Fujiwara, Q. Liyii, S. K. Luthra, J. Ashburner, S. Osman, and T. Jones. Quantitation of [11C]diprenorphine cerebral kinetics in man acquired by PET using presaturation, pulse-chase and tracer-only protocols. *J. Neurosci. Methods*, 51:123–134, Mar 1994.

[50] N. E. Anden and G. Stock. Effect of clozapine on the turnover of dopamine in the corpus striatum and in the limbic system. *J. Pharm. Pharmacol.*, 25:346–348, Apr 1973.

[51] M. S. Lidow, G. V. Williams, and P. S. Goldman-Rakic. The cerebral cortex: a case for a common site of action of antipsychotics. *Trends Pharmacol. Sci.*, 19:136–140, Apr 1998.

[52] H. Takahashi, M. Higuchi, and T. Suhara. The role of extrastriatal dopamine D2 receptors in schizophrenia. *Biol. Psychiatry*, 59:919–928, May 2006.

[53] J. M. Stone, J. M. Davis, S. Leucht, and L. S. Pilowsky. Cortical dopamine D2/D3 receptors are a common site of action for antipsychotic drugs–an original patient data meta-analysis of the SPECT and PET in vivo receptor imaging literature. *Schizophr Bull*, 35:789–797, Jul 2009.

[54] H. Olsson, C. Halldin, C. G. Swahn, and L. Farde. Quantification of [11C]FLB 457 binding to extrastriatal dopamine receptors in the human brain. *J. Cereb. Blood Flow Metab.*, 19:1164–1173, Oct 1999.

[55] C. Halldin, L. Farde, T. Hogberg, N. Mohell, H. Hall, T. Suhara, P. Karlsson, Y. Nakashima, and C. G. Swahn. Carbon-11-FLB 457: a radioligand for extrastriatal D2 dopamine receptors. *J. Nucl. Med.*, 36:1275–1281, Jul 1995.

[56] A. J. Montgomery, P. Stokes, Y. Kitamura, and P. M. Grasby. Extrastriatal D2 and striatal D2 receptors in depressive illness: pilot PET studies using [11C]FLB 457 and [11C]raclopride. *J Affect Disord*, 101:113–122, Aug 2007.

[57] H. Olsson and L. Farde. Potentials and pitfalls using high affinity radioligands in PET and SPET determinations on regional drug induced D2 receptor occupancy–a simulation study based on experimental data. *Neuroimage*, 14:936–945, Oct 2001.

[58] D. Baldwin and S. Rudge. The role of serotonin in depression and anxiety. *Int Clin Psychopharmacol*, 9 Suppl 4:41–45, Jan 1995.

[59] J. N. Joyce, A. Shane, N. Lexow, A. Winokur, M. F. Casanova, and J. E. Kleinman. Serotonin uptake sites and serotonin receptors are altered in the limbic system of schizophrenics. *Neuropsychopharmacology*, 8:315–336, Jun 1993.

[60] L. Farde, H. Ito, C. G. Swahn, V. W. Pike, and C. Halldin. Quantitative analyses of carbonyl-carbon-11-WAY-100635 binding to central 5-hydroxytryptamine-1A receptors in man. *J. Nucl. Med.*, 39:1965–1971, Nov 1998.

[61] V. W. Pike, J. A. McCarron, A. A. Lammertsma, S. Osman, S. P. Hume, P. A. Sargent, C. J. Bench, I. A. Cliffe, A. Fletcher, and P. M. Grasby. Exquisite delineation of 5-HT1A receptors in human brain with PET and [carbonyl-11 C]WAY-100635. *Eur. J. Pharmacol.*, 301:5–7, Apr 1996.

[62] R. V. Parsey, M. Slifstein, D. R. Hwang, A. Abi-Dargham, N. Simpson, O. Mawlawi, N. N. Guo, R. Van Heertum, J. J. Mann, and M. Laruelle. Validation and reproducibility of measurement of 5-HT1A receptor parameters with [carbonyl-11C]WAY-100635 in humans: comparison of arterial and reference tissue input functions. *J. Cereb. Blood Flow Metab.*, 20:1111–1133, Jul 2000.

[63] R. M. Moresco, S. Todde, S. Belloli, P. Simonelli, A. Panzacchi, M. Rigamonti, M. Galli-Kienle, and F. Fazio. In vivo imaging of adenosine A2A receptors in rat and primate brain using [11C]SCH442416. *Eur J Nucl Med Mol Imaging*, 32(4):405–413, 2005.

[64] S. N. Schiffmann, G. Fisone, R. Moresco, R. A. Cunha, and S. Ferre. Adenosine A2A receptors and basal ganglia physiology. *Prog. Neurobiol.*, 83:277–292, Dec 2007.

[65] S. Todde, R. M. Moresco, P. Simonelli, P. G. Baraldi, B. Cacciari, G. Spalluto, K. Varani, A. Monopoli, M. Matarrese, A. Carpinelli, F. Magni, M. G. Kienle, and F. Fazio. Design, radiosynthesis, and biodistribution of a new potent and selective ligand for in vivo imaging of the adenosine A(2A) receptor system using positron emission tomography. *J. Med. Chem.*, 43:4359–4362, Nov 2000.

[66] D. J. Brooks, S. Papapetropoulos, F. Vandenhende, D. Tomic, P. He, A. Coppell, and G. O'Neill. An open-label, positron emission tomography study to assess adenosine A2A brain receptor occupancy of vipadenant (BIIB014) at steady-state levels in healthy male volunteers. *Clin Neuropharmacol*, 33:55–60, 2010.

[67] I.D. Hinz, R. Grachev, D.L. Cutler, J. Hunter, S. Osman, M. Doder, D.J. Brooks, and V.J. Cunningham. In-vivo quantification of A2A receptors in human brain with [11C]SCH442416 and positron emission tomography. *Molecular Imaging and Biology*, 5:1656, May-June 2003.

[68] A. F. Ramlackhansingh, S. K. Bose, I. Ahmed, F. E. Turkheimer, N. Pavese, and D. J. Brooks. Adenosine 2A receptor availability in dyskinetic and nondyskinetic patients with Parkinson disease. *Neurology*, 76:1811–1816, May 2011.

[69] I. B. Galazzo, S. K. Bose, A. F. Ramlackhansingh, I. Ahmed, N. Pavese, G. Rizzo, D. J. Brooks, F. E. Turkheimer, and A. Bertoldo. Kinetic modeling of the adenosine A2A subtype receptor radioligand [11C]SCH442416 in humans. *Neuroimage*, 52:S178, Aug 2010.

[70] A. Pazos, R. Cortes, and J. M. Palacios. Quantitative autoradiographic mapping of serotonin receptors in the rat brain. II. Serotonin-2 receptors. *Brain Res.*, 346:231–249, Nov 1985.

[71] C. Lundkvist, C. Halldin, N. Ginovart, S. Nyberg, C. G. Swahn, A. A. Carr, F. Brunner, and L. Farde. [11C]MDL 100907, a radioligland for selective imaging of 5-HT(2A) receptors with positron emission tomography. *Life Sci.*, 58:187–192, 1996.

[72] H. Watabe, M. A. Channing, M. G. Der, H. R. Adams, E. Jagoda, P. Herscovitch, W. C. Eckelman, and R. E. Carson. Kinetic analysis of the 5-HT2A ligand [11C]MDL 100,907. *J. Cereb. Blood Flow Metab.*, 20:899–909, Jun 2000.

[73] H. Ito, S. Nyberg, C. Halldin, C. Lundkvist, and L. Farde. PET imaging of central 5-HT2A receptors with carbon-11-MDL 100,907. *J. Nucl. Med.*, 39:208–214, Jan 1998.

[74] B. J. Jones and T. P. Blackburn. The medical benefit of 5-HT research. *Pharmacol. Biochem. Behav.*, 71:555–568, Apr 2002.

[75] D. Perani, V. Garibotto, A. Gorini, R. M. Moresco, M. Henin, A. Panzacchi, M. Matarrese, A. Carpinelli, L. Bellodi, and F. Fazio. In vivo PET study of 5HT(2A) serotonin and D(2) dopamine dysfunction in drug-naive obsessive-compulsive disorder. *Neuroimage*, 42:306–314, Aug 2008.

[76] H. P. Landolt and R. Wehrle. Antagonism of serotonergic 5-HT2A/2C receptors: mutual improvement of sleep, cognition and mood? *Eur. J. Neurosci.*, 29:1795–1809, May 2009.

[77] S. Kasper, J. Tauscher, M. Willeit, M. Stamenkovic, A. Neumeister, B. Kufferle, C. Barnas, J. Stastny, N. Praschak-Rieder, L. Pezawas, M. de Zwaan, S. Quiner, W. Pirker, S. Asenbaum, I. Podreka, and T. Brucke. Receptor and transporter imaging studies in schizophrenia, depression, bulimia and Tourette's disorder–implications for psychopharmacology. *World J. Biol. Psychiatry*, 3:133–146, Jul 2002.

[78] R. Hinz, Z. Bhagwagar, P. J. Cowen, V. J. Cunningham, and P. M. Grasby. Validation of a tracer kinetic model for the quantification of 5-HT(2A) receptors in human brain with [(11)C]MDL 100,907. *J. Cereb. Blood Flow Metab.*, 27:161–172, Jan 2007.

[79] S. A. Anttila and E. V. Leinonen. A review of the pharmacological and clinical profile of mirtazapine. *CNS Drug Rev*, 7:249–264, 2001.

[80] T. S. Furey, N. Cristianini, N. Duffy, D. W. Bednarski, M. Schummer, and D. Haussler. Support vector machine classification and validation of cancer tissue samples using microarray expression data. *Bioinformatics*, 16:906–914, Oct 2000.

[81] R. Hinz and F.E. Turkheimer. Determination of tracer arrival delay with spectral analysis. *IEEE Trans Nucl Sci*, 53(1):212–219, 2006.

[82] B. M. Mazoyer, R. H. Huesman, T. F. Budinger, and B. L. Knittel. Dynamic PET data analysis. *J Comput Assist Tomogr*, 10:645–653, 1986.

[83] R. T. Ogden. Estimation of kinetic parameters in graphical analysis of PET imaging data. *Stat Med*, 22:3557–3568, Nov 2003.

[84] M. Laruelle. Modelling: when and why? *Eur J Nucl Med*, 26:571–572, Jun 1999.

[85] R. V. Parsey, R. T. Ogden, and J. J. Mann. Determination of volume of distribution using likelihood estimation in graphical analysis: elimination of estimation bias. *J. Cereb. Blood Flow Metab.*, 23:1471–1478, Dec 2003.

[86] J. Hirvonen, S. Aalto, V. Lumme, K. Nagren, J. Kajander, H. Vilkman, N. Hagelberg, V. Oikonen, and J. Hietala. Measurement of striatal and thalamic dopamine D2 receptor binding with 11C-raclopride. *Nucl Med Commun*, 24:1207–1214, Dec 2003.

[87] R. N. Gunn, P. A. Sargent, C. J. Bench, E. A. Rabiner, S. Osman, V. W. Pike, S. P. Hume, P. M. Grasby, and A. A. Lammertsma. Tracer kinetic modeling of the 5-HT1A receptor ligand [carbonyl-11C]WAY-100635 for PET. *Neuroimage*, 8:426–440, Nov 1998.

[88] V. Oikonen, T. Allonen, K. Nagren, J. Kajander, and J. Hietala. Quantification of [Carbonyl-(11)C]WAY-100635 binding: considerations on the cerebellum. *Nucl. Med. Biol.*, 27:483–486, Jul 2000.

[89] R. V. Parsey, V. Arango, D. M. Olvet, M. A. Oquendo, R. L. Van Heertum, and J. John Mann. Regional heterogeneity of 5-HT1A receptors in human cerebellum as assessed by positron emission tomography. *J. Cereb. Blood Flow Metab.*, 25:785–793, Jul 2005.

[90] K. Varani, F. Portaluppi, S. Merighi, E. Ongini, L. Belardinelli, and P. A. Borea. Caffeine alters A2A adenosine receptors and their function in human platelets. *Circulation*, 99:2499–2502, May 1999.

[91] P. Svenningsson, C. Le Moine, G. Fisone, and B. B. Fredholm. Distribution, biochemistry and function of striatal adenosine A2A receptors. *Prog. Neurobiol.*, 59:355–396, Nov 1999.

[92] P. S. Talbot, M. Slifstein, D. R. Hwang, Y. Huang, E. Scher, A. Abi-Dargham, and M. Laruelle. Extended characterisation of the serotonin 2A (5-HT2A) receptor-selective PET radiotracer 11C-MDL100907 in humans: quantitative analysis, test-retest reproducibility, and vulnerability to endogenous 5-HT tone. *Neuroimage*, 59:271–285, Jan 2012.

[93] P. T. Meyer, Z. Bhagwagar, P. J. Cowen, V. J. Cunningham, P. M. Grasby, and R. Hinz. Simplified quantification of 5-HT2A receptors in the human brain with [11C]MDL 100,907 PET and non-invasive kinetic analyses. *Neuroimage*, 50:984–993, Apr 2010.

[94] M. E. Phelps, S. C. Huang, E. J. Hoffman, C. Selin, L. Sokoloff, and D. E. Kuhl. Tomographic measurement of local cerebral glucose metabolic rate in humans with (F-18)2-fluoro-2-deoxy-D-glucose: validation of method. *Ann. Neurol.*, 6:371–388, Nov 1979.

[95] F. Turkheimer, R. M. Moresco, G. Lucignani, L. Sokoloff, F. Fazio, and K. Schmidt. The use of spectral analysis to determine regional cerebral glucose utilization with positron emission tomography and [18F]fluorodeoxyglucose: theory, implementation, and optimization procedures. *J Cereb Blood Flow Metab*, 14(3):406–22, 1994.

[96] W. H. Press, B. P. Flannery, S. A. Teukolsky, and W. T. Vetterling. *Numerical Recipes: The Art of Scientific Computing*. Cambridge University Press, 1986.

[97] E. M. DiStefano, Landaw. Multiexponential, multicompartmental, and noncompartmental modeling. I. methodological limitations and physiological interpretations. *Am J Physiol*, 246(5 Pt 2):R651–64, 1984.

[98] M. Veronese, A. Bertoldo, S. Bishu, A. Unterman, G. Tomasi, C. B. Smith, and K. C. Schmidt. A spectral analysis approach for determination of regional rates of cerebral protein synthesis with the L-[1-(11)C]leucine PET method. *J. Cereb. Blood Flow Metab.*, 30:1460–1476, Aug 2010.

[99] K. Brøsen, E. Skjelbo, B. B. Rasmussen, H. E. Poulsen, and S. Loft. Fluvoxamine is a potent inhibitor of cytochrome P4501A2. *Biochem. Pharmacol.*, 45:1211–1214, Mar 1993.

[100] K. Brøsen. The pharmacogenetics of the selective serotonin reuptake inhibitors. *Clin Investig*, 71:1002–1009, Dec 1993.

[101] A. Bertoldo, G. Sparacino, and C. Cobelli. "Population" approach improves parameter estimation of kinetic models from dynamic PET data. *IEEE Trans Med Imaging*, 23:297–306, Mar 2004.